Mineralogical and geochemical characteristics of the Utanobori and Omui epithermal gold deposits and the Omu silica sinter in northeastern Hokkaido, Japan

日本、北海道北東部、歌登および雄武威浅熱水金鉱床、雄武シリカシンターの鉱物学的-地球化学的特徴

Thomas Tagab Sorulen

I.D: 6516107

Department of Geosciences, Geotechnology, and Materials Engineering for Resources,

Graduate School of International Resource Sciences

Akita University, JAPAN

2019

AUTHOR'S STATEMENT

This thesis has been submitted to the Department of Geosciences, Geotechnology, and Materials Engineering for Resources, Graduate School of International Resource Sciences in Akita University in partial fulfillment of the requirements for the degree of Doctor in Resource Science (Geology).

The work done by the author contained within this thesis is original, and had not been submitted to other higher institutions before. Materials previously published or unpublished made mentioned in this thesis were correctly referenced, otherwise, the thesis contains no material previously written or published by another individual.

Signed: _____ Date: _____

Mr. Thomas Tagab Sorulen Akita, Japan

For bibliographical purpose, this thesis may be refereed as follows:

Sorulen, T. T., 2019. Mineralogical and geochemical characteristics of the Utanobori and Omui epithermal gold deposits and the Omu silica sinter in northeastern Hokkaido, Japan. A thesis submitted to the Department of Geosciences, Geotechnology, and Materials Engineering for Resources, Graduate School of International Resource Sciences in Akita University Japan, in partial fulfillment of the requirements for the degree of Doctor in Resource Science (Geology). Submitted: September 2019, 177 p.

ABSTRACT

The Northeast Hokkaido Metallogenic Province in the northeastern part of Hokkaido in Japan is host to epithermal precious and base metal deposits, volcanic massive sulfide (Kuroko) deposits, and subaerial-volcanic exhalative hydrothermal deposits. Amongst the various deposits, the Utanobori and Omui low sulfidation epithermal vein-type deposits, and the Omu silica sinter were studied. The objective of the study is to understand the characteristics of the silica sinter and ore-bearing veins and their relationship to mineralization and associated volcanic events on the basis of field relations, petrography, Ar-Ar and K-Ar age dating, X-ray diffractometry (XRD), inductively coupled plasma mass spectrometry (ICP-MS), atomic absorption spectroscopy (AAS), energy-dispersive X-ray spectroscopy-scanning electron microscopy (SEM-EDX), cathodoluminescence (CL), electron probe micro analysis (EPMA), and sulfur isotope analyses.

Mineralized veins of the Utanobori deposit are hosted by the Middle to Late Miocene Esashi Formation, which consists of conglomerate, sandstone, and tuff. Silica sinter and quartz-adularia veins are exposed in the Utanobori deposit. The quartz-adularia veins with ginguro bands are divided into three stages with twelve to fourteen sub-stages. Ore minerals identified include electrum, naumannite, chlorargyrite, bromargyrite and trace pyrite. These ore minerals were formed in the main mineralization stages I (bands I-b and I-d) and II (band II-a). An unidentified Fe-Sb secondary mineral is also present in the veins. Alteration assemblages imply near-neutral pH conditions during ore deposition. The SEM-CL images show that CL-dark microcrystalline quartz exhibiting colloform (ghost-sphere) texture is closely associated with ore minerals. Concentrations of Al, Fe, K, Ti, and Mn of quartz of the quartz-adularia vein with ginguro band and silica sinter were determined using EPMA. In the quartz-adularia vein with ginguro band, Al

and K contents of CL-dark microcrystalline quartz exhibiting colloform (ghost-sphere) texture are commonly >1000 ppm. This may imply that ore minerals were crystallized from alkaline and silica supersaturated fluids at temperatures <200ºC which deposited initially amorphous silica with primary colloform texture that were crystallized to microcrystalline quartz. The $\delta 34S_{CDT}$ values of fine-grained disseminated pyrite in the altered conglomerate and bedded tuff in the argillic altered zone are -4.3 ‰ and -4.2 ‰. Mineralization ages of the quartz-adularia vein with ginguro of the stages I, II and III by Ar-Ar dating determined on adularia are 13.6±0.06 Ma, 13.6±0.07 Ma, and 13.6±0.06 Ma, respectively. From available radiometric age data and field observations, two separate events of rhyolite volcanism were recognized. The first closely associated with the deposition of early formed silica sinter, and the second closely associated with the later formed mineralized quartz-adularia veins.

Mineralized veins of the Omui epithermal gold deposit are hosted by rhyolite lapilli tuff of the Miocene Propylite Lava. Approximately 8 km north of the Omui deposit, outcrops of silica sinter (Omu sinter) forming up to 3.2 m high terraces are observed south of the Otoineppu river. The mineralized quartz veins of the Omui deposit (Honpi vein) show early, middle and late stages of mineralization. The middle stage represents the main mineralization event. Abundant quartz and thin (<1 mm) ginguro bands were formed in the early stage. Mineralization accompanied with brecciation deposited ore during the middle stage, followed by the precipitation of abundant quartz and trace ginguro bands in the late stage. Kaolinite observed in the quartz veins was formed in the early and middle stages, and is lesser in the late stage. Adularia and illite were also formed, but in minor to trace amounts in the veins. Bladed calcite was formed at places in the early and middle stages. Electrum, argentite and stephanite formed in the middle stage, closely associated with microcrystalline quartz.

The Omu silica sinter is massive, and brecciated at intervals. The silica sinter is 3.2 m high and dips gently NW. Twenty nine (29) layers were recognized. Structures of the silica sinter observed includes thick (massive) and finely laminated, sinter clast breccia, low-amplitude wavy stromatolite, network and streamer fabrics, geyserite eggs, and plant-rich sinter. The Au content of the sulfide-rich brecciated base of the silica sinter is >1 ppm, and >0.1 ppm in the upper sinter clast breccia layers. The Au and Ag contents of the silica sinter are positively correlated. Base on studies conducted on thermophilic microbes that thrive along gradients of pH, geothermal fluid flow rate, fluid composition and temperature of the silica sinter lithofacies, geyserite eggs suggest temperatures of deposition range from >75ºC, and from ~60 to 75ºC for the thinly laminated, and from ~25 to ~40ºC for the thickly laminated and plant-rich sinter layers. K-Ar dating conducted on hornblende of a Rhyolite Dike reveals an age of 14.3 Ma, suggesting that the Rhyolite Dike pre-dates the Motoineppu Lava that hosted the quartz veins at the Omui deposit. The relationship of the Rhyolite Dike to mineralization is uncertain, but it may had played a role as a heat source for hydrothermal activities. The ore-forming age is not reported yet. The association of electrum with microcrystalline quartz in Omui is similar to that of the Utanobori deposit.

The deposition of silica sinters and the hydrothermal mineralization in the Utanobori and Omui epithermal gold deposits were closely related to rhyolite volcanism in each area. Quartz textures and structures were observed in mineralized veins of the Utanobori and Omui gold deposits suggest that gold was precipitated with initially amorphous silica that crystallized to microcrystalline and mosaic quartz. Silica sinters in both deposits were overprinted, suggesting that repeated hydrothermal events occurred after silica sinters were deposited. In comparison to

other low sulfidation epithermal vein-type deposits, this study has shown two of few examples where silica sinter is mineralized by cross-cutting ore-bearing veins.

ACKNOWLEDGEMENT

I would like to firstly thank the Monbukagakusho (MEXT) for the support and scholarship offered during my research and stay in Japan. Special and big word of thanks to Irving Resources Inc., for information, permission and financial support to the field work and analysis conducted on the samples. Special word of thanks and gratefulness to Prof. Akira Imai and Assist. Prof. Ryohei Takahashi for their mentorship, advice, comments and guidance during my research. The contribution, support and advice of co-authors in the manuscript is very much appreciated and thanked. Also I would like to extend my thankfulness to Prof. Andreas Agangi for his advice and comments during my research. I also thank Dr. Hinako Sato for her technical assistance during the analysis of samples,

I also kindly thank all economic geology lab members who had contributed to my joy, research and experiences during my stay in Japan, and extend my joy and thankfulness to my families and friends back home for their patience, words of advice and support.

In Chapter 3 of my thesis, I would like to extend a special word of thanks to Irving Resources Inc., especially Ms. Akiko Levinson, Dr. Quinton Hennigh, and Mr. Hidetoshi Takaoka for information, permission and financial support to the field work conducted and Ar-Ar age dating of samples. Also, a special world of thanks to the co-authors Assist. Prof. Dr. Ryohei Takahashi (Akita University), Mr. SoTanaka (Akita University), Ms. Kana Suzuki (Akita University), Prof. Dr. Akira Imai (Kyushu University), Prof. Dr. Yasushi Watanabe (Akita University) and Shingo Kikuchi (H.R.S) for their significant contribution in the submitted manuscript to Resource Geology entitled, "Mineralogical and Geochemical Characteristics of the Utanobori Gold Deposit in Northern Hokkaido, Japan" which has been published. I am grateful

to Prof. Hiroharu Matsueda of Hokkaido University and Mr. Ken Nakayama for providing samples and to Dr. Tetsuo Suzuki of H.R.S., Dr. Masahiro Yahata of My Geo, Mr. Haruo Harada of Mitsui Mineral Development Engineering Co., Ltd. for kind support and assistance. I also thank Dr. Hinako Sato for her technical assistance in ICP-MS and AAS analyses, and thank Mr. Akira Hara and Mr. Aoki Nozomi of Akita University for their kind assistant in the translation from Japanese to English during reviewing of Japanese literatures. This study presented in this chapter was financially supported by JSPS Grant-in-Aid for Scientific Research (17K06982), the Japan Mining Promotive Foundation and the Society of Resource Geology.

In Chapter 4 of my thesis, I would like to thank Irving Resources Inc., especially Ms. Akiko Levinson, Dr. Quinton Hennigh, and Mr. Hidetoshi Takaoka for information, permission and financial support to aid in field work and sample collection. I am grateful to Mr. Ken Nakayama for providing samples and to Dr. Tetsuo Suzuki of H.R.S., Dr. Masahiro Yahata of My Geo, Mr. Haruo Harada of Mitsui Mineral Development Engineering Co., Ltd. for kind support and assistance. I also thank Dr. Hinako Sato for her technical assistance in ICP-MS analysis. A special word of thanks to Assist. Prof. Dr. Ryohei Takahashi (Akita University), Mr. So Tanaka (Akita University), Ms. Kana Suzuki (Akita University), Prof. Dr. Akira Imai (Kyushu University), Prof. Dr. Yasushi Watanabe (Akita University) and Shingo Kikuchi (H.R.S) for their significant contribution towards the research entitled, "Occurrence of the Fe-Sb Oxide Mineral in the Utanobori Gold Deposit in Northern Hokkaido, Japan".

In Chapter 5 of my thesis, I would like to thank again Irving Resources Inc., especially Ms. Akiko Levinson, Dr. Quinton Hennigh, and Mr. Hidetoshi Takaoka for information, permission and financial support to aid in field work and sample collection. I am grateful to Dr. Tetsuo Suzuki of H.R.S., Dr. Masahiro Yahata of My Geo, Mr. Haruo Harada of Mitsui Mineral

Development Engineering Co., Ltd. for kind support and assistance. I also thank Dr. Hinako Sato for her technical assistance in ICP-MS and AAS analyses. A special word of thanks to Assist. Prof. Dr. Ryohei Takahashi (Akita University), Mr. Keigo Kuzumaki (Akita University), Prof. Dr. Akira Imai (Kyushu University) and Mr. Akira Hara (Akita University) for their contribution towards the research entitled, "The Omui Gold Deposit and Omu Silica Sinter in Northern Hokkaido, Japan".

TABLE OF CONTENTS

LIST OF FIGURES

Figure

LIST OF TABLES

Table

CHAPTER 1

INTRODUCTION

1.1.1 Background on epithermal deposit

Epithermal deposits (Fig. 1) are interpreted as deposits formed by rising hot fluids at shallow crustal levels, at temperature less than 200^{o}C and pressures of less than 100 bars (Lindgren, 1922, 1933). Recent studies on epithermal deposits provided a classification scheme where deposits are classified into high sulfidation (HS), intermediate sulfidation (IS), and low sulphidation (LS) based on the sulfidation state of ore-bearing fluids and sulfide mineral assemblages (Simmons *et al*., 2005).

These deposits are formed at crustal levels less than 1.5 km, and at temperatures ranging between 150^{o}C and 300^{o}C, and are commonly associated with coeval volcanic rocks and sub-volcanic equivalents of mostly calc-alkaline affinity that form in oxidized magmatic arcs (Hedenquist *et al*., 2000; Silitoe & Hedenquist, 2003; Simmons *et al*., 2005). The advanced argillic mineral assemblages consisting of alunite, kaolinite (dickite), pyrophyllite, and residual and/or vuggy silica are indicative of a HS system that formed from oxidized acidic hydrothermal fluids, and the alteration assemblages consisting of quartz-adularia ± illite and calcite are commonly associated with LS systems formed from reduced, near neutral hydrothermal fluids. IS deposits are said to be genetically related to HS deposits (Sillitoe & Hedenquest, 2003). Ore minerals in HS, IS and LS deposits commonly consists of pyrite + enargite, ± luzonite, covellite + digenite, famatinite, and orpiment, and tennantite, tetrahedrite, hematite-pyrite-magnetite, pyrite, chalcopyrite, and iron-poor sphalerite, and arsenopyrite-loellingite-pyrrhotite, pyrrhotite and iron-rich

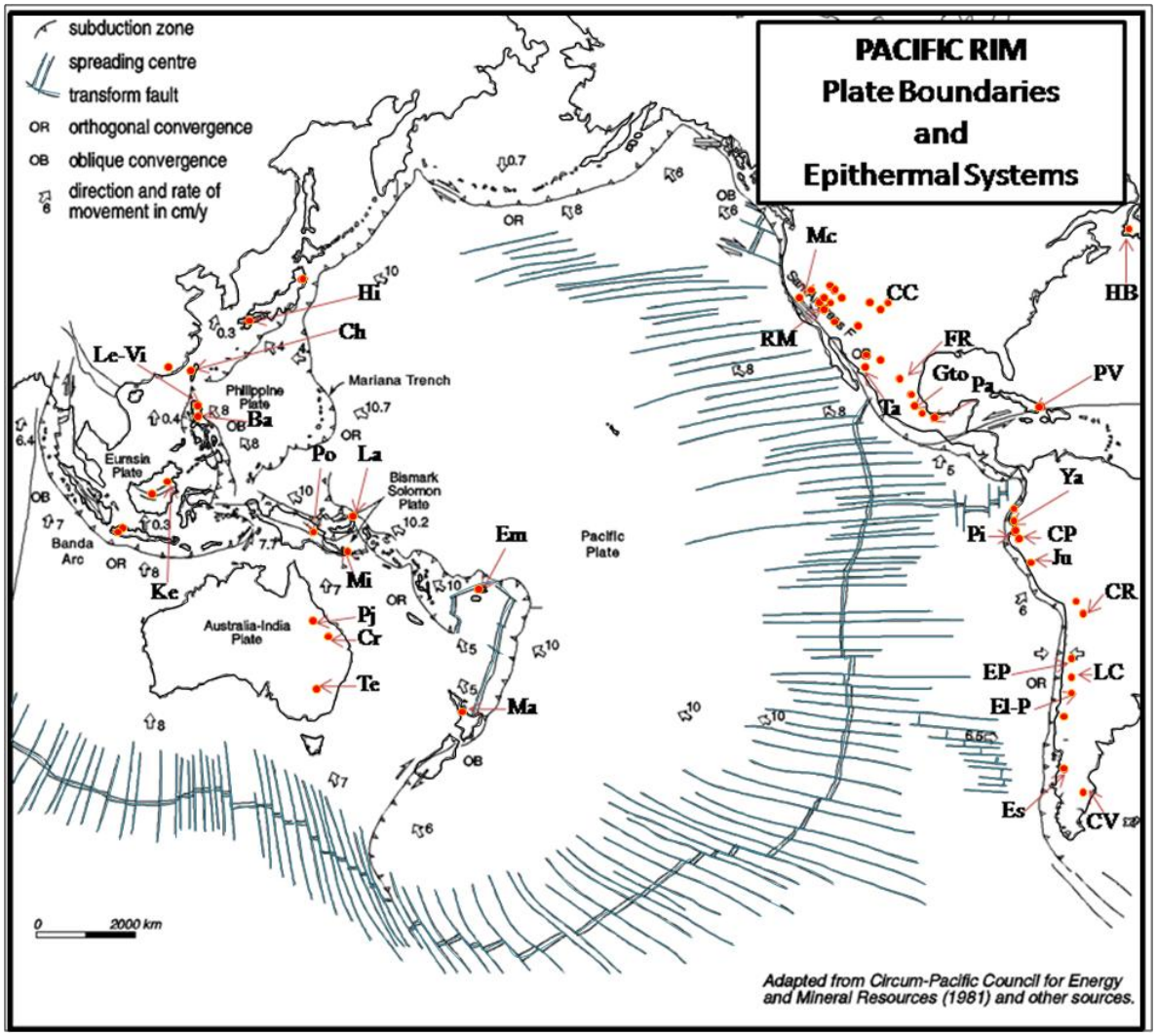

Fig. 1 Location of plate boundaries and epithermal deposits within the Pacific Rim, with some localities indicated by abbreviations. Abbreviations: Ba – Baguio district (Acupan); CC – Cripple Creek; Ch – Chinkuashih; Cr – Cracow; CR – Cerro Rico; CV – Cerro Vanguardia; EL-P – El Indio-Pascua; Em – Emperor; EP – El Penon; Es – Esquel; Fr – Fresnillo; HB – Hope Brook; Hi – Hishikari; Ju – Julcani; Ke – Kelian; La – Ladolam; Le-Vi – Lepanto-Victoria; LC – La Coipa; Ma – Martha Hill-Favona; Mc – McLaughlin; Mi – Misima; Pi – Pierina; Pj – Pajingo; Po – Porgera; PV – Pueblo Viejo; RM – Round Mountain; Ta – Tayoltita; Te – Temora; Ya – Yanacocha. Modified from Simmons *et al*. (2005) and Corbett and Leach (1997).

Table 1. General Characteristics of Epithermal Deposits (modified from Simmons *et al*., 2005; Corbett & Leach, 1997).

Classification based on Hedenquist *et al.* (2000), Einaudi *et al* . (2003), Silitoe & Hedenquist, (2003)	**Fluid (1)**	**Alteration mineral (2)**	**Expected minerals (2)**	**Associated and economic accesory minerals (1)**	**Gold fineness (1)**	**Composition of igneous rocks (2)**	**Tectonic environment (2)**
High Sulfidation	Acidic, oxidized, saline, SO2-dominant	Alunite, kaolinite (dickite), pyrophyllite, residual/vuggy silica	Pyrite-enargite, ± luzonite, covellite-digenite, famatinite, orpiment	High % pyrite, Au ± Cu, As with Te at high levels	High fineness (silver-poor)	Calc-alkaline, andesite-dacite	Magmatic arc in a neutral to mildly extensional stress state; compressive stress state uncommon but serves to suppress volcanic activity
Intermediate Sulfidation			Tenantite, tetrahedrite, hematite-pyrite-magnetite, pyrite, chalcopyrite, Fe-poor			Calc-alkaline, andesite-rhyolite	Magmatic arc in a neutral to mildly extensional stress state; compressive stress state rare
Low Sulfidation	Near neutral, reduced, dilute, H2S-dominant	Quartz-adularia ± illite, calcite	Arsenopyrite-loellingite-pyrrhotite, Fe-rich sphalerite-pyrite	Au ± Ag, Pb, Zn, Cu, with As, Te, Hg, Sb at high levels	Variable with depth, high fineness at depth (silver-poor), low fineness (silver-rich) at high levels	Calc-alkaline, alkaline, thoelitic bimodal basalt-rhyolite	Magmatic arc undergoing extension leading to rifting; postcolllisional rifting
Alterations	**Propylitic:** Quartz, K-feldspar (adularia), albite, illite, chlorite, calcite, epidote, pyrite; **Argillic:** Illite, smectite, chlorite, inter-layered clays, pyrite, calcite (sideritte), chalcedony; **Advanced argillic (steam heated):** Opal, alunite (white, powdery, fine-grained, pseudocubic), kaolinite, pyrite, marcasite; **Advanced Argillic (magmatic hydrothermal):** Quartz, alunite (tabular), dickite, pyrophyllite, (diaspore, zunyite); **Advanced argillic (supergene):** Alunite, kaolinite, halloysite, jarosite, Fe-oxides.						

Notes: (1) Data modified from Corbett and Leach (1997), and (2) Simmons *et al*. (2005).

sphalerite and pyrite, respectively (Simmons *et al*., 2005). Table 1 displays a summary of the characteristics of HS, IS and LS epithermal deposits.

Low sulfidation vein-type gold deposits are common in the Northeast Hokkaido Metallogenic Province (e.g., Utanobori, Omui, Hokuryu and Kitano-oh) and in other parts of Japan (e.g., Hishikari Au deposit in Kyushu). This deposit type occasionally forms within 1-2 km depth, but are generally within 500 m from the surface (e.g., Buchanan, 1981; Fig. 2). Metals are generally deposited from hydrothermal fluid below temperatures of 300 °C, commonly through the processes known as boiling and fluid mixing (e.g., Hedenquist *et al*., 2000). Ascending hydrothermal fluids from depth generally tend to be structurally controlled, and may flow laterally outwards to produce zoned alteration patterns during fluid neutralization (e.g., Buchanan, 1981; Fig. 2). Rising hydrothermal fluids may reach the surface, but may also experience events of trapping from overlying hosts rocks below surface. The buildup of fluid pressure in host rocks may finally escape through series of fractures, either induced by seismic events or hydraulic pressure. Fracturing results in fluid boiling as pressure is released, which in turn deposit metals. Episodic hydrothermal events and host rock trapping and fracturing produce colloform-crustiform bandings (e.g., Dong *et al*., 1995) having black metal-rich bands known as ginguro (e.g., Saunders, 1990). Mineralized fluids are commonly neutralized through the process of dilution producing an alteration assemblage. Abundant quartz-adularia and bladed calcite are indicative of boiling conditions (e.g., e.g., Hedenquist *et al*., 2000). Where hydrothermal fluids reach the surface, further cooling results in the deposition of silica sinter and mud pools (Fig. 2). Silica sinters are important as it indicates the paleosurface and pinpoints the upflow channel of hydrothermal fluids (e.g., Hedenquist *et al*., 2000). Only a few documented cases show the evidence of

mineralized quartz veins cross-cutting silica sinter, for example the Cerro Blanco mine in Guatemala (JDS Energy & Mining Inc., 2019) and the Mc Laughlin mine in California (Sherlock *et al*., 1995).

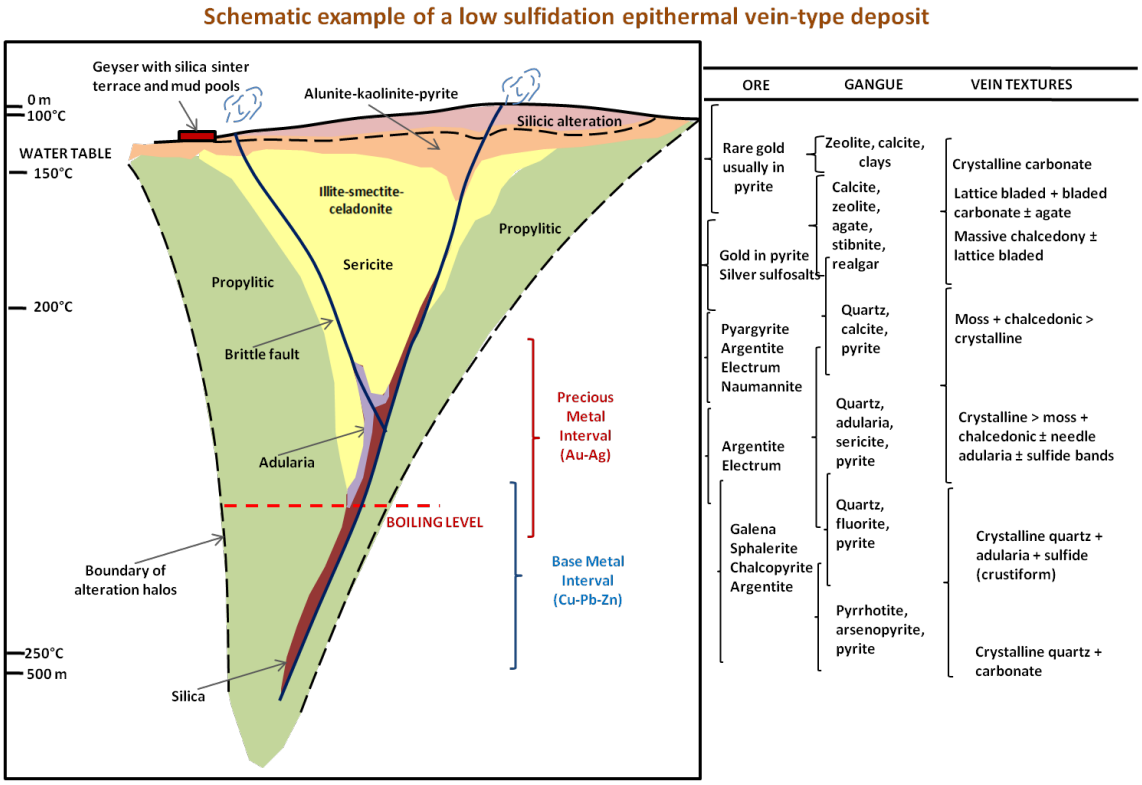

Fig. 2 Schematic example of a low sulfidation epithermal vein-type deposit. Modified after Buchanan (1981) and Morrison *et al*. (1990).

1.1.2 Locality of the studied deposits

The Utanobori and Omui gold deposits are located at the north east part of Hokkaido, approximately centered at 44°52’14.40’’N and 142°28’54.35’’E, and 44°32'9.60"N and 142°54'26.80"E, respectively, in the Northeast Hokkaido Metallogenic Province, Japan (Fig. 3). The Omu silica sinter is located approximately 9 km north of the Omui gold deposit (Fig. 3). The Northeast Hokkaido Metallogenic Province is host to epithermal vein-type Ag-Ag and Cu-Pb-Zn, vein and disseminated-type Hg,

volcanogenic massive sulfide Cu-Pb-Zn (Kuroko), and subaerial-volcanic exhalative hydrothermal FeS_2 and S deposits (Hasegawa *et al*., 1983; Yahata, 2002; Fig. 3). The Utanobori and Omui deposits were reported as Middle Miocene in age [Mnistry of International Trade and Industry (MITI), 1996; Yahata, 1999, 2002]. Formation age of Au-Ag and Cu-Pb-Zn deposits are older in the north from 15 Ma at Tokusei and from 13 Ma at Motokura, respectively, to the youngest Pleistocene age of the Seta Au (1.3-1.6 Ma) and 5.7 Ma at Yoroh Cu-Pb-Zn deposits in the south [Ministry of International Trade and Industry (MITI), (1994); Yahata, 2002].

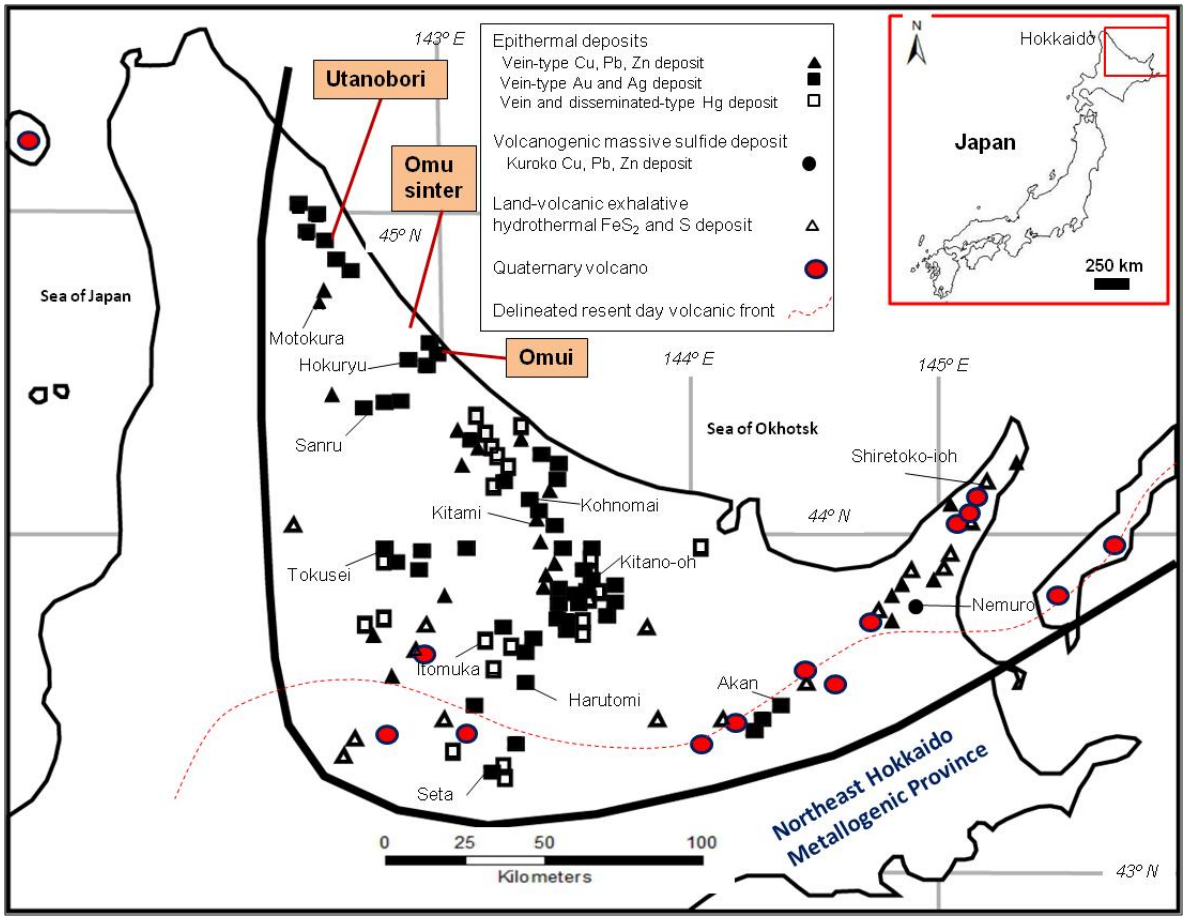

Fig. 3 Location map of the Utanobori and Omui Au-Ag vein-type deposit (in bold), Omu Sinter (in bold), and other epithermal, volcanogenic massive sulfide and land-volcanic exhalative hydrothermal deposits in the Northeast Hokkaido Metallogenic

(Figure 3 continued)

province, Japan (modified after Hasegawa *et al*., 1983; Yahata, 2002; Sorulen *et al*., 2019).

Hydrothermal mineralization in Miocene was closely related to felsic volcanism which shifted southward following the southward shift of volcanic events (Watanabe, 1996). The delineated present day volcanic front is represented by a chain of Quaternary volcanoes (Fig. 3).

1.1.3 Cathodoluminescence (CL) and trace element geochemistry of quartz

The optical and electromagnetic phenomenon known as cathodoluminescence occurs when a luminescence surface hit by electrons emits protons which may have wavelengths in the visible spectrum. The application of cathodoluminescence on quartz serves as a powerful tool to reveal its characteristics which are not easily distinguished under normal optical microscopy (e.g., Götze, 1996). Furthermore, an applications of cathodoluminescence combined with trace element geochemistry (using electron probe microanalysis, EPMA) on quartz provide a unique and powerful approach in acquiring information from quartz. The application of this technique on minerals including quartz aids in the identification of their chemical composition, structure, genetic characteristics and typomorphic properties (e.g., Pagel *et al.*, 2000). Primary, secondary and replacement textures and defect centers of crystals are easily identified using this technique; hence it is useful in the fields of igneous, metamorphic and sedimentary petrology in the crystallization, alteration and replacement processes that may be associated with crystal defects (e.g., Müller, 2000).

The variation in CL in minerals such as quartz can be caused by intrinsic defects (e.g., non-stoichiometry and structural imperfections) or extrinsic defects related with luminescence-active impurities such as trace elements (Marshall, 1988, Takahashi *et al*., 2008). Considering the substitution of trace elements in the quartz lattice (i.e., Si^{4+}), positively charged interstitial cations of H^{+}, Na^{+}, Li^{+}, K^{+} which charge compensate for Al^{3+} are common in hydrothermal quartz (e.g., Rusk *et al*., 2008; Müller *et al*., 2010). Comparing between magmatic and hydrothermal quartz, commonly, Al uptake is much more favored at pH>5 in hydrothermal quartz with Al contents up to 5000 ppm, and lower in magmatic quartz up to 200 ppm (Müller, 2000). The variation and high contents of Al in hydrothermal quartz may result from crystallization in a high pH aqueous solution (Merino *et al*., 1989) favoring Al uptake on favored crystal growth faces/sites which is dependent on temperature and growth mechanisms (e.g., Müller 2000). Götze *et al*. (1997) showed that the bulk Al content is quartz is higher than structurally incorporated, which may suggest that Al may not only occur as structurally incorporated, but also as impurity clusters or inclusions (e.g., Müller 2000). Al contents of quartz in vein quartz from the Alps is up to 12000 ppm (Mullis & Ramseyer, 1999), caused by larger ion radius of Al^{3+} in comparison to Si^{4+}, which may had caused deformation and structural weakening in the quartz lattice. Pfenninger (1961) suggested an explanation to the entrapment of impurity in quartz summarized by Müller (2000): Oversaturation of silica results in diffusion-controlled crystal growth and higher growth rates. At these rates the surface diffusion is too low to organize a planar face growth and cellular growth becomes dominant. Cellular growth results in the development of defect channels which may be filled with foreign elements. These defect channels, 20-50 nm in diameter, are parallel to the c-axis and surrounded by disordered SiO_2 boundary layers. They start to grow at

the structural channels due to the stepwise bond lacking between the tetrahedra. The competition between impurity segregation and lateral diffusion results in a broadening of the defect channels which finally may result in dendritic growth. Variations in CL emissions caused by defects in quartz reflect the physiochemical conditions of quartz during its growth, and thus provide signatures of its genetic conditions (e.g., Götze, 1996).

Early study on CL was done by Crookes and others during 1869 to 1879, who observed fluorescence and phosphorescence in substances when subjected to the negative discharge in high vacuum (e.g., Crookes, 1896). The first report on CL was produced by Goldstein (1907). The introduction of the electrum microscope since the 1960's provided further investigations into CL properties of substances subjected to electron bombardment. Though several studies were undertaken to understand CL with the application and combination of various techniques during the last decade (e.g., heterogeneous distribution of trace elements in quartz, Ramseyer & Mullis, 1990; e.g., structural and chemical variations within crystals, Marshall, 1988; e.g., CL of hydrothermal quartz, Perny *et al*., 1992; e.g., quartz phenocrysts in rhyolite, Watt *et al*., 1997), little is still known about the relation between CL properties, trace element distribution and petrogenesis of quartz.

1.2 Previous works on the Utanobori and Omui deposits and Omu silica sinter

1.2.1 Utanobori

The Utanobori deposit was discovered in 1929, and acquired by Sumitomo Metal Mining Co., Ltd. in 1934, and was operated until its closure in 1943 (MITI, 1996). Mineralized ore-bearing veins were exploited by underground mining techniques, where series of underground tunnels were constructed centered at Mt Kanayama at

levels about 52 m, 114 m, 142 m, 151 m, 173 m, and 200 m with respect to present day sea level. The adits range from 10 m to <220 m in length. Reported historical production includes crude ore of 19,141 t, with concentrates of 134 kg of gold and 708 kg of silver at average grades of 7 g/t and 37 g/t, respectively (MITI, 1996).

Geology of the Utanobori deposit was reported by Hasegawa *et al*. (1962), Osanai *et al*. (1962, 1963) and Yamaguchi (1981). In the Omui and Omu area, geology was reported by Suzuki *et al.* (1966). Mineralization of the Utanobori deposit and the Omui and Omu areas were reported by Komura *et al*. (1962), Geological Survey of Japan (GSJ) (1967) and Suzuki *et al*. (1966), respectively. Age dating on Tokushibetsu Agglomerate and a tuff of the Esashi Formation, a biotite-granite intrusive of the Hidaka Supergroup, a tuff breccia of the Ofuntanarumanai Formation, a Kinkomanai Lava and a Kemomanai Lava were reported by Shibata *et al*. (1981), Maeda *et al*. (1986), Koshimizu and Kim (1986), and Okamura *et al*. (1995), respectively in Utanobori. Ages of ore formation in the Kitami region were discussed by Ishihara (1998) and Yahata (2002). In the Omui and Omu area, ages of rock units were discussed by Suzuki *et al*. (1966), a Motoineppu Lava by Koshimizu and Kim (1987), a Inashinetsu Lava by Watanabe and Yamaguchi (1991), a Makahoronai Lava by Watanabe *et al*. (1995), and a Kamiomu Formation by Watanabe (1995). The tectonic model of epithermal gold mineralization in Northeast Hokkaido and genesis of vein hosting fractures in the Kitami Region of Hokkaido were discussed by Watanabe (1995, 1996), and a regional overview of precious and base metal deposits, settings and ages in the Northeast Hokkaido Metallogenic Province were discussed by Yahata (2002). Fluid inclusion microthermometry, drill core observation, X-ray diffractometry (XRD), electron probe micro-analysis (EPMA) and K-Ar age dating were performed by Ministry of International Trade and Industry (MITI) (1996) on the

Utanobori deposit. Three stages of quartz veining were recognized in Utanobori; an early stage of quartz-adularia band (black), middle stage consisting of chalcedony and quartz, and a late stage consisting of chalcedony and transparent quartz (MITI, 1996). Diamond drilling conducted at Utanobori included four drill holes, 7MAHH-1, 8MAHH-1, 8MAHH-2, and 8MAHH-3, with drilling lengths of 400 m, 300 m, 330 m, and 500 m, respectively, all orientated towards SE to SSE direction except for 8MAHH-3 which was oriented towards NW (MITI, 1996). The 7MAHH-1 drill collar was located approximately 50 m NE from Mt. Kanayama, aimed at testing beneath the historical mining area. The 8MAHH-1 and 8MAHH-2 were spaced at approximately 50 m intervals to the SW after 7MAHH-1, and 8MAHH-3 approximately 1020 m towards SW with respect to Mt. Kanayama. The maximum Au and Ag grades in veins intercepted in 7MAHH-1, 8MAHH-1, 8MAHH-2 and 8MAHH-3 were reported as 3.2 g/t Au and 5 g/t Ag at 232.30 m, 10.4 g/t Au and 12.2 g/t Ag at 251.25 m, 1.5 g/t Au and 3.5 g/t Ag at 260.30 m, and <0.01 g/t Au and <5 g/t Ag from 357 m to 358.50 m, respectively. MITI (1996) documented homogenization temperatures of fluid inclusion of the stage I quartz-adularia vein (n = 27), and the stage III quartz-adularia vein exhibiting euhedral and microcrystalline quartz (n = 28) ranged from 240 to 270°C, and 220 to 230°C (euhedral quartz) and 170 to 180°C (microcrystalline quartz), respectively. Homogenization temperatures of the silica sinter and calcite lens ranged from 280 to 310°C (n = 11) and from 150 to 160°C (n = 20), respectively, with reported boiling temperatures for calcite veins at 230 to 240°C (MITI, 1996). X-ray diffractrometry (XRD) conducted by MITI identified alteration mineralogy and divided them two groups; (1) altered Kinkomanai Lavas and (2) altered Esashi Group, with assumptions that K-feldspar formed as a result of hydrothermal alteration and plagioclase is a primary mineral (MITI, 1996).

In the Esashi Group, two alteration zones were identified; Zone I is characterized by quartz-sericite/smectite mixed layer, and Zone II is characterized by quartz-sericite. Zone I was sub-divided into three sub-zones; IE zone (quartz-sericite/smectite), IaE zone (quartz-sericite/smectite-plagioclase) and IbE zone (quartz-sericite/smectite-plagioclase-K-feldspar, coincides with the silicified zone), Zone II was also sub-divided into four sub-zones; IIE zone (quartz-sericite, coincides with the Utanobori mine), IIaE zone (quartz-sericite-plagioclase, distal to the silicified zone), IIbE zone (quartz-sericite-K-feldspar) and IIcE zone (quartz-kaolinite, acidic alteration zone which borders and rims the silicified zone). In the Kinkomanai Lavas, three zones were identified; (1) IK zone is characterized by cristobalite, tridymite and primary biotite, (2) IIK zone is characterized by quartz (after cristobalite and tridymite) accompanied with smectite, and (3) IIIK zone characterized by quartz accompanied by sericite/smectite and chlorite/smectite mixed layered clay. Electron probe micro-analysis (EPMA) on the mineralized quartz-adularia vein revealed the presence of electrum (AuAg), naumannite [$Ag_2(Se,S)$], fischesserite [$Ag_3Au(S,Se)_2$], chlorargyrite (AgCl) and bromargyrite (AgBr) solid solution, Ag-Sb-Fe-Cl-Br phase and goethite (MITI, 1996).

Undergraduate studies conducted by Suzuki (2015 MS) on the Utanobori deposit included petrography and paragenesis of a mineralized quartz-adularia vein (Figs. 4, 5) identification of alteration, ore and gangue minerals by microscopic observation and XRD analyses, scanning electron microscope with energy dispersive spectroscope (SEM-EDS) on ore minerals, and X-ray fluorescence (XRF) on the mineralized quartz-adularia vein. In the main mineralized quartz-adularia vein, 7 (I-a to I-g), 3 (II-a to II-c) and 2 (III-a to III-b) sub-stages were identified in the stage I, the stage II and the stage III, respectively with naumannite and electrum common in

the main silver-bearing bands (“ginguro”) of the sub-stages I-b and I-d of the stage I (Suzuki, 2015 MS).

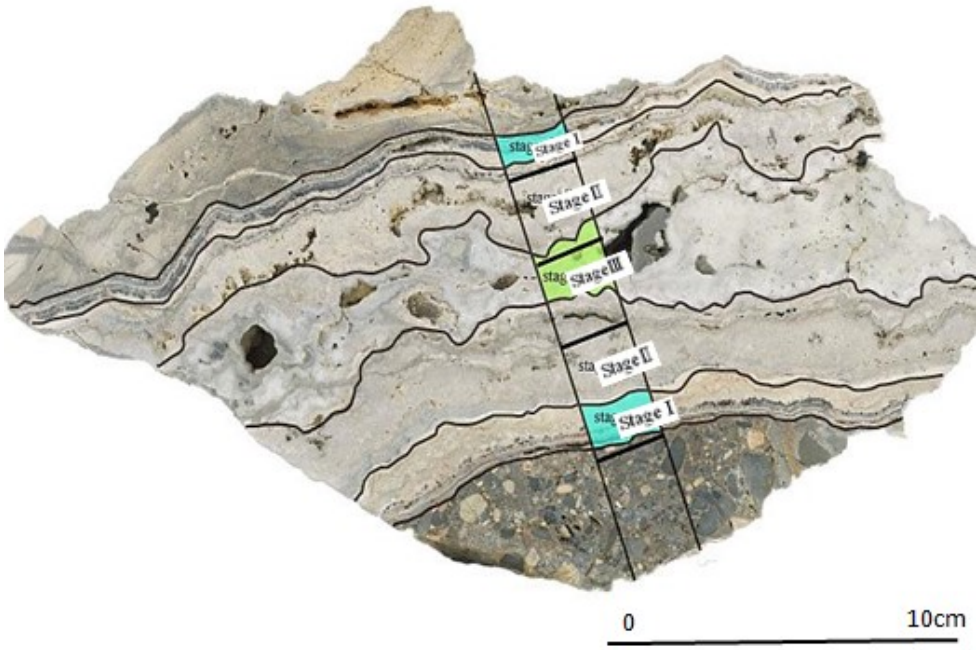

Fig. 4 The main ore-bearing quartz-adularia vein at Utanobori (Suzuki, 2015 MS).

Other ore minerals identified included an unknown Fe-Sb oxide, chloragyrite and bromargyrite. Ore minerals were commonly associated with microcrystalline quartz and slightly with adularia. The Au content of electrum determined from SEM-EDS analysis ranged from 51.0 to 55.3 at% Au (av. 52.5 at% Au, n=10), 61.6 to 67.3 at% Au (av. 65.7 at% Au, n=20), and 51.2 to 59.8 at% Au (av. 55.5 at% Au, n=5) in band I-b of the stage I, I-d of the stage I, and II-a of the stage II, respectively of the mineralized quartz-adularia vein (Suzuki, 2015 MS). An unknown Fe-Sb oxide identified in the quartz-adularia vein was proposed as either schafarzikite or tripuhyite based on the calculated ratio of Fe:Sb = 4:1.

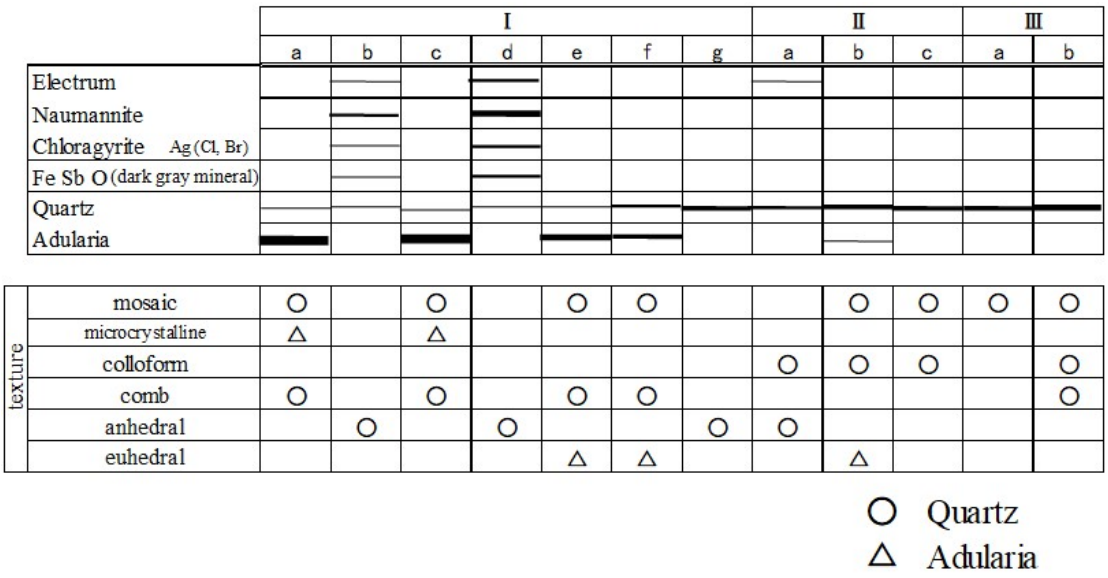

Fig. 5 Paragenetic sequence of the ore-bearing quartz-adularia vein at Utanobori (Suzuki, 2015 MS).

Undergraduate studies by Tanaka (2018 MS) also confirmed the presence of ore minerals and its association with gangue and alteration minerals as previously identified by Suzuki (2015 MS), and further attempted to determine the unknown Fe-Sb oxide with proposed chemical formula of $Fe_8Sb_2AlSiO_{12}(OH)_{17}$ determined by EPMA analysis. Average Se/(Se+S) ratio of naumannite calculated by Tanaka (2018 MS) ranged from 94.6 to 97.7at% in the stages I and II of the mineralized quartz-adularia vein.

1.2.2 Omui and Omu

Placer gold was identified in the Omui area during the early 1890s which eventually lead up to the discovery of a main gold-bearing vein called Honpi [MMIJ, 1990; Steffen, Robertson and Kirsten (SRK), 2018]. The Honpi was tested in 1921, and in 1925, Fujita Mining Co. commenced mining activity which included construction of a

100 m deep vertical shaft with four main and two sub-levels focused on extracting a 1 to 1.5 m main vein (Shuto, 1999; SRK, 2018).

Mining activity ceased in 1928, and production was reported at 0.34 t Au and 8.5 t Ag, equating to about 377.1 kg Au and 9255.6 kg Ag (Shuto, 1999, SRK, 2018). Between 1984 and 1985, geological mapping and nine diamond-drill holes were conducted, which delineated quartz and silicified floats boulders and the extent of mineralization below surface, respectively (Shuto, 1999; SRK, 2018).

In 2016, Irving Resources Inc. secured a mining license covering 2.98 km^2 of the Omui area, and an additional 50 prospecting licenses over an additional 152.03 km^2 of the area encompassing the entirety of the northeast-trending Omu volcanic graben (Irving Resources Inc., 2019). Also in 2016, Irving Resources Inc. filled 38 prospecting licenses covering 121.55 km^2 of the Utanobori area (Irving Resources Inc., 2019). During 2016, Irving resources Inc. discovered a 3.2 m high silica sinter (Omu sinter), and in 2019, applied a drilling permit to test the possibility of mineralized veins that may exist below the sinter (Irving Resources Inc, 2019).

Exploration activities by Irving resources Inc. and Mitsui Mineral Development Engineering Co. Ltd. (MINDECO) commenced in 2016 covering areas which include the Omui deposit and Omu sinter. MINDECO is a contractor of Irving Resources Inc. in Japan (SRK, 2018). Stream sediment sampling conducted in 2017 acquired gold (>0.5 ppm), silver (> 2.5 ppm), arsenic (150 ppm), and antimony (>15 ppm) values corresponding to the Omui deposit (SRK, 2018). Rock chip samples were also collected during the soil sampling program. A total of 12 rock-chip samples were collected from the Omu sinter which returned Au and Ag grades ranging from 0.17 to 1.52 g/t and 0.5 to 38 g/t, respectively (SRK, 2018). Abundant

quartz and adularia were identified in the silica sinter based on XRD analysis conducted in 2018 (SRK, 2018).

In 2017, gravity survey was conducted covering an area measuring approximately 18 x 18 km^2 which includes the Omui and Omu areas. Interpreted gravity data by Irving Resources Inc. shows a graben structure that trends NE-SW, with the Omui deposit and Omu sinter appearing to lie on the flanks of the interpreted graben structure (SRK, 2018; Fig. 6).

In 2017 and 2018, magnetic surveys [using an Unmanned Aerial Vehicle (UAV or "drone")] were conducted to better understand the structure in the Omui deposit and Omu sinter (SRK, 2018). Data obtained are yet to be interpreted by Irving Resources Inc. (SRK, 2018).

In 2018, high spatial resolution Light Detection and Ranging (LiDAR) topographic models was carried out as part of Irving Resources Inc. exploration (SRK, 2018). The UAV was also employed in this survey. Interpreted data and survey reports are still in preparation (SRK, 2018).

Nearing the end of 2018, Irving Resources Inc. received a mining permit for its Omu gold silver project, which includes the Omui deposit (Irving Resources Inc. news release, October 30th 2018; SRK, 2018).

In early 2019, Irving resources Inc. conducted a drilling program with two diamond drill holes totaling 786 m at the Omu sinter (Irving Resources Inc. news release, April 22nd 2019). The first hole 19OMS-001 tested the full width of the targeted N-S trending magnetic low at Omu sinter, and was oriented northwest with an inclination of -45 degrees and reached a depth of 515 meters (Irving Resources Inc. news release, April 22nd 2019; Fig. 6). The second hole 19OMS-002 was designated to test deeper areas under the zone of intense silicification and clay alteration

encountered in hole 19OMS-001. Hole 19OMS-002 was collared 210 m northwest of hole 19OMS-001 and oriented southwest with an inclination of -60 degrees and a depth of approximately 271 m and progressing (Irving Resources Inc. news release, April 22nd 2019; Fig. 6).

In hole 19OMS-001, rhyolite and lesser andesite and volcaniclastic intervals were encountered. Intervals of intense silicification and/or clay alteration were observed at the top of bedrock to 91 m, and moderate to strong clay alteration and /or silicification from 370 to 515 m (Irving Resources Inc. news release, April 22nd 2019). Zones of disseminated and/or veinlet sulfide (pyrite) mineralization were observed especially in the intervals from 88 to 119 m, 210 to 227 m, 359 to 467 m and 479 to 515 m (Irving Resources Inc. news release, April 22nd 2019). The nature of alteration and mineralization observed in hole 19OMS-001 confirms the presence of a significant hydrothermal system measuring at least 350 m wide (Irving Resources Inc. news release, April 22nd 2019).

In hole 19OMS-002, rhyolite was predominantly encountered. Hydrothermal alteration which includes silicification and/or clay alteration were observed at surface to 217 m, and notable zones of moderate to heavy disseminated and/or veinlet sulfide (pyrite) mineralization were observed from 129 m to 169 m and 182.5 to 271 m (Irving Resources Inc. news release, April 22nd 2019).

The additional hole 190MS-003 was drilled in a south-southeasterly direction at an inclination of -55 degrees and was designed to test the extension of mineralization encountered in hole 190MS-002 (Fig. 6; Irving Resources Inc. news release, May 22nd 2019). Silicification and vein breccias sulfide mineralization were encountered at depths beginning around 350 m and ended at the intersection of an east west structures at 426 m (Irving Resources Inc. news release, May 22nd 2019).

A new hole, 190MS-004 had been collared approximately 140 m south-southeast of hole 190MS-003, with an east-southeasterly orientation and an inclination of -60 degrees (Fig. 6; Irving Resources Inc. news release, May 06th, 22nd, 2019). Upon writing of this chapter, drilling data for hole 190MS-004 was yet to be released by Irving Resources Inc.

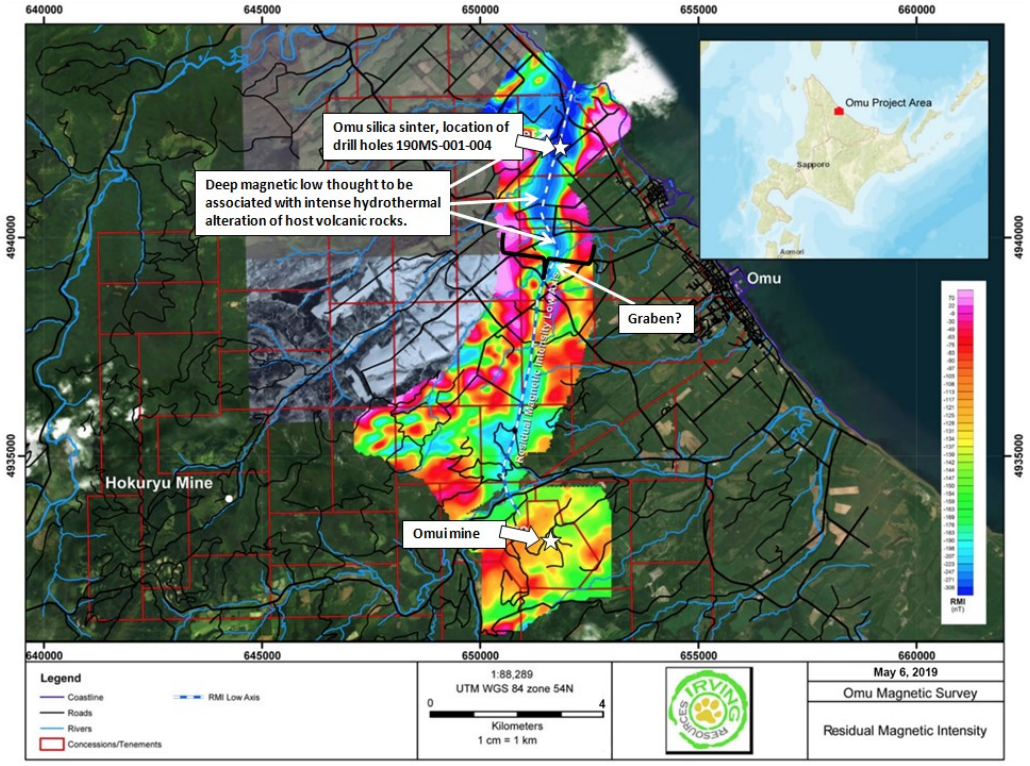

Fig. 6 Regional Gravity Anomaly map with an interpreted graben structures (Irving Resources Inc. news release, May 06th, 2019). Shown also are four diamond drill holes by Irving Resources Inc. during their drilling program in early 2019 (Irving Resources Inc. news release, May 06th, 22nd, 2019).

Undergraduate studies conducted by Kuzumaki (2018 MS) discussed about the gold mineralization and ore-forming conditions at the Omui deposit. Field work conducted in the Omui area identified altered host rocks of the Inashibetsu Lava,

rhyolite dike, rhyolite tuff breccias, rhyolite lapilli tuff and sandstone and mudstone of the Kamiomu Formation. Methodologies employed include XRD, microscopic observation, SEM-EDS, inductively coupled plasma-mass spectrometer (ICP-MS) and atomic absorption spectroscopy (AAS) analyses, EPMA, and fluid inclusion microthermometry studies. Alteration mineralogy determined by XRD analysis (n= 30) the vicinity of the Omui area revealed the presence of silicification that characterizes the central zone of hydrothermal activity near the Honpi ore zone, surrounded by quartz ± K-feldspar ± chlorite ± cristobalite ± calcite, to smectite ± quartz ± K-feldspar and quartz ± K-feldspar ± kaolinite ± illite proximal to distal with respect to the ore zone (Kuzumaki, 2018 MS). Ore minerals identified by microscopic observation in the Honpi ore-vein (e.g., Fig. 7) are electrum, argentite and stephanite in the matrix of microcrystalline quartz with kaolinite at places. SEM-EDS analysis was employed to aid the identification of the ore minerals.

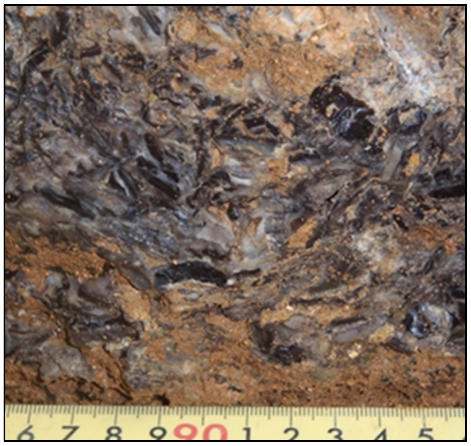

Fig. 7 The Honpi ore at Omui deposit (Kuzumaki, 2018 MS).

Data from ICP-MS and AAS analysis were utilized to generate anomaly maps and construct the alteration box plot (after Large *et al*., 2001) in the vicinity of the Omui deposit. The gold and silver contents of the black brecciated part and milky

white part of the ore-vein range from 0.9 to 194 ppm Au and 30.4 to 3638 ppm Ag and from 0.8 to 124 ppm Au and 0.2 to 4512 ppm Ag, respectively. The arsenic, silver, antimony anomaly maps show values >20 ppm, >20 ppm, and >5 ppm, respectively in the vicinity of the Omui deposit. The alteration box plot shows that values of Alteration Index (AI) and Chlorite-Carbonate-Pyrite Index (CCPI) increase towards the chlorite pyrite field, commonly from altered and mineralized rhyolite lapilli tuff. The Au content of electrum determined using EPMA ranges from 29.9 to 49.3 at% Au (av. 42.6 at% Au). Homogenization temperatures and salinity of the two-phase liquid-vapor-fluid inclusions of the Honpi vein range from 200 to 230°C, and from 5 to 5.7 wt. % NaCl, respectively, with ore-forming depth estimated at 191.7 m to 237.8 m from the paleo-water table.

A graduate study by Zeeck (2018 MS) discussed about the role of fluid flashing in the formation of high-grade, low sulfidation epithermal deposits, applying Omui deposit as a case study. Microscopic analysis, cathodoluminescence microscopy, SEM analyses and fluid inclusion studies were employed. The study showed that the quartz-vein exhibits a wide range of textures that represents primary growth patterns, and in addition, indicative of recrystallization and silica precursor phases of other vein minerals. Episodic mineralization was concluded based on crustiform, brecciated and alternating band structures associated with ore minerals. Densely packed micro-spheres of silica were also observed in the study, concluding that mosaic quartz formed from the recrystallization of non-crystalline silica precursor phase. The study also concluded that the colloform bands with relict microsphere textures were formed through rapid silica and ore mineral deposition within the veins at high temperatures, presumably involving flashing of hydrothermal fluids at depths over 400 m below the paleo-surface.

Table 2 Summary of previous works on the Utanobori and Omui Au deposits and Omu silica sinter in the Northeast Hokkaido Metallogenic Province, Japan.

Utanobori Au Deposit	Omui Au Deposit and Omu Silica sinter
1929: Deposit discovered (MITI, 1996). **1934:** Acquisition by Sumitomo Metal Mining (Utanobori mine) and construction of cyanidation plant, production includes **crude ore of 19,141 t, concentrates of 161 kg Au and 971 kg silver, and grades of 7 g/t Au and 37 g/t Ag** (MITI, 1996). **1943:** Mine closure **2016 till present:** 38 prospecting licenses filled by Irving Resources Inc. covering 121.55 square kilometers of the Utanobori area (Irving Resources Inc., 2019)	**1980s:** Placer Au discovered in Omui (SRK, 2018) **1925:** Fujita Mining Co. commence mining in Omui (SRK, 2018) **1928:** Mining activities ceased in Omui, production reported at **0.34 t Au and 8.5 t Ag** (SRK, 2018) **2016:** Irving Resources Inc. secured a mining license covering 2.98 square kilometer of the Omui area, additional 50 prospecting licenses over 152.03 square kilometer of the area encompassing the entirety of the northeast-trending Omu Volcanic Graben (Irving Resources Inc., 2019). Omu silica sinter discovered. **2018:** Irving Resources Inc. was offered a drilling permit to test the possibility of vein existance below the Omu silica sinter (Irving Resources Inc., 2019).
Geology: Hasegawa *et al*. (1962), Sekai *et al*. (1962), Osana *et al*. (1962, 1963), and Yamaguchi (1981).	**Geology:** Suzuki *et al*. (1966).
Mineralization: Komura *et al*. (1962), Geological survey of Japan (1967) and Yahata (2002).	**Mineralization:** MMIJ (1990), Sillitoe (1993), and Yahata (2002)
Age dating: Shibata *et al*. (1981) - K-Ar on Esashi Formation-tuff bulk of 13.8 +/- 0.9 Ma, Tokushibetsu agglomerate of 13.7 +/- 0.7 Ma; Maeda *et al*. (1986) – K-Ar on biotite granite of the Hidaka Supergroup of 16.5 Ma; Koshimizu and Kim (1986) – K-Ar on tuff breccia of the Ofutarumanai Formation (OF) at 14.4 Ma; Okamura (1995) – Rb-Sr on dacite of OF at 14 Ma, and MITI (1996).	**Age dating:** Suzuki *et al*. (1966), Koshimizu and Kim (1987) -Motoinepu Lava 12.0 +/- 0.9 Ma, Watanabe and Yamaguchi (1991) - Inashibetsu Lava 9.8 +/- 0.5 Ma, Watanabe *et al*. (1995) - Nakahoronai Lava 12.9 +/- 0.5 Ma, Watanabe (1995) - Kamiomu Formation - 14.3 +/- 1.0 Ma.

Table 2 (continued)

Epithermal tectonic model and genesis of vein hosting fractures in the Kitami Region: Documented by Watanabe (1995,1996).

Fluid inclusion, drill core observation, XRD, EPMA and K-Ar dating (Kinkomanai lava -dacite bulk of 12.1 +/- 0.1 Ma, mineralization on adularia - 12.1 +/- 0.6 Ma): MITI (1996).

2015 (Akita University): Bachelor thesis by Kana Suzuki.
Stages of mineralization and paragenesis sequence

Identification of alteration, ore and gangue minerals (microscopic observation)
SEM-EDS on ore minerals
XRD analysis (bulk and clay), and XRF mapping

2018 (Akita University): Bachelor thesis by Tanaka So.
Microscopic observation of ore and gangue minerals
XRD analysis

SEM-EDS on ore minerals
EPMA on ore minerals

2018 (Akita University): Bachelor thesis by Keigo Kuzumaki.

Identification of alteration, ore and gangue minerals (microscopic observation)

SEM-EDS on ore minerals
XRD analysis (bulk and clay)
ICP-MS
AAS
Fluid Inclusion microthermometry

2018 (Colorado School of Mines): Master thesis by Lauren Zeeck.
Microscopic observation of ore and gangue minerals
Cathodoluminescence microscopy
SEM analysis
Fluid Inclusion microthermometry

1.3 Aim and significance of this study

Provided the previous studies in section 1.2, it is noted that after mining activities ceased operations in 1943 and 1928 in Utanobori and Omui, respectively, very few exploration activities and research work commenced which were focused in reexamining the two deposits (e.g., Table 2). Published scientific information on the Utanobori and Omui gold deposits are few, and none for the newly discovered Omu silica sinter.

Given the recent exploration activities conducted by Irving Resources Inc. and Japan Gold in the Northeast Hokkaido Metallogenic Province, it is crucial to understand that mineral exploration in Japan had not been fully carried out since the closure of mines as discussed by Arribas and Mizuta (2017). An example of such is the discovery of the Omu silica sinter by Irving Resources Inc. in 2016, suggesting that not only exploration activities was limited during past activities, but also scientific information and techniques in discovering new deposits were not yet made available or readily understood (e.g., Arribas and Mizuta, 2017). Low-sulfidation vein-type deposits in the Northeast Hokkaido Metallogenic Province are closely related with silica sinters, where close proximity of silica sinters and quartz veins were observed at the Utanobori, Omui and Kitano-oh deposits as examples (Fig. 3).

Given the scarce available published information and understanding of the Utanobori and Omui Au deposits and the Omu silica sinter, this study is important in making available scientific information of the three areas of interest mentioned, and to aid in exploration activities and understanding of the type of low sulfidation epithermal vein-type Au systems in the Northeast Hokkaido Metallogenic Province. Furthermore, the study focuses in providing the first spot analysis using electronprobe microanalysis on epithermal quartz in the Northeast Hokkaido Metallogenic Province.

This study will also contribute towards further research in understanding trace element contents of epithermal quartz which is a topic of interest in modern research. The trace element contents of quartz were studied on a mineralized quartz-adularia vein in the Utanobori deposit.

This study is also significant to provide new age data on mineralization, silica sinter formation and related igneous events of the Utanobori and Omui Au deposits and the Omu silica sinter.

The study also focuses on the quartz textures of the Utanobori quartz-adularia veins and its implications to mineralization. This study will be the first published information on quartz textures of the Utanobori deposit.

1.4 Objectives

The primary ojective of this study is to understand the characteristics of the silica sinters and ore-bearing veins and their relationship to mineralization and associated volcanic events in the Utanobori and Omui Au deposits and the Omu silica sinter. Furthermore, the research is aimed at to make available scientific information for the Utanobori, Omui and Omu areas.

1.5 Thesis layout

This thesis presents the research works conducted on the Utanobori, Omui and Omu areas which are presented in Chapters 3, 4 and 5. Chapter 3 and 4 focuses on the Utanobori gold deposit, and Chapter 5 is focused on the Omui gold deposit and the Omu silica sinter. The Chapters 2 and 4 contents were prepared for publication which is in line with the objective of the studies (which is to publish scientific information on the Utanobori, Omui and Omu areas).

The Chapter 1 of thesis was aimed to inform about the types of epithermal deposits while focusing on the low sulfidation vein-type Au-Ag system. A review on previous studies provides an insight of what have been done, are currently done or future plans on the Utanobori and Omui Au deposits and the Omu silica sinter. Aim and significance of this study shows the importance of this research and its aim in solving and providing information in solving geological problems in the three areas. The objective focuses on the main purpose of the study achieved through the process and application of the scientific methods.

The Chapter 2 presents the “Mineralogical and Geochemical Characteristics of the Utanobori Gold Deposit in Northern Hokkaido, Japan”. This Chapter summarizes the research conducted in Utanobori, and the contents of this Chapter have been published by Resource Geology Journal.

The Chapter 3 summarizes the research on the “Occurrence of the Fe-Sb Oxide Mineral in the Utanobori Gold Deposit in Northern Hokkaido, Japan”.

The Chapter 4 presents the summary of the research on the Omui Au deposit and Omu silica sinter entitled, “The Omui Gold Deposit and Omu Silica Sinter in Northeastern Hokkaido, Japan”.

In Chapter 5, a general conclusion is presented uniting the discussions presented in the thesis.

CHAPTER 2

MINERALOGICAL AND GEOCHEMICAL CHARACTERISTICS OF THE UTANOBORI GOLD DEPOSIT IN NORTHERN HOKKAIDO, JAPAN

Abstract

The Utanobori gold deposit is a low sulfidation epithermal vein-type deposit located in northern Hokkaido, Japan. The deposit is hosted by Middle to Late Miocene Esashi Formation, which consists of conglomerate, sandstone, and tuff. These rocks were altered and alteration grades from the deposit outward, silicified zone → K-feldspar + illite ± chlorite/smectite mixed layer ± calcite zone → least altered zone. Kaolinite alteration observed proximal to the silicified zone is interpreted as a product of alteration by steam heated water. The silica sinters display milky white and orange to reddish-brown layers ranging from <1 cm to >12 cm in thickness per layer, with a total thickness ranging from 30 cm to approximately 1 m. The quartz-adularia veins observed in this study either contain ginguro band which correspond to the main gold-bearing vein commonly observed at old mine adits (Type 1 Veins), or without ginguro band and contain minor adularia and are observed to cross cut the silica sinters (Type 2 Veins).

Type 1 Veins are divided into three stages with twelve to fourteen sub-stages. Ore minerals identified include electrum, naumannite, chlorargyrite, bromargyrite, an unidentified Fe-Sb mineral and an Fe-(Sb)-As bearing mineral and trace pyrite. These ore minerals were formed in the main mineralization stages I (bands I-b and I-d) and II (band II-a). Trace amounts of electrum was observed in the bands I-a, I-c, I-f and I-g, II-d, and III-b. Primary, recrystallization and replacement quartz textures observed in this study are colloform, zoning and comb, mosaic, flamboyant, ghost-sphere and

feathery, and pseudo-acicular, respectively. Scanning electron microscopy with cathodoluminescence (CL) images show that CL-dark microcrystalline quartz exhibiting colloform (ghost-sphere) texture is closely associated with ore minerals in Type 1 Vein and Type 2 Vein with ore minerals scarcely associated with adularia. Ore minerals are observed to associate with CL-dark microcrystalline quartz of Type 2 Vein that cross cut the silica sinter. Recrystallization, replacement and primary comb-zoned textures commonly display CL-dark, CL-intermediate, and CL-bright banding. Concentrations of Al, Fe, K, Ti, and Mn of quartz of the Type 1 Vein and silica sinter were determined using an electron probe micro-analyzer. In Type 1 Vein, Al and K contents of CL-dark microcrystalline quartz exhibiting colloform (ghost-sphere) texture are commonly >1000 ppm. This may imply that ore minerals were crystallized from alkaline, silica supersaturated fluids at temperatures <200ºC which initially deposited amorphous silica with primary colloform texture (associated with metals) that were recrystallized to microcrystalline quartz. The Au content of electrum determined by a scanning electron microscope with energy dispersive spectroscopy ranges from 51.0 to 55.3 at% Au (av. 52.5 at% Au), 61.6 to 67.3 at% Au (av. 65.7 at% Au), and 51.2 to 59.8 at% Au (av. 55.5 at% Au) in band I-b, I-d, and II-a, respectively of Type 1 Vein. The $\delta^{34}S_{CDT}$ values of two fine-grained disseminated pyrites in the altered conglomerate and bedded tuff in the argillic altered zone are -4.3 ‰ and -4.2 ‰. Mineralization ages of Type 1 Vein of the stages I, II and III by Ar-Ar dating determined on adularia is 13.6±0.06 Ma, 13.6±0.07 Ma, and 13.6±0.06 Ma, respectively. K-Ar age determined on adularia in silica sinter and on whole-rock of glassy rhyolite of the Esashi Formation is 15.0±0.4 Ma and 14.6±0.4 Ma, respectively. From radiometric age dating, silica sinter that was associated with

rhyolitic volcanism formed prior to mineralization associated with rhyolitic and andesitic volcanism.

2.1 Introduction

The Utanobori deposit is an epithermal vein-type gold deposit (Yahata, 2002) located in the northeastern part of Hokkaido, Japan. Age of mineralization of the Utanobori deposit was reported as Middle Miocene [Ministry of International Trade and Industry (MITI), 1996; Yahata, 2002]. The deposit was discovered in 1929, and acquired by Sumitomo Metal Mining Co., Ltd. in 1934, and was operated until its closure in 1943 (MITI, 1996). Reported historical production includes 19,141 t of crude ore, with concentrates of 134 kg of gold and 708 kg of silver at average grades of 7g/t and 37g/t, respectively (MITI, 1996). In 2016, Irving Resources Inc. filed 38 prospecting licenses covering 121.55 km^2 of the Utanobori area (Irving Resources Inc., 2018).

Veins that carry gold at the Utanobori deposit are hosted in sedimentary and volcanic rocks of the Esashi Formation (MITI, 1996). The deposit is centered on Mt. Kanayama, a resistant silicified ridge that trends northeast to southwest. Silica sinters and quartz veins are observed as outcrops, or as scattered floats (e.g., MITI, 1996).

Geology of the Utanobori deposit was reported by Hasegawa *et al*. (1962), Osanai *et al*. (1962, 1963) and Yamaguchi (1981). Mineralization was reported by Komura *et al*. (1962) and the Geological Survey of Japan (GSJ) (1967). Age dating on a Tokushibetsu Agglomerate and a tuff of the Esashi Formation, a biotite-granite of the Hidaka Supergroup, a tuff breccia of the Ofuntanarumanai Formation, a Kinkomanai Lava and a Kemomanai Lava were reported by Shibata *et al*. (1981), Maeda *et al*. (1986), Koshimizu and Kim (1986), Okamura *et al*. (1995), respectively. The tectonic model of epithermal gold mineralization in Northeast Hokkaido and

genesis of fractures that host veins in the Kitami Region of Hokkaido were discussed by Watanabe (1995, 1996). Fluid inclusion microthermometry, drill core observation, X-ray diffractometry (XRD) on altered host-rocks, electron probe micro-analysis (EPMA) on ore minerals and K-Ar age dating on a quartz-adularia vein and Kinkomanai Lava were performed by MITI (1996).

In this study, stages in representative quartz veins and silica sinters were identified and classified according to mineralization style. Data of alteration mineralogy identified using XRD analysis on altered host rocks of the Esashi Formation are from Sorulen *et al*. (2019). Microscopic observation of representative quartz veins and silica sinters was conducted. Inductively coupled plasma-mass spectrometer (ICP-MS) and atomic absorption spectroscopy (AAS) analyses were conducted to determine the metal contents of the representative samples. Scanning electron microscope with energy dispersive spectroscope (SEM-EDS) semi-quantitative analysis was used on the representative quartz veins and silica sinter to identify minerals present and their compositions. Data of the composition of electrum determined by SEM-EDS analysis are from Sorulen *et al.* (2019). High-resolution cathodoluminescence (CL) images were taken for each representative sub-stage of quartz veins and silica sinter, with back scattered electron (BSE) and secondary electron images (SEI). From the BSE and CL images, the K, Fe, Al, Ti and Mn concentration of quartz of the representative sub-stages of quartz veins and silica sinter were analyzed using EPMA to understand the relationship between quartz textures, ore minerals and trace elements of quartz. Radiometric age dating was conducted on the basis of Ar-Ar method on adularia in stages I, II and III of a gold mineralized quartz-adularia vein, and K-Ar method on adularia intercalated in a silica sinter and a rhyolite sample from the Esashi Formation. Sulfur isotope analysis was

also conducted on pyrite. The aim of the study is to reveal the characteristics of the quartz veins and its relationship to mineralization and to elucidate the timing of quartz vein and silica sinter formation related to igneous activities.

2.2 Geological background

The Utanobori gold deposit is located in the northeastern part of Hokkaido, centered at 44°52'14.40''N and 142°28'54.35''E in the Northeast Hokkaido Metallogenic Province, Japan (Fig. 8).

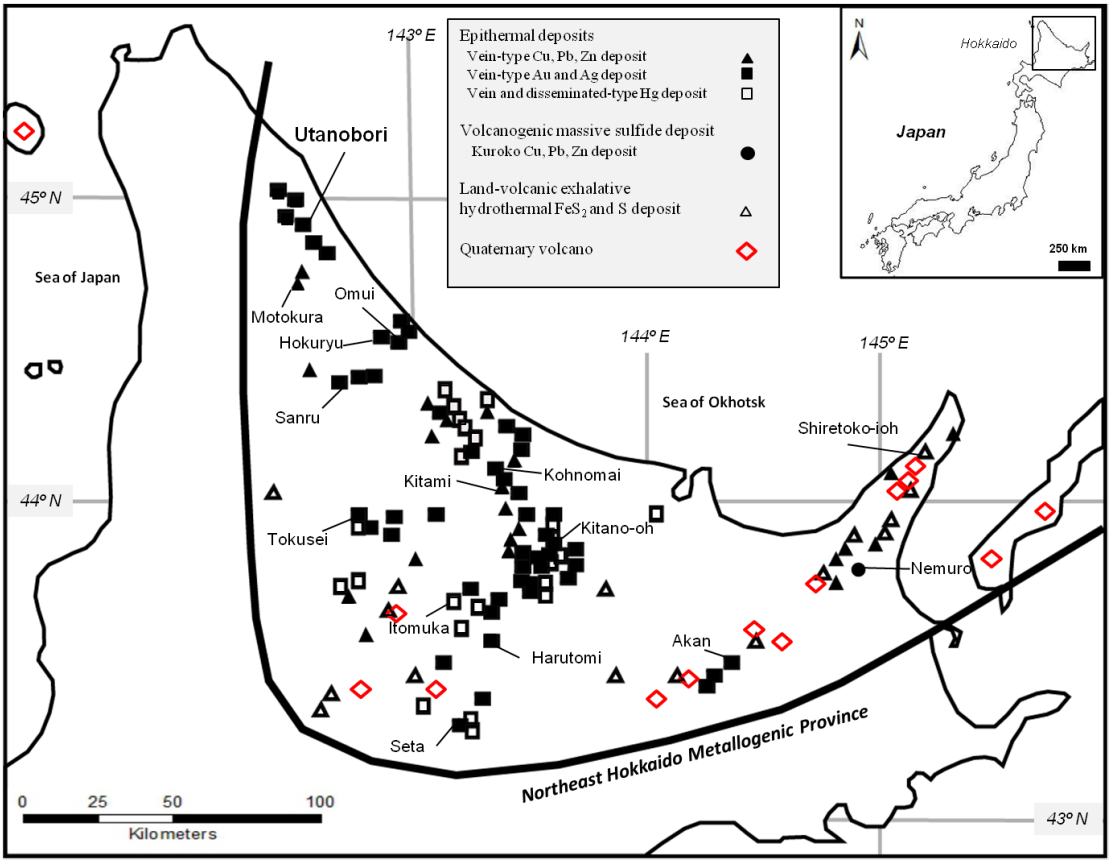

Fig. 8 Location map of the Utanobori deposit and other epithermal, volcanogenic massive sulfide and land-volcanic exhalative hydrothermal deposits in the Northeast Hokkaido Metallogenic province, Japan (modified from Hasegawa *et al.*, 1983; Yahata, 2002; Sorulen *et al.*, 2019).

The Northeast Hokkaido Metallogenic Province host epithermal vein-type Au-Ag and Cu-Pb-Zn, vein and disseminated-type Hg, volcanogenic massive sulfide Cu-Pb-Zn (Kuroko), and subaerial-volcanic exhalative hydrothermal FeS_2 and S deposits (Hasegawa *et al*., 1983; Yahata, 2002). Formation age of Au-Ag and Cu-Pb-Zn deposits are older in the north at 15 Ma at Tokusei and at 13 Ma at Motokura, respectively, to the youngest Pleistocene age of the Seta Au deposits (1.3-1.6 Ma) in the south (MITI, 1994; Yahata, 2002). Hydrothermal mineralizations in Miocene were closely related to felsic volcanism which shifted southward following the southward shift of volcanism (Watanabe, 1996). The present-day volcanic front is represented by a chain of Quaternary volcanoes (Fig. 8)

The Utanobori deposit sits atop a basement consisting of mélange matrix of Cretaceous to Early Paleogene accretionary complex of the Hidaka Supergroup made up of slate, sandstone, chert, and limestone with tuff (Fig. 9A; Yamaguchi, 1981; MITI, 1996). Veins associated with mineralization at the Utanobori deposit are hosted in the conglomerate, sandstone, siltstone and tuff of the Middle to Late Miocene Esashi Formation, which unconformably overlay the Hidaka Supergroup [Fig. 9A; Yamaguchi, 1981; MITI, 1996]. Tuff belonging to the Esashi Formation had been dated at 13.8 Ma (Shibata *et al*., 1981; MITI, 1996). The Esashi Formation was then covered by the Kinkomanai Lava and Kemomanai Lava, of ages 14 Ma and 12.1 ± 0.6 Ma from dacite and 6.6 Ma from basalt, respectively (Fig. 9A; Okamura *et al*., 1995; MITI, 1996). Late Miocene to Pliocene sandstone and conglomerate of the Penke Formation unconformably overlay the former rock units, and outcrops toward the south to southwest of the deposit (Fig. 12A; Yamaguchi, 1981; MITI, 1996; GSJ, 2009).

Distribution of silicified rocks, quartz veins, and silica sinter floats and

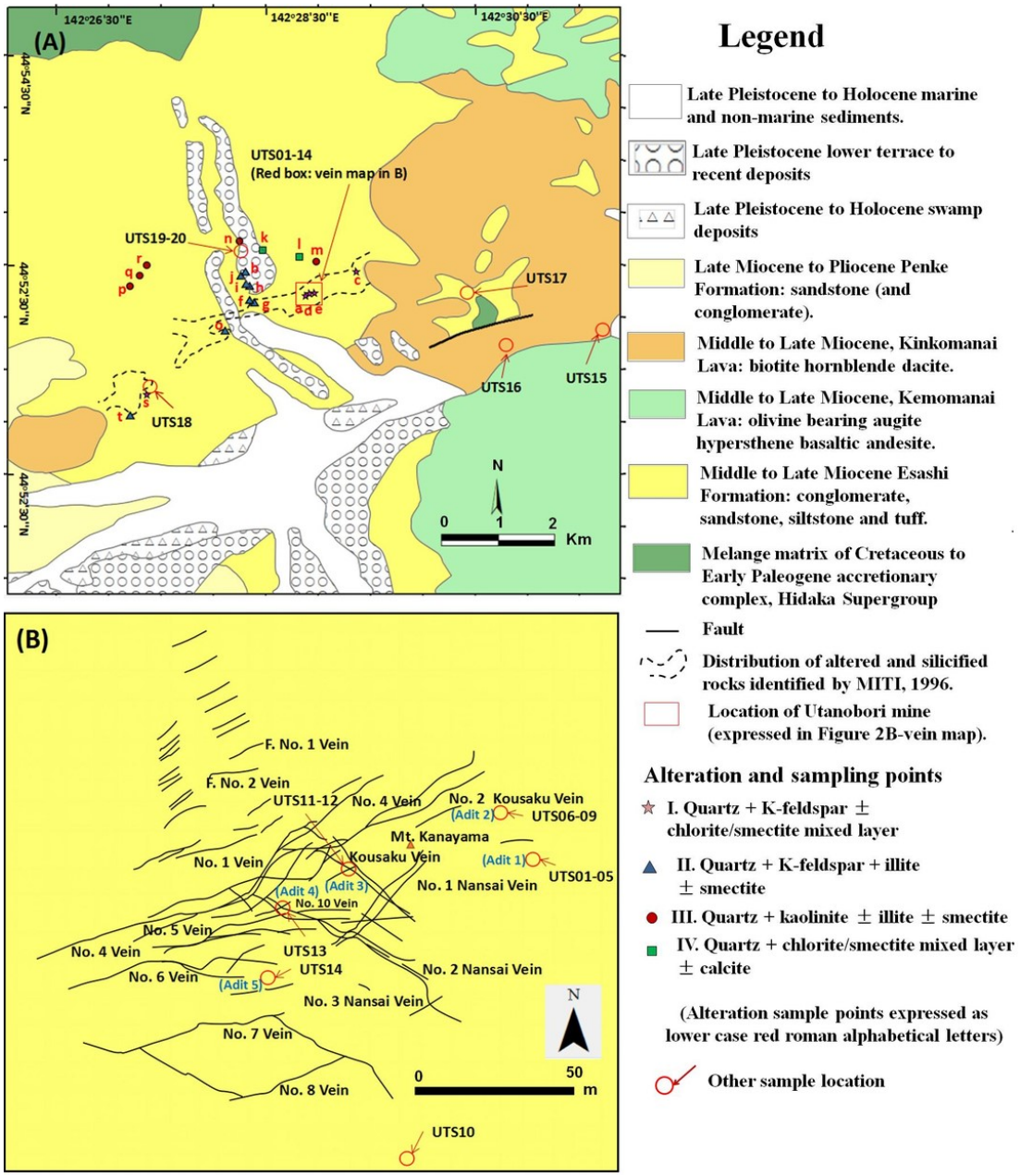

Fig. 9 (A) Geologic and alteration map, and (B) vein distribution map showing sample localities and mine adits visited in the Utanobori deposit (modified after Yamaguchi, 1981; GSJ, 2009; MITI, 1996). Alteration assemblages after Sorulen *et al*. (2019).

outcrops identified by MITI (1996) trend generally NE-SW (Fig. 9A; MITI, 1996). Alteration types identified by MITI (1996) are (I) quartz + K-feldspar ±

chlorite/smectite mixed layer, (II) quartz + K-feldspar + illite ± smectite, (III) quartz + kaolinite ± illite ± smectite and (IV) quartz + chlorite/smectite mixed layer ± calcite (Fig. 9A).

Several surface and sub-surface quartz veins at the Utanobori deposit were reported by MITI (1996) based on data from Sumitomo Metal Mining Co., Ltd. The vein map in Figure 9B includes veins identified on the surface, at 40 meter level (mL), 60 mL, 100 mL, and 160 mL, with respect to present-day sea level. The generalized strike and dip of the mineralized veins at Utanobori deposit are between N50ºE and N90ºE (mode: N60º-70ºE), and 70ºN and 90º, respectively, correlating well with ENE-WSW local structures (MITI, 1996). The NW-SE striking veins were reported to correspond with several fractures found in outcrops in the Utanobori area (MITI, 1996). The width of the veins commonly ranges from >5 cm to 30 cm, up to 1 m (MITI, 1996). Length of each vein ranges from 10 m to <220 m (Fig. 9B).

2.3. Samples and analytical methods

2.3.1. Sample type and quartz morphology

Float and outcrop samples analyzed in this study include mineralized and barren quartz veins from the southeastern extension of the No. 2 Kousaku Vein (n=8) and No. 6 Vein (n=2), silica sinters with (n=2) or without (n=2) cross-cutting quartz veins at the eastern extension of the No. 2 Kousaku Vein and Kousaku Vein, and southeast of No. 8 Vein and Kousaku Vein, respectively, kaolinite ± pyrite altered rocks (n=8), host rock tuff of the Esashi Formation (n=1), sedimentary host rock of the Esashi Formation analyzed for alteration mineralogy by XRD (n=20), Kinkomanai Lava

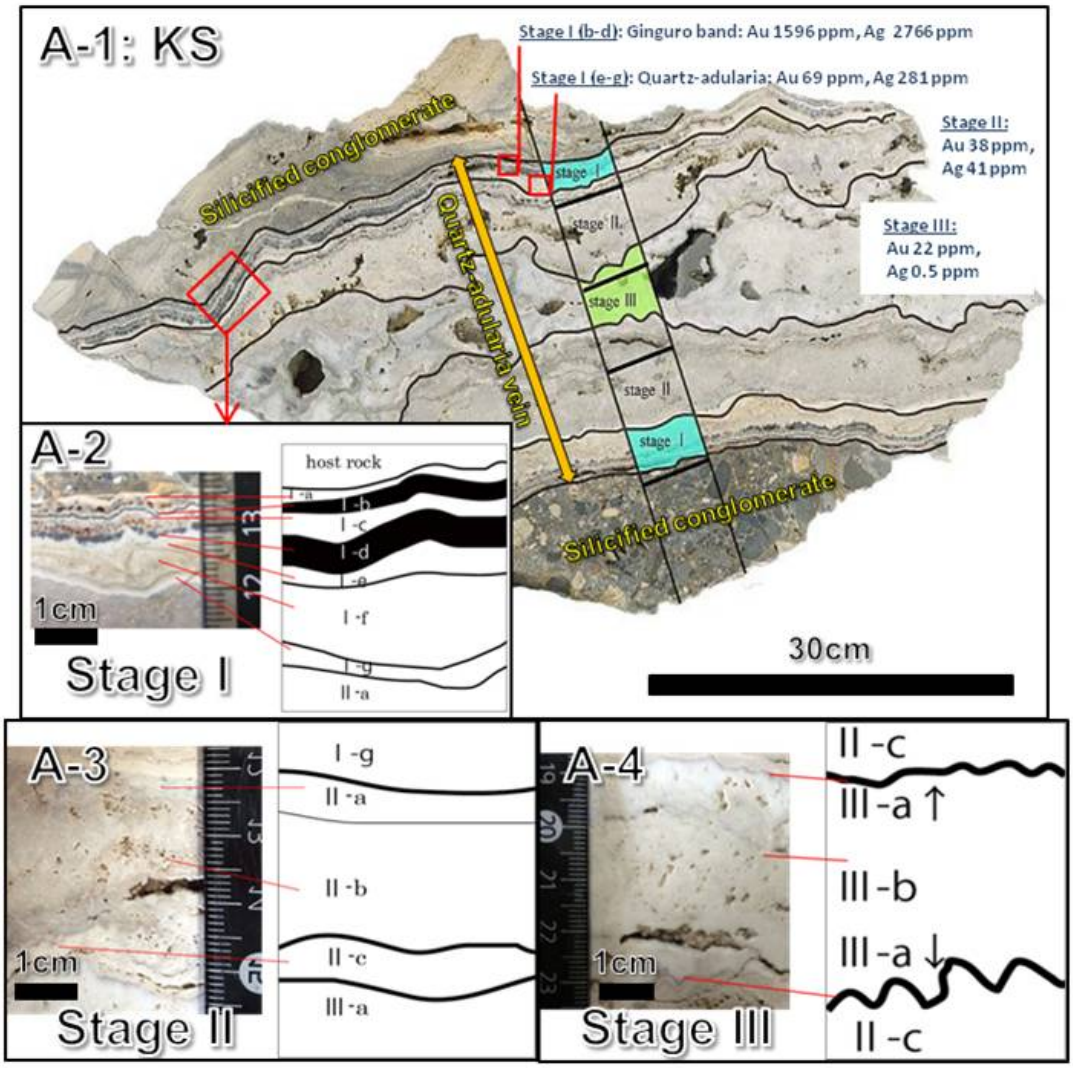

Fig. 10 Quartz-adularia vein with ginguro bands (Type 1 Vein) sample KS150708-01 (Sorulen *et al.*, 2019). (A-1) Host rock silicified conglomerate cut by Type 1 Vein exhibiting three stages of quartz growth. (A-2) Stage I, (A-3) stage II, and (A-4) stage III of the Type 1 Vein.

(n=2), and a 30 cm gold mineralized quartz-adularia vein showing three distinct stages of quartz generations with unknown sample locality (Figs. 9, 10). A total of five mine adits were visited, numbering 1 to 5 from east to west (Fig. 9B).

The classification of quartz textures in epithermal vein systems was first described by Adams (1920). Recent studies have noted that quartz textures in

epithermal gold vein deposits provide clues to understand the processes responsible for mineralization (e.g., Saunders, 1994; Dong *et al*., 1995). The classification of quartz textures in this study is adapted from Dong *et al.* (1995). "Vug" or "vuggy" terminology used in this study describes open cavities commonly associated with comb quartz.

In this study, the term "structure" and "textures" is used for features seen in hand specimen and under microscopic observation, respectively. Structures commonly observed in this study include colloform, crustiform, comb, and vuggy, with seven observed textures including mosaic, colloform, comb, zoned, feathery, flamboyant, ghost-sphere and pseudo-acicular quartz.

2.3.1.1 Quartz veins and silica sinter

Representative samples collected in this study are presented in Appendix 1 with sample photos in Figures 10 and 11. Stages for quartz veins and silica sinters were determined on hand specimen and further divided into sub-stages based on hand specimen and microscopic observation.

The quartz-adularia veins observed in this study either contain ginguro band or without, described as Type 1 Vein and Type 2 Vein, respectively. Both veins types were observed together at old mine adits or as isolated scattered floats. In hand specimen, three stages are identified in the Type 1 quartz veins having abundant adularia and black-colored silver-rich bands ("ginguro band") in the stage I and discontinuous ore mineral bands in the stage II, or may contain significant amount of adularia and <1 mm discontinuous ginguro bands in stage I. On the other hand one to two stages are recognized in the Type 2 quartz veining, commonly milky white to

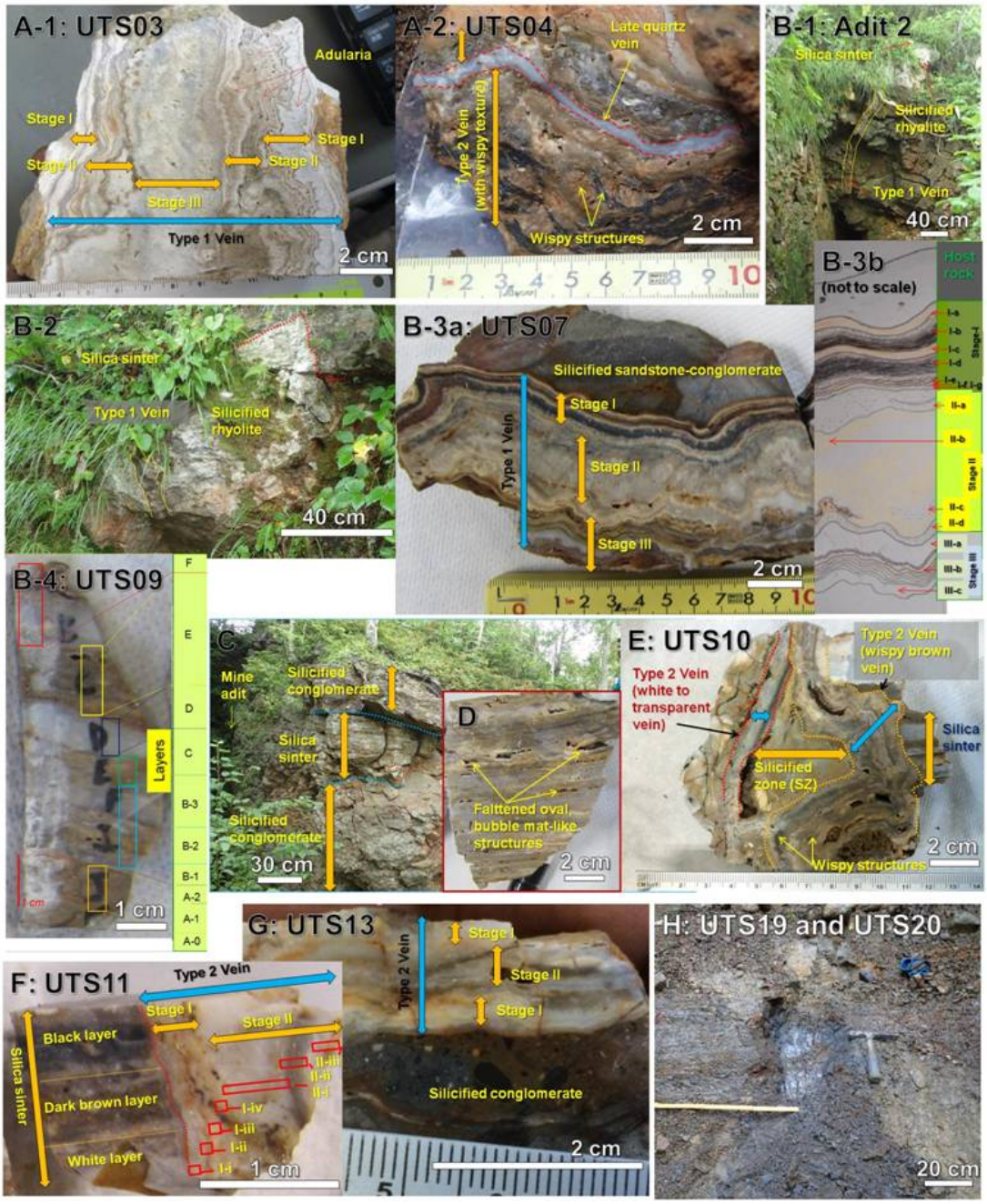

Fig. 11 Representative photos of the quartz veins, silica sinters, and altered rocks. (A-1) The Type 1 Vein with three stages of quartz veining (sample UTS03). (A-2) The Type 2 Vein exhibiting vuggy texture and discontinuous black sulfide bands with wispy structures (sample UTS04). (B-1) Type 1 Vein cutting silicified rhyolite overlain by silica sinter observed (outcrop at Adit 2). (B-2) Close up view of photo B-1 showing silicified rhyolite buried by silica sinter and later cut by the Type 1 Vein. (B-3a) Type 1 Vein with distinct ginguro bands (sample UTS07). (B-3b)

(Fig. 11 continued)

Representative sketch of the Type 1 Vein (sample UTS07). (B-4) Silica sinter sample 5 m east from B-2, showing silica sinter layers separated into layers A to F (sample UTS09). (C) Silica sinter intercalated between silicified conglomerates (outcrop). (D) Example of flattened ovals forming bubble mat-like structures in silica sinter. (E) Silica sinter conduit filled by post silicification, and later cut by early Type 2 Vein and late Type 2 Vein exhibiting wispy structures (sample UTS10). (F) Silica sinter cut by the Type 2 Vein, with silica sinter layers separated into black layer, dark brown layer, and white layer (sample UTS11). (G) The Type 2 Vein cutting silicified conglomerate at Adit 4 (sample UTS13). (H) Argillic clay ± pyrite in altered conglomerate (UTS19) and intercalated tuff layers (UTS20) of the Esashi Formation 2 km northwest from the mine.

transparent, or may exhibit wispy structure with minor to trace adularia content and no observable ginguro bands and was observed to cut the silica sinter. No cross-cutting relationship was observed between Type 1 Vein and Type 2 Vein. The Type 2 Veins cross cut the silica sinter.

Quartz and quartz + carbonate veins and stringers are treated independently regardless of the two veins earlier described. The former with a milky appearance with no observable adularia in hand specimen cuts Type 1 and Type 2 Vein. It also cross-cut the silica sinter.

Silica sinter is one of a common feature on the surface of hydrothermal systems, formed by precipitation of amorphous silica in geothermal areas. In this study, silica sinter observed consists of consecutive layers of milky white to transparent and red-orange-brown layers of quartz (which crystallized from initial

amorphous silica), commonly having compact, irregular, flattened oval or oval bubble mat-like structures (e.g., Lynne, 2013). The darker layers are commonly cut by veinlets and stringers of milky white to transparent quartz.

Three stages of crustiform-colloform quartz-adularia bands initially identified by MITI (1996) are identified in the Type 1 Vein (Fig. 10), which are further sub-divided into 12 to 14 sub-stages in this study based on hand specimen and microscopic observation. Stage I, II and III consist of 7, 3 and 2 bands respectively, with ginguro bands formed in the stage I-b and the stage I-d bands (Fig. 10A-1, A-2). A discontinuous ginguro band was formed in the stage II-a band. Stage III band is generally vuggy and contains brecciated host rock fragments. Adularia content decreases from stage I to III.

A Type 1 Vein observed at the Adit 1 ranges from 5 to 40 cm in thickness, exhibiting symmetrical crustiform-colloform structures of quartz-adularia bandings (Fig. 9B; sample UTS01 to UTS05), with adularia commonly formed in the stage I and II. The milky to transparent quartz vein contained embedded brecciated host rock fragments of silicified sandstone-siltstone of the Esashi Formation in the vein formed in the stage III of the Type 1 Vein of a sample UTS01, and vuggy quartz structure with minor adularia formed in stage III of UTS03 (Fig. 10A-1). A 3 mm quartz vein was formed and cut stages I and II bands of the Type 1 Vein (sample UTS02). The vein with wispy structure observed at the Adit 1 exhibits structures of vuggy and discontinuous black fine pyrite bands (Figs. 9B, 11A-2; sample UTS04, UTS05) cut by a late 5 mm wide colloform milky white to transparent quartz vein, observed to fill vugs (Fig. 11A-2).

A Type 1 Vein and silica sinter were observed at the Adit 2 (Figs. 9B, 11B). Three stages of quartz growth are identified in the Type 1 Veins in sample UTS06 to

UTS09. The veins range from 7 to 10 cm in width, with symmetrical structures of crustiform and colloform bands. Ginguro bands associated with red to brown iron oxide are observed to be separated by thin white to pinkish adularia bands that were formed in the stage I. Milky white to transparent quartz associated with white and pink adularia and fine black ore minerals were deposited in the stage II (sample UTS06, UTS07; Fig. 11B-3). Colloform quartz with minor adularia bands bounded by milky white to transparent quartz was deposited in stage III (sample UTS06 to UTS09; Fig. 11B-3). From the three stages observed in the Type 1 Vein of a sample UTS07 (Fig. 11B-3a), 14 sub-stages were identified by hand specimen and microscopic observations (Fig. 11B-3b). The Type 1 Veins continues upward toward the overlying silicified rhyolite and east-west trending silica sinter and is observed to cross cut the silicified rhyolite (sample UTS08; UTS09; Fig. 11B-1, B-2, B-4).

A silica sinter was observed hosted in silicified rhyolite (Fig. 11B-2, sample UTS08) and siltstone of the Esashi Formation at Adit 2 (Fig. 11B-4; sample UTS09). The silica sinters display consecutive layering consisting of milky white and orange to reddish-brown near horizontal layers ranging from 1 cm to 3 cm per layer with a total thickness of 30 cm. At a northward continuation of the Adit 3, a silica sinter is intercalated with silicified conglomerates of the Esashi Formation (Fig. 11C), and is also present approximately 20 m east of the Adit 3 (Fig. 9B; sample UTS12). Each layer ranges from <1 to 5 cm in thickness, commonly with flattened ovals of vugs in darker layers, with some layers about 1 mm in thickness (Fig. 11D).

A Type 2 Vein observed proximal to the Adit 4 shows two stages of banding with symmetrical growth structure of crustiform-colloform milky white to transparent quartz, exhibiting vuggy structure in the stage II band of the transparent quartz (sample UTS13; Figs. 9B, 11G).

A Type 1 Vein at the Adit 5 displayed 6 bands of crustiform-colloform structures mainly composed of quartz and adularia, with two ginguro bands in the band 1 and band 4 ranging from 1 mm to 1 cm wide, respectively (Fig. 9B; sample UTS14). Host rocks around the Adit 5 commonly consist of silicified conglomerate and siltstone of the Esashi Formation.

Approximately 50 m south of No. 8 Vein, a silica sinter was observed to be cut by a conduit-like structure, a vertical 9 cm wide open-space, filled later by non-crystalline silica which was later crystallized to microcrystalline quartz exhibiting vuggy structure. The conduit was cut by an early 1 cm wide white to transparent Type 2 Vein displaying a 2 mm thick black lining, which was cut by a later 2 cm wide Type 2 Vein with wispy structure exhibiting crustiform-colloform quartz with discontinuous black bands and vuggy structures (sample UTS10; Fig. 11E). The vein sample UTS11 displays symmetrical growth structures with two stages of quartz growth observed to cut the silica sinter (Fig. 11F).

In addition, a silica sinter sample from an unknown location in Utanobori was obtained from the Hokkaido University Museum.

2.3.1.2 Kinkomanai Lava and altered rocks of the Esashi Formation

Kinkomanai Lava blanketing the Hidaka Supergroup and the Esashi Formation crops out at approximately 4 km ESE of the mine (Fig. 9B; sample UTS15, UTS16). On hand specimen, the Kinkomanai Lava consists of 1 mm long white altered plagioclase and hornblende phenocrysts, and grey to purplish-grey groundmass with up to 1 cm irregular vugs filled at places with transparent amorphous silica (Fig. 9B).

Lapilli tuff of the Esashi Formation in sample UTS17 (Fig. 9B) chiefly consists of 1 cm yellowish to white altered plagioclase set in a moderately compact white altered matrix in hand specimen.

Clasts of conglomerate of the Esashi Formation were altered to clays proximal to the delineated silicified zone by MITI (1996) (sample UTS18; Fig. 9B). At approximately 2 km northwest from the mine, fine-grained cubic pyrites are disseminated in inter-beds of conglomerate and tuff (sample UTS19; Figs. 9B, 11H).

2.4 Analytical methods

Thin sections of representative quartz veins and silica sinters were prepared and petrographic analysis for mineral identification was carried out using a Nikon ECLIPSE LV100N polarizing microscope at Akita University, Japan. Alteration mineralogy on altered host rocks (n=20) was identified on the basis of X-ray diffraction (XRD) method. Altered host rocks were lightly crushed using an iron motar and pulverized in an agate motar to silt size, and measured at conditions of 30 kV and 16 mA, with scan speed at 2°/min for bulk analysis and 1°/min for the hydraulic elutriated clay minerals, from 2 to 60° and from 2 to 40°, respectively using a XRD Multiflex from Rigaku Corp. installed at Akita University in Japan. Hydraulic elutriated samples were treated with HCl to distinguish between kaolinite and chlorite. For bulk analysis, quartz sand was used as a standard.

For bulk chemical analyses, thirty-five representative samples of quartz veins, silica sinters, and altered host rocks were lightly crushed using an iron motar and pulverized in an agate motar to silt size. Powdered sampled were analyzed using an inductively coupled plasma mass spectrometer (ICP-MS) Agilent 7500 Series Agilent Technology ICP-MS by an acid digestion by HF, $HClO_4$ for Ag, Mn, Cu, Zn, Rb, Sr,

Sb, Te, Ba and Pb, and aqua regia for Au. Atomic absorption spectroscopy (AAS) was conducted using an Agilent 240FS Agilent Technology AAS on a sample (UTS07) to correct for silver content. Reference standards from GSJ were used in ICP-MS and AAS analyses. The analyses were conducted at Akita University, Japan.

Semi-quantitative analysis of chemical composition of minerals was conducted and their internal structures were examined using a JEOL JSM-6610 LV scanning electron microscope (SEM) with an Oxford energy dispersive spectroscope (EDS) and a Gatan Mini cathodoluminescence (CL) detector, respectively, at Akita University, Japan. Measurement conditions are at 15 kV acceleration voltage, 2.2 nA probe current and 10 mm working distance. Electrum composition was determined by a JEOL JXA-8800R SuperProbe electron probe micro-analyzer (EPMA) with wavelength dispersion spectroscopy, with acceleration voltage at 20 kV and a working distance of 10 mm with ZAF correction. The Au and Ag contents of electrum from stages I and II band of the Type 1 Vein on a total of 30 and 5 analytical points, respectively were determined. For the quantitative determination of Al, K, Ti, Fe, Mn and Si contents of quartz, measurement conditions of the EPMA were set at 20 kV acceleration voltage, 80 nA beam current with a beam diameter of 5 μm, and counting time of 15 sec and 300 sec for Si and Al, Ti, K, Mn, and Fe, respectively. Detection limits of Al, K, Ti, Fe, Mn, and Si are 13, 10, 23, 21, 20 and 46 ppm, respectively, with analytical error range of ±3 %. The analysis was conducted at Akita University, Japan.

For sulfur isotope analysis, mineral separates of pyrite from two argillic altered samples were prepared. Pyrite was decomposed by adding nitric acid and bromine and was finally converted to $BaSO_4$, from which SO_2 gas was obtained for measurement of isotope of sulfur using a Thermo Delta-V Advantage, isotope ratio

mass spectrometer at Akita University, Japan. The isotopic ratio is presented in $\delta^{34}S$ (‰) expression relative to Canyon Diablo Troilite (CDT).

Age dating was conducted on three separated adularia fractions representative of stages I, II and III of the Type 1 Vein obtained from a 30 cm gold mineralized float (Fig. 10). Mineral separates of adularia were sent to Actlabs in Canada for ^{40}Ar-^{39}Ar geochronology using an incremental step heating method using CO_2 laser. Plateau age determination and data correction were conducted using the computer software Isoplot v4.15 (Ludwig, 2012). Adularia separated from silica sinter and a glassy rhyolite (for whole-rock) of the Esashi Formation were sent to the Institute of Geological and Nuclear Sciences Limited in New Zealand for K-Ar age determination (Sorulen *et al*,. 2019).

2.5. Results

2.5.1. Alteration, mineralization and textural characteristics

This section presents results on alteration assemblages of the altered host rocks of the Esashi Formation (Fig. 9A) and ore and gangue mineral assemblages and textural characteristics of the quartz-adularia veins (Figs. 12, 13) and silica sinter (Fig. 14). Paragenetic sequences of the quartz-adularia veins (Type 1 and Type 2 Veins) and silica sinter are shown in Figure 15.

2.5.1.1 Altered host rocks

Alteration mineralogy of representative samples of altered conglomerate, sandstone, siltstone and mudstone of the Esashi Formation was determined by XRD analysis (Table 3). Sample localities are shown in Figure 9A. Alteration mineral assemblages consist of (I) quartz + K-feldspar ± chlorite/smectite mixed layer that coincides with

the silicified zone, (II) quartz + K-feldspar + illite ± smectite, in and proximal to the silicified zone, (III) quartz + chlorite/smectite mixed layer ± calcite distal to the silicified zone, and (IV) quartz + kaolinite ± illite ± smectite proximal to distal areas

Table 3 Alteration mineralogy determined from XRD analysis of altered host rocks (Suzuki, 2015 MS). Alteration ID is represented in Figure 9A.

Sample location	Sample type	Qtz	Plag	K-feldspar	Smec	Ill	Kao	C/S	Cal
a	Conglomerate	++++		-					
b	Sandstone	++++		-	-	-			
c	Conglomerate	+++		-				-	
d	Mudstone	++++		-					
e	Mudstone	++++		-					
f	Conglomerate	++++		-	-	-			
g	Conglomerate	++++		-	-	-			
h	Conglomerate	++++		-	-	-			
i	Conglomerate	++++		-	-	-			
j	Sandstone	++++		-		-			
k	Conglomerate	+	-					+	+
l	Mudstone	+++	-			-		-	
m	Mudstone	++++				-	-		
n	Sandstone	+++			+	-	-		
o	Conglomerate	++++		-		-			
p	Mudstone	++++				-	-		
q	Sandstone	++++				-	-		
r	Sandstone	++++				-	-		
s	Sandstone	++++		-					
t	Conglomerate	+++		-		-			

Abundance respective to quartz standard: ++++: => 20%, +++: 15-20%, ++: 10-15%, +: 5-10%, -: <5%. Abbreviations: Qtz = quartz; Plag = plagioclase; K-feld = K-feldspar; Smec = smectite; Ill = illite; Kao = kaolinite; C/S = chlorite/smectite mixed layer; Cal = calcite.

with respect to the silicified zone (Fig. 9A). The distribution of these alteration assemblages are not strictly restricted but may occur as discontinuous or spots in the silicified zone (alteration assemblage II and IV). Alteration IV assemblage was observed at the rim of the silicified zone and at lower elevation with respect to the silicified zone (Fig. 9A).

2.5.1.2 Quartz-adularia veins

Gold mineralization at the Utanobori deposit is divided into three stages consisting of 12 to 14 bands observed in the quartz-adularia veins with ginguro (Type 1 Veins) (Figs. 10, 11B-3, 15A).

In the stage I of the Type 1 Vein, electrum, naumannite and an unidentified Fe-Sb oxide formed in the bands I-b and I-d of stage I (Fig. 15A). Trace pyrite, silver halides [chlorargyrite (AgCl) and bromargyrite (AgBr)], chalcopyrite, sphalerite, barite, and unidentified Fe-(Sb)-As oxide formed variably in the stage I (Fig. 15A). Electrum and naumannite commonly <10 μm across were formed in the bands I-a. I-c, I-f, and I-g of the stage I, and commonly >10 to >20 μm across formed in the I-b and I-d bands of the stage I (Figs. 12A-2, A-3). Electrum and naumannite in the bands I-b and I-d show distinct dendritic texture (e.g., Saunders *et al.*, 1996), with growth orientations facing towards the vein center, and commonly distorted by comb (zoned) texture (Figs. 12A; 15A). Mosaic and microcrystalline quartz exhibiting colloform texture commonly formed in the stage I band of the Type 1 Vein, with zoned and comb texture common also in the bands I-b and I-d, respectively (Fig. 15A). In the stage I band of the Type 1 Vein, microcrystalline quartz exhibiting colloform (ghost-sphere) texture was recrystallized to mosaic quartz, with an exception observed for the band I-c (e.g., Figs. 12B; 15A). Comb (zoned) quartz was formed proximal to mosaic or microcrystalline quartz (e.g., Fig. 12B). In the band I-b, feathery quartz was observed along the growth tips of early formed comb-zoned quartz (e.g., Fig. 12B). Ore minerals are closely associated with microcrystalline quartz and scarcely with adularia in the stage I bands (Figs. 12A, 15A). Comb (zoned) quartz was observed to enclose ore minerals during its growth (e.g., Fig. 12C). Microcrystalline quartz formed in the stage I band exhibiting colloform (ghost-sphere) texture commonly

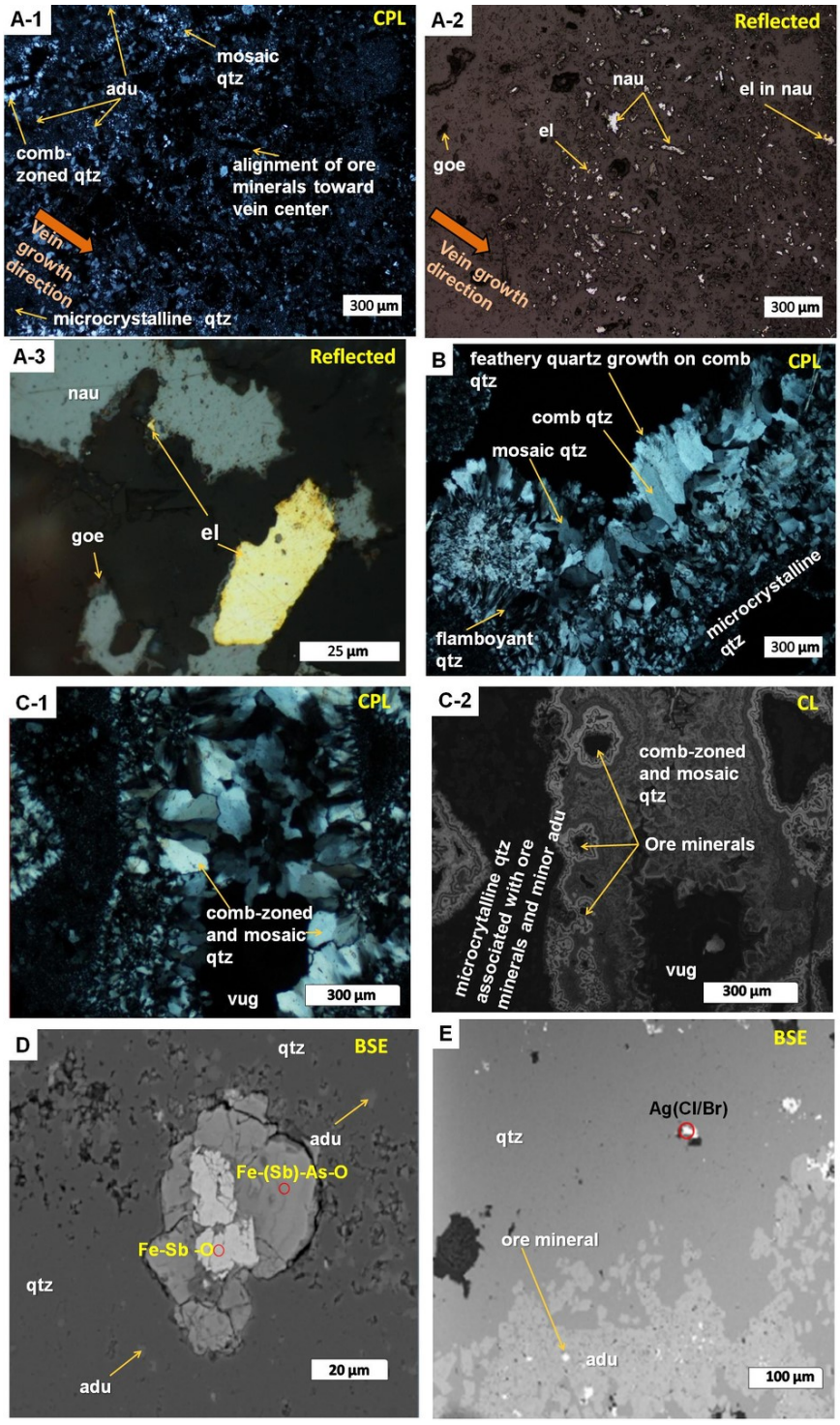

Fig. 12 Representative photomicrographs of the Type 1 Vein. (A-1) Quartz textures, with microcrystalline quartz, comb-zoned, and mosaic textures and adularia in stage I band (band I-b) in the Type 1 Vein showing the growth direction and alignment of dendritic ore minerals associated with microcrystalline-colloform banded quartz (sample UTS07). (A-2) Association of electrum and naumannite with

(Fig. 12 continued)

banded quartz (sample UTS07). (A-3) Close up photomicrophotograph of electrum and naumannite (sample UTS07). (B) Common types of quartz textures observed in the Type 1 Vein. (C-1) Stage I band, sub-stage I-b band of the Type 1 Vein, showing microcrystalline, comb-zoned and mosaic quartz in crossed-polarized light (CPL) (sample UTS07). (C-2) CL image of photomicrograph C-1 (sample UTS07). (D) Fe-(Sb)-As oxide (Spectrum 1) and Fe-Sb oxide (Spectrum 2) in the band III-b of the Type 1 Vein (sample UTS07). (E) Silver halides [Ag(Cl/Br)] in the band I-b of the Type 1 Vein (spectrum 1) (sample UTS07).

associate with ore minerals. The Fe-Sb oxide was commonly associated with Fe-(Sb)-As oxide formed in the stage I (e.g., Fig. 12D; Fig. 15A), and minor chlorargyrite and bromargyrite formed in the bands I-b and I-d, and trace in the bands I-a, I-c, I-e, I-f, I-g of the stage I (e.g., Fig. 12E, Spectrum 1 - Cl: 7.7 wt. %, Br: 20.3 wt. %, Ag: 58.5 wt. %; Fig. 15A). Secondary goethite after sulfides (commonly pyrite and chalcopyrite) is present in the bands I-b and I-d, and minor in the bands I-a, I-c, I-e, I-f, I-g (Fig. 12A-3; Fig. 15A). Minor illite and trace smectite are present in the band I-a proximal to the host rock siltstone (Fig. 15A).

In the Type 1 Vein, electrum commonly formed with minor naumannite and Fe-Sb oxide in the band II-a of the stage II (Fig. 15A). Trace Fe-(Sb)-As oxide, chlorargyrite, and bromargyrite only formed in the band II-a of the stage II. Trace pyrite formed in the stage II (Fig. 15A). Electrum and naumannite formed in the stage II are commonly <10 μm across. In the stage II band of Type 1 Vein, similar textural changes of quartz were observed for microcrystalline quartz, mosaic and comb (zoned) quartz as described for the stage I band of Type 1 Vein, but with some ghost-

sphere quartz exhibiting flamboyant texture in the bands II-a and II-c of the stage II of the Type 1 Vein (Figs. 12B, 15A). The CL characteristics are also similar to those described for the microcrystalline quartz, mosaic, comb (zoned) and feathery quartz that formed in the stage I band of Type 1 Vein. The flamboyant quartz formed in the bands II-a and II-b displayed CL-dark, CL-intermediate, and CL-bright bandings. Brecciated colloform textures observed in the band II-b of the stage II band displayed CL-dark, CL-intermediate and CL-bright bandings. Ore minerals formed in the stage II are closely associated with microcrystalline quartz exhibiting colloform (ghost-sphere) texture and scarcely with adularia (Fig. 15A). In the band II-c, microcrystalline quartz exhibiting colloform (ghost-sphere) texture associated with trace pyrite, mosaic, and comb quartz commonly formed (Fig. 15A). Secondary goethite commonly formed in the stage II band (Fig. 15A).

In the Type 1 Veins during the stage III, trace electrum, naumannite, chlorargyrite, bromargyrite, pyrite, chalcopyrite, barite, Fe-Sb oxide and Fe-(Sb)-As oxide were formed in the band III-b associated with the thin bands of microcrystalline quartz exhibiting colloform-ghost-sphere textures (Fig. 15A). Naumannite, barite and Fe-Sb oxide, and pyrite, chalcopyrite, Fe-Sb and Fe-(Sb)-As oxides were formed as trace in the bands III-a and III-c, respectively of the stage III (Fig. 15A). Electrum and naumannite formed in the stage III in the Type 1 Veins are commonly <10 μm across. In the bands III-a and III-b, comb quartz were formed proximal to microcrystalline quartz, and proximal to mosaic quartz in the band III-c. The CL characteristics observed for microcrystalline quartz exhibiting colloform-ghost-sphere textures and comb quartz formed in the stage III band of Type 1 Vein are similar to the microcrystalline quartz and comb quartz formed in the stage I band of the Type 1

Vein. Secondary goethite commonly is present in the bands III-b, and minor in the bands III-a and III-c (Fig.15A).

The observed differences between the bands of the Type 1 Vein in samples KS and UTS07 are due to the occurrence of the bands II-c and III-b in sample UTS07, and absence of the bands II-c and III-b in the sample KS (Figs. 10; 11B-3; 15A).

The representative quartz-adularia vein without ginguro band (Type 2 Vein) that cross-cuts the silica sinter is divided into two stages consisting of 7 bands (Figs. 11F, 15B). In the Type 2 Vein (Fig. 11F), trace electrum was formed in the bands I-iii and I-iv, and together with trace naumannite in the band I-ii (Fig. 15B). The Fe-Sb oxide, Fe-(Sb)-As oxide and chalcopyrite (and pyrite) were formed variably in the stage I (Fig. 15B). The band I-i was observed to horizontally branch out as quartz stringers into the silica sinter layers (Fig. 13A-1). In the band I-i, ore minerals are associated with the thin (<150 μm across) early formed microcrystalline quartz band of the horizontal quartz stringers (Fig. 13A-1, A-2, A-3). In the stage I band of the Type 2 Vein, microcrystalline quartz exhibiting colloform (ghost-sphere, flamboyant) textures were recrystallize to mosaic quartz. Comb-zoned quartz formed proximal to mosaic or microcrystalline quartz, with late feathery texture were formed along the growth tips of the early formed comb-zoned quartz in the stage I band in the Type 2 Vein (Figs. 13B; 15B). Pyrite was enclosed by comb-zoned quartz formed in the band I-i. The CL of microcrystalline quartz, and comb-zoned and mosaic quartz commonly showed characteristics of CL-dark, and CL-dark, CL-intermediate and CL-bright bands, respectively (Fig. 13A-2). In the bands I-ii, I-iii and I-iv of stage I band of the Type 2 Vein (Fig. 15B), microcrystalline quartz exhibiting colloform (ghost-sphere) texture commonly showed CL-dark, and mosaic, comb-zoned, feathery, and flamboyant quartz commonly showed CL-dark, CL-intermediate, and CL-bright

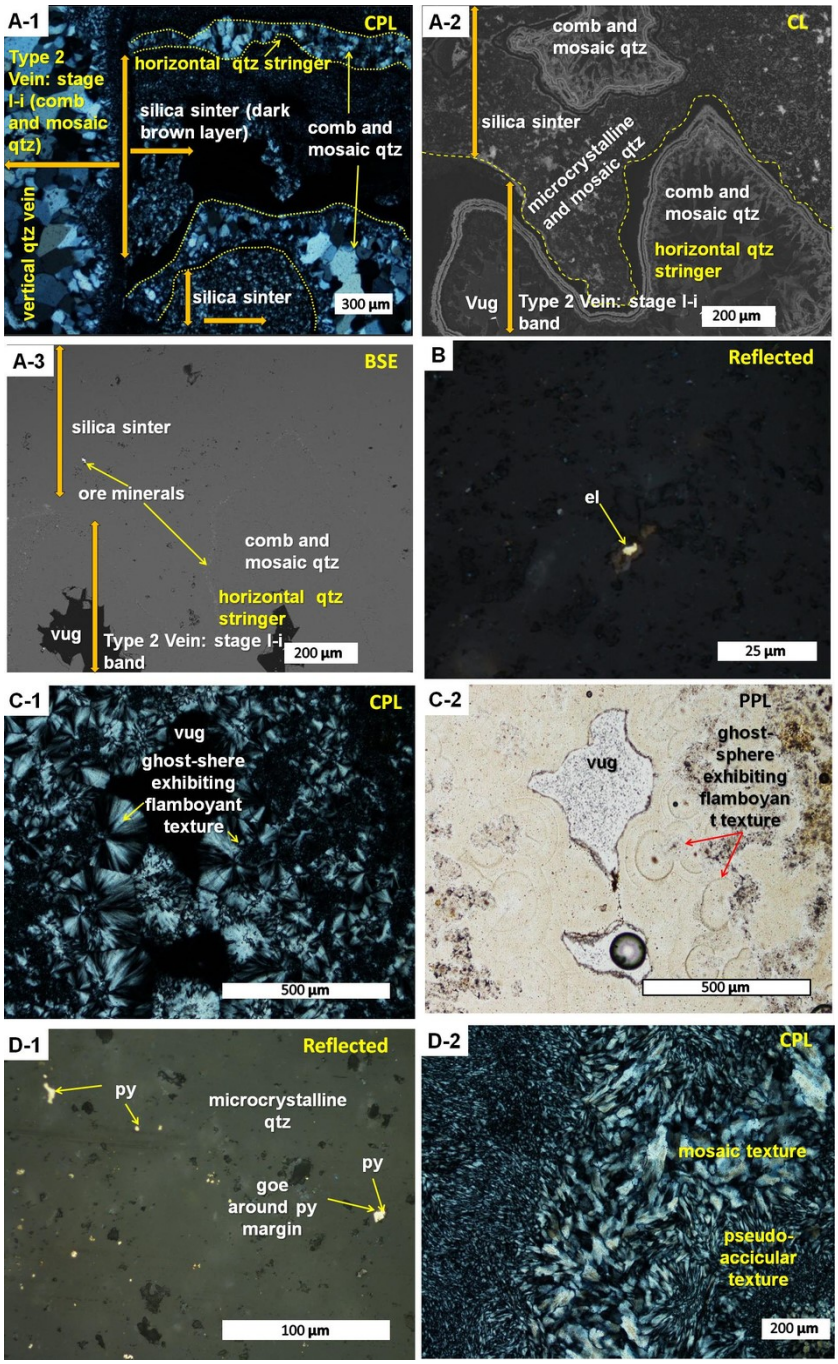

Fig. 13 Representative photomicrographs of the Type 2 Vein. (A-1) The Type 2 Vein cutting silica sinter in sample UTS11, showing vertical and horizontal cross cutting relationship of the stage I band (band I-i). (A-2) CL image of the stage I band (band I-i) horizontally extended into silica sinter (sample UTS11). (A-3) BSE image of photomicrograph A-2. (B) Occurrence of electrum in the band I-ii of the stage I band (sample UTS11).

(Fig. 13 continued)

(C-1) Stage III band of the wavy vein showing ghost-sphere exhibiting flamboyant texture in CPL (sample UTS10). (C-2) Ghost-sphere texture in plane-polarized light (PPL) (sample UTS10). (D-1) Wavy vein, showing disseminated fine-grained pyrite in the dark discontinuous band in reflected photomicrograph (sample UTS04). (D-2) Pseudo-acicular and mosaic textures in the late colloform quartz vein cutting the wavy vein (sample UTS04).

bands (e.g., Fig. 13A-2). Ore minerals are closely associated with microcrystalline quartz exhibiting colloform (ghost-sphere) textures, with electrum and naumannite commonly <5 μm across formed in the stage I (Fig. 13B; 15B). Secondary goethite is present variably throughout the stage I of the Type 2 Vein.

In the Type 2 Vein that cross-cuts the silica sinter (Figs. 11F, 15B), trace pyrite, chalcopyrite, Fe-Sb oxide and Fe-(Sb)-As oxide are present in the band II-ii, and electrum and naumannite (commonly <5 μm across) in the band II-iii, closely associated with microcrystalline quartz exhibiting colloform ghost-sphere textures (Fig. 15B). In the Type 2 Vein, similar textural changes and CL characteristics of quartz occurred for microcrystalline quartz exhibiting colloform ghost-sphere textures, mosaic, and comb-zoned quartz. Secondary goethite after sulfides is present in the band II-ii of the Type 2 Vein (Fig. 15B).

In the Type 2 Vein, trace electrum, naumannite and minor pyrite associated with microcrystalline quartz is present in the brown wispy vein that cross-cuts the white to transparent vein (Fig. 11E, sample UTS10). Ghost-sphere and flamboyant texture is common in the brown wispy vein (Fig. 13C). In the sample UTS04 (Fig. 11A-2), ore minerals associated with microcrystalline quartz are observed in the

discontinuous black bands exhibiting vuggy and wispy structures (brown wispy vein) and having dominant secondary goethite and fine-grained pyrite (Fig. 11A-2). Mosaic, microcrystalline, comb, colloform and pseudo-acicular textures commonly are present in the late cross-cutting quartz vein in UTS04 (Figs. 11A-2, 13D-2).

2.5.1.3 Silica sinter

In the silica sinter (Figs. 11B-4, 15C), the layering of milky white and brown layers are separated into 6 layers from A (base of silica sinter) to F (top of silica sinter) (Figs. 14, 15C). The layer A is characterized by the occurrence of near horizontal quartz alignment in a matrix of abundant microcrystalline quartz exhibiting trace ghost-sphere texture that crystallized from initially amorphous silica (Figs. 14A, 15C). The light brown layer A-0 is overlain by a brown layer A-1, which in turn is overlain by the light brown layer A-2 (Figs. 14A, 15C).

The layer B is characterized by a dominant milky white microcrystalline quartz layer that crystallized from initially amorphous silica. The milky white layer B-1 overlay the layer A-3 of the silica sinter (Figs. 11B-4, 15C). The layer B-1 is overlain by the layer B-2, characterized by discontinuous wispy micro-fractures stained by goethite-hematite, which in turn is overlain by a milky white layer B-3 (Fig. 15C).

The layer C is characterized by partly preserved, four stacked layers of palisade-like textures (<500 μm thick per layer) with microbial filaments (e.g., Lynne, 2013; Figs. 14A; 15C) that formed initially as amorphous silica. The layer C overlay the layer B-3 of the silica sinter (Figs. 11B-4; 15C).

The layer C is overlain by the layer D of the silica sinter (Figs. 11B-4; 15C). The layer D is characterized by a milky white microcrystalline quartz layer exhibiting

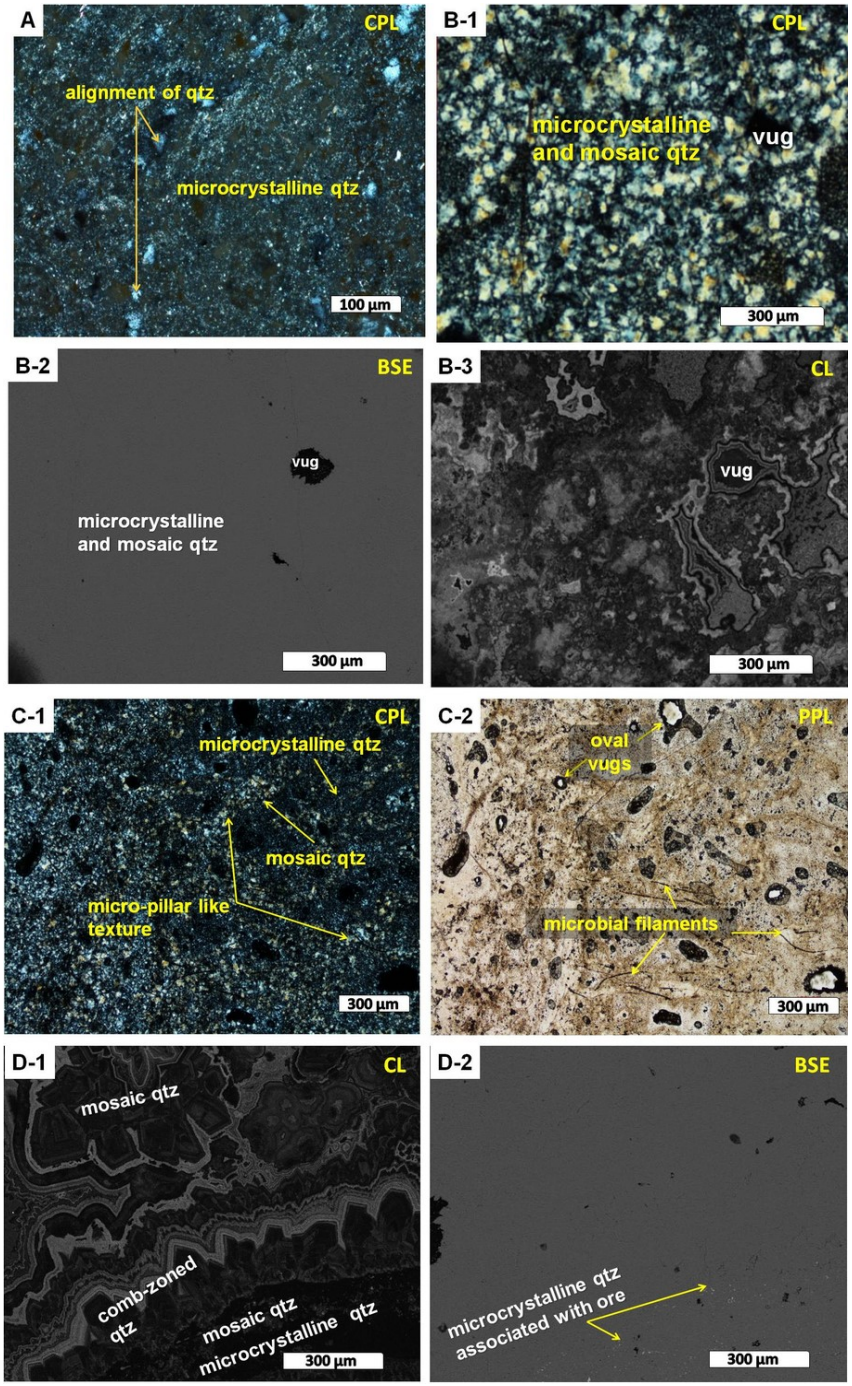

Fig. 14 Representative photomicrographs of the silica sinter. (A) Silica sinter showing dominant microcrystalline quartz and quartz alignment in the layer A-1 (bottom layer) (sample UTS09). (B-1) Silica sinter layer B-2 showing mosaic and microcrystalline quartz in CPL (sample UTS09). (B-2) BSE image of photomicrograph B-1 showing the absence of ore minerals (sample UTS11). (B-3) CL image of photomicrograph B-2 showing the CL characteristics of mosaic and microcrystalline quartz (sample

(Fig. 14 continued)

UTS11). (C-1) Palisade-like texture in layer C of the silica sinter showing micro-pillar structures in CPL (sample UTS11). (C-2). PPL view of photomicrophotograph C-1 showing microbial filaments (sample UTS11). (D-1) CL image of the quartz stringer in layer E of the silica sinter (sample UTS11). (D-2) BSE image of photomicrograph D-1 showing ore minerals associated with early microcrystalline quartz of the quartz stringer (sample UTS11).

trace ghost-sphere texture that crystallized from initially amorphous silica. The layer D exhibits black spots texture and micro-fractures stained by minor goethite-hematite.

The layer E overlay the layer D of the silica sinter. The layer D is characterized by a massive microcrystalline quartz layer that crystallized from initially amorphous silica.

The top layer F of the silica sinter show similar characteristics to layer E, but is partially vuggy (Figs. 11B-4, 15C).

Post hydrothermal activity after silica sinter deposition formed Fe-Sb oxide and Fe-(Sb)-As oxide in the layer A associated with discontinuous quartz stringers (Figs. 14A), and continuous quartz stringers in the layer B-1 (Fig. 15C). In the layers B to F, microcrystalline quartz exhibiting (colloform) trace ghost-sphere was recrystallized to mosaic quartz. In the layer B-1, trace comb (zoned) quartz of the horizontal quartz stringers were formed proximal to mosaic or microcrystalline quartz, with later feathery texture formed along the growth tips of the early comb (zoned) quartz. In the layer C, vugs associated with the palisade-texture were commonly filled by mosaic quartz and proximal comb quartz of the discontinuous horizontal quartz stringers (Figs. 15C, 14C). The horizontal quartz stringers in the

A

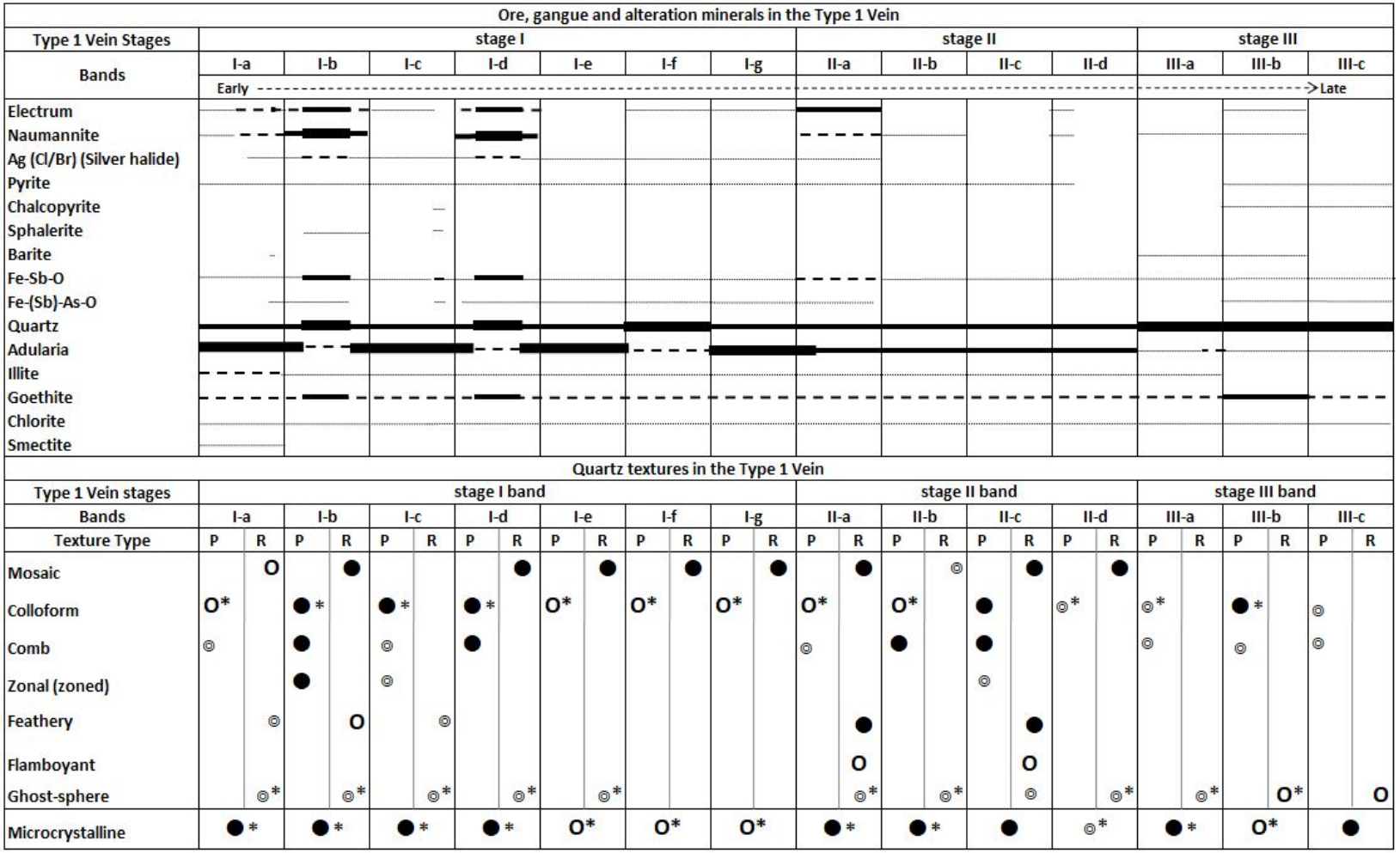
Ore, gangue and alteration minerals in the Type 1 Vein
Type 1 Vein Stages
stage I
stage II
stage III
Bands
I-a I-b I-c I-d I-e I-f I-g II-a II-b II-c II-d III-a III-b III-c
Early
Late
Electrum
Naumannite
Ag (Cl/Br) (Silver halide)
Pyrite
Chalcopyrite
Sphalerite
Barite
Fe-Sb-O
Fe-(Sb)-As-O
Quartz
Adularia
Illite
Goethite
Chlorite
Smectite
Quartz textures in the Type 1 Vein
Type 1 Vein stages
stage I band
stage II band
stage III band
Bands
I-a I-b I-c I-d I-e I-f I-g II-a II-b II-c II-d III-a III-b III-c
Texture Type
P R
Mosaic
Colloform
Comb
Zonal (zoned)
Feathery
Flamboyant
Ghost-sphere
Microcrystalline

B

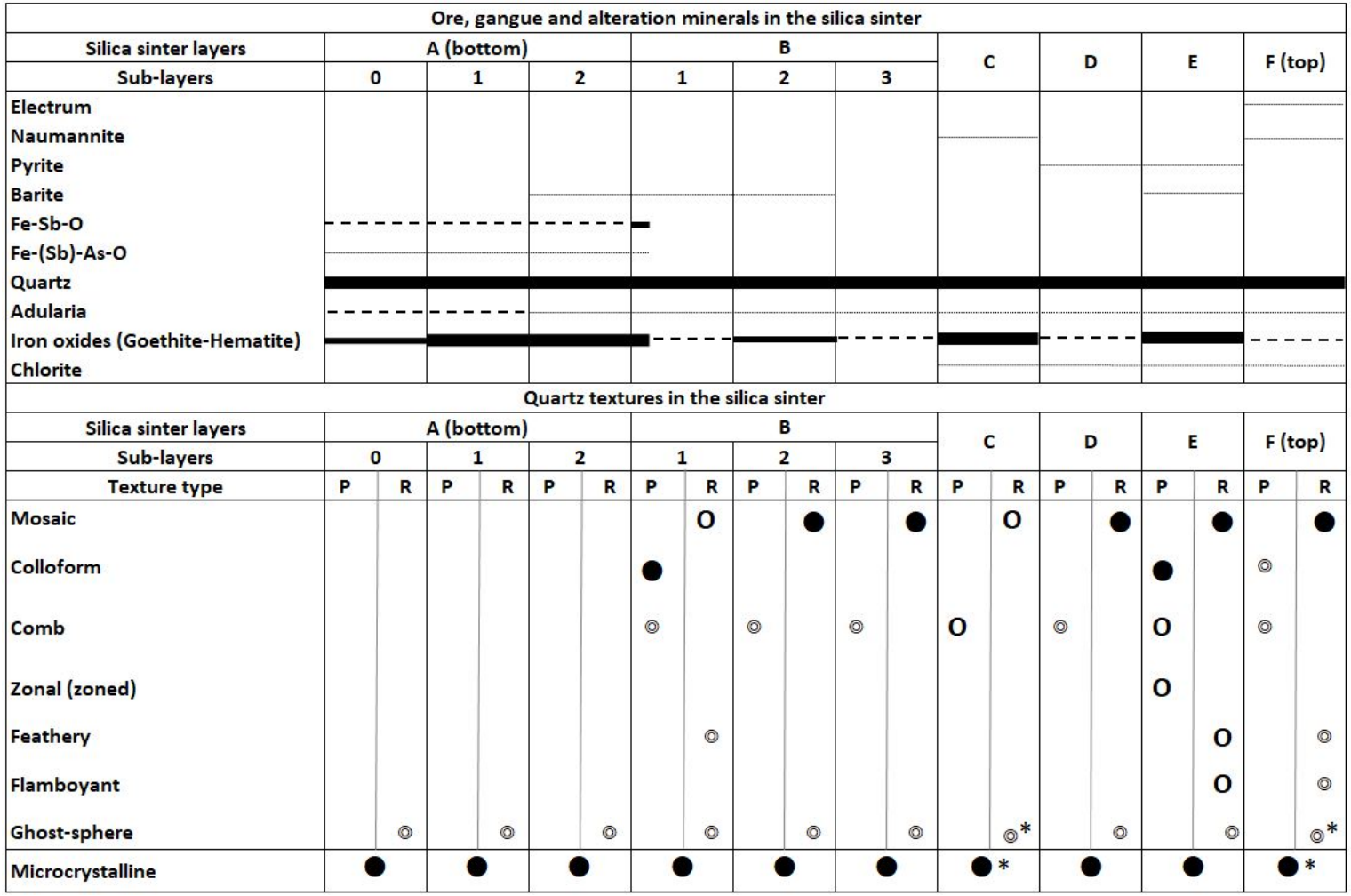
Ore, gangue and alteration minerals in the silica sinter
Silica sinter layers
A (bottom)
B
C
D
E
F (top)
Sub-layers
0
1
2
1
2
3
Electrum
Naumannite
Pyrite
Barite
Fe-Sb-O
Fe-(Sb)-As-O
Quartz
Adularia
Iron oxides (Goethite-Hematite)
Chlorite
Quartz textures in the silica sinter
Silica sinter layers
A (bottom)
B
C
D
E
F (top)
Sub-layers
0
1
2
1
2
3
Texture type
P
R
Mosaic
Colloform
Comb
Zonal (zoned)
Feathery
Flamboyant
Ghost-sphere
Microcrystalline

C

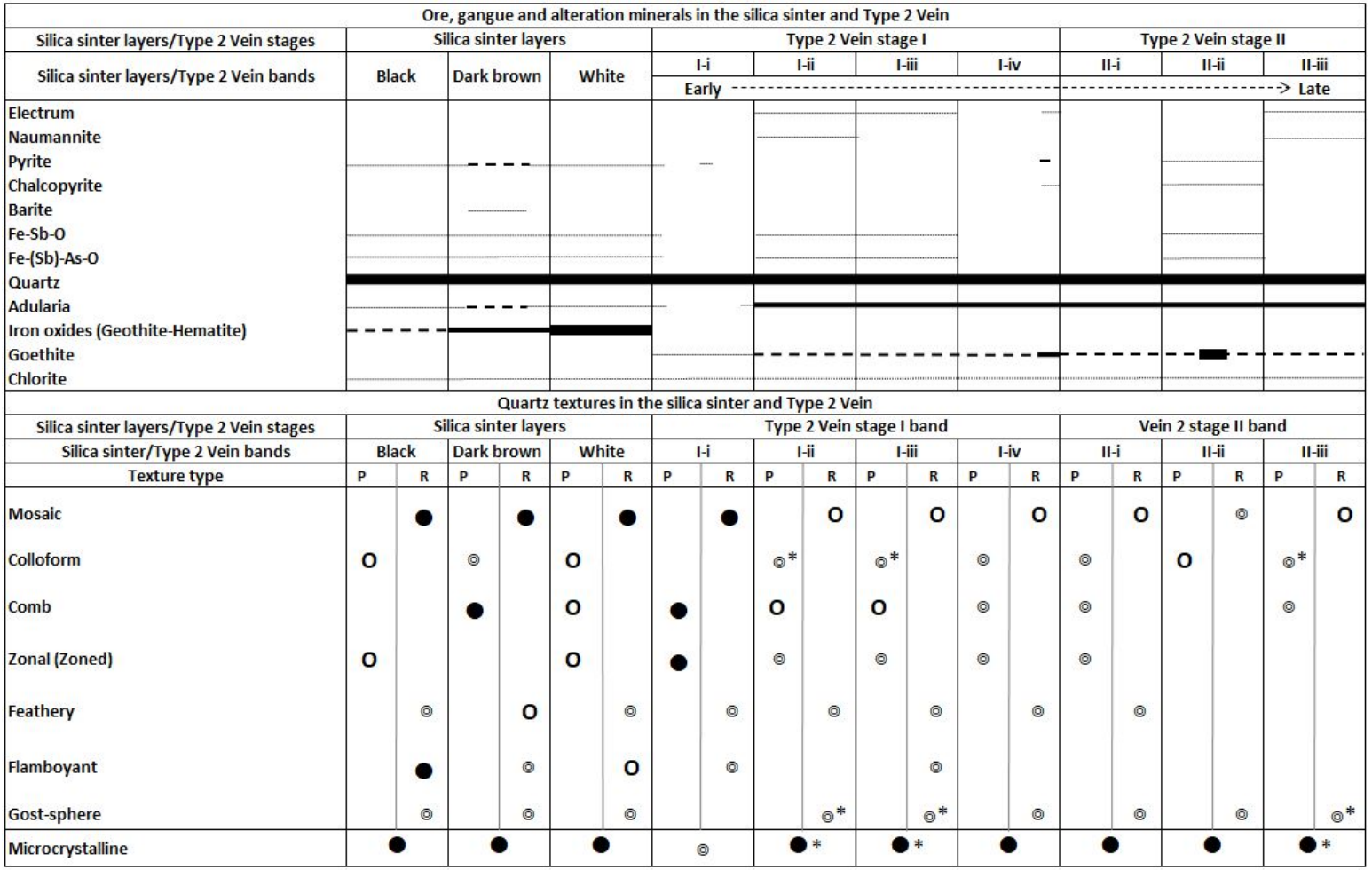
Ore, gangue and alteration minerals in the silica sinter and Type 2 Vein
Silica sinter layers/Type 2 Vein stages
Silica sinter layers
Type 2 Vein stage I
Type 2 Vein stage II
Silica sinter layers/Type 2 Vein bands
Black
Dark brown
White
I-i
I-ii
I-iii
I-iv
II-i
II-ii
II-iii
Early
Late
Electrum
Naumannite
Pyrite
Chalcopyrite
Barite
Fe-Sb-O
Fe-(Sb)-As-O
Quartz
Adularia
Iron oxides (Geothite-Hematite)
Goethite
Chlorite
Quartz textures in the silica sinter and Type 2 Vein
Silica sinter layers/Type 2 Vein stages
Silica sinter layers
Type 2 Vein stage I band
Vein 2 stage II band
Silica sinter/Type 2 Vein bands
Black
Dark brown
White
I-i
I-ii
I-iii
I-iv
II-i
II-ii
II-iii
Texture type
P
R
Mosaic
Colloform
Comb
Zonal (Zoned)
Feathery
Flamboyant
Gost-sphere
Microcrystalline

Alteration	Ore and gangue	Symbol
Extreme	Abundant	▬▬▬
Strong	Common	▬▬
Moderate	Minor	- - - - - -
Weak	Trace	.....

Minerals		Quartz
Textural symbols and abundances	Common	●
	Minor	O
	Trace	◎
*Associated with Au and Ag ore		

Fig. 15 Paragenetic sequences and quartz textures. (A) Type 1 Vein, (B) Type 2 Vein cross cutting the silica sinter, and (C) silica sinter. Abbreviations for quartz Textures; P = primary texture, R= recrystallization texture.

layer C compose of microcrystalline quartz associated with trace naumannite (<5 μm across), and comb quartz (Fig. 15C). In the layer D, trace pyrite is associated with microcrystalline quartz of the horizontal quartz stringers. In the layer E, trace pyrite are associated with abundant quartz stringers (Figs. 11B-4, 14D, 15C). Trace pyrite is associated with the colloform microcrystalline quartz of the quartz stringer in the layer E. The layer F is similar to the layer E, except for the decrease abundance of quartz stringers, a decrease in goethite-hematite alteration, the absence of comb-zoned texture, and the presence of trace electrum and naumannite associated with microcrystalline quartz of the horizontal quartz stringers in the layer F (Figs. 11B-4, 15C). In the layers A to F, microcrystalline quartz exhibiting colloform (ghost-sphere) texture commonly display CL-dark. Flamboyant, mosaic, comb-zoned, and feathery quartz display CL-dark, CL-intermediate and CL-bright bands (Fig. 14B-3, D-1).

In the sample UTS11 (Figs. 11F, 15B), silica sinter was separated into black, dark brown and white layers based on color and the occurrence of goethite-hematite and adularia content. The vertical orientation and stages of layering of the silica sinter float sample is unknown. Pyrite, Fe-Sb and Fe-(Sb)-As oxides are associated with colloform microcrystalline quartz of the horizontal quartz stringers (Figs. 13A, 15B).

2.5.2 Ar-Ar and K-Ar age dating

^{40}Ar-^{39}Ar dating on adularia in stages I, II and III bands of the quartz-adularia vein with ginguro band (Type 1 Vein) in sample KS150708-01 was conducted (Fig. 10). The results of the ^{40}Ar-^{39}Ar step heating method show plateau weighted ages for stages I, II and III at 13.63±0.06 Ma (2σ) (MSWD = 4.4) with 100 % $^{39}Ar_k$ released, 13.63±0.07 Ma (2σ) (MSWD = 1.5) with 58.7 % $^{39}Ar_k$ released, and 13.63±0.06 Ma (2σ) (MSWD = 4.0) with 65.2 % $^{39}Ar_k$ released, respectively (Fig. 16).

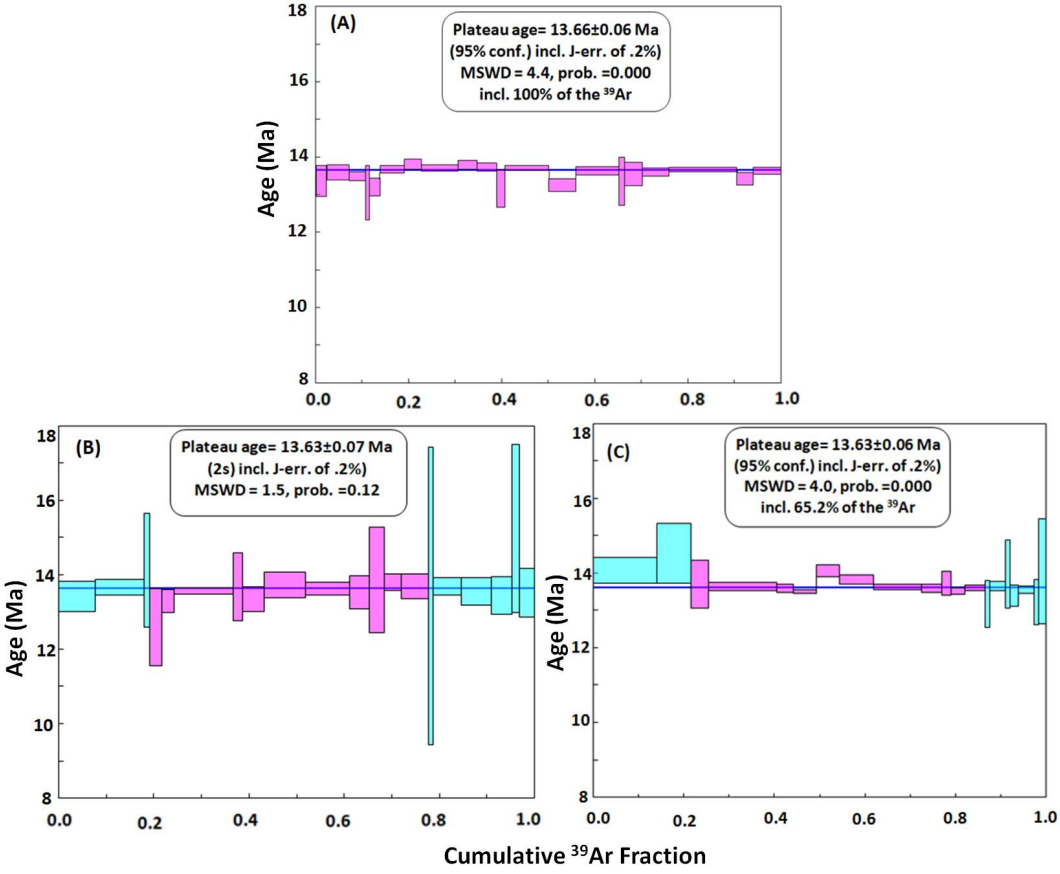

Fig. 16 ^{39}Ar-^{40}Ar ages of adularia from sample KS150708-01 (Fig. 10, Type 1 Vein) for (A) the stage I of the Type I Vein, (B) the stage II of the Type 1 Vein, (C) and stage III of the Type 1 Vein. Plateau steps are magenta, rejected steps are cyan.

K-Ar method age dating on adularia intercalated in silica sinter, and a whole-rock rhyolite was conducted. The rhyolite from sample the Esashi Formation was collected approximately 6 km southwest from the Utanobori mine. The K-Ar age data of the silica sinter and rhyolite yield ages of 15.0±0.4 Ma and 14.6±0.4 Ma, respectively (Table 4).

Table 4. K-Ar age data of the silica sinter, and rhyolite of the Esashi Formation (Sorulen *et al*., 2019)

INS1	Contr No	K (wt. %)	^{40}Ar (radiogenic) (nl/g)	(% total)	Age (Ma)	Comments
20751	UT-14	3.36	1.964	70	15.0±0.4	Adularia intercalated in silica sinter
20752	UT-21	3.36	0.762	27	14.6±0.4	Rhyolite approx. 6 km SW from the Utanobori mine

1: TR: total rock (100-200 micron).

2: Decay constant ^{40}K: $\lambda_\beta = 0.4962 \times 10^{-9}$ yr^{-1}; $\lambda_c = 0.581 \times 10^{-10}$ yr^{-1}.

Isotopic abundance $^{40}K/^{39}K = 0.01167$ % atomic.

Errors are two standard deviations.

2.5.3 Geochemical characteristics of the veins, silica sinter and altered host rocks

The bulk concentration of Au, Ag, Mn, Cu, Zn, Rb, Sr, Sb, Te, Ba, and Pb of the quartz-adularia veins (Type 1 and Type 2 Veins), silica sinters, and least to altered host are presented in Table 5. The Au, Ag and Sb contents of the Type 1 Veins range from 3 to 1078 ppm and from 42 to 1673 ppm and from 42 to 4444 ppm, respectively. For the Type 2 Veins, Au, Ag and Sb contents range from less than 1 to 1 ppm and from 1 to 32 ppm and from 46 to 288 ppm, respectively, and

Table 5. Whole-rock concentrations of selected elements of the quartz-adularia veins (Type 1 Vein and Type 2 Vein), silica sinters, least and altered host rocks of the Utanobori deposit.

ID	Sub-ID	Description	Au ppm	Ag ppm	Mn ppm	Cu ppm	Zn ppm	Rb ppm	Sr ppm	Sb ppm	Te ppm	Ba ppm	Pb ppm
UTS01		Silicified sandstone-hostrock	NA	30.5	62.4	39.4	28.5	164	47.5	263.7	0.06	192.7	8.98
UTS02	a	Silicified sandstone-hostrock	NA	29.5	64.4	49.2	42	138.4	22.4	170.5	b.d	74	6.7
UTS02	b	Type 1 Vein - bulk	29	79	48.3	50	7.5	382.3	21.2	90	0.14	65.6	6.8
UTS02	c	Type 1 Vein - bulk	NA	42.4	97.2	30	8.2	149	39	117.7	0.05	115.4	6.3
UTS03	a	Type 1 Vein - stage I band	94.7	83.3	78.7	52	103.4	665	26.6	67.7	0.11	87	77.5
UTS03	b	Type 1 Vein - stage II band	35.6	114.4	67	31.4	36.7	452	28.5	112.3	0.40	145	21.1
UTS03	c	Type 1 Vein - stage III band	10.7	73.3	123.2	45.5	35.3	173.3	30	42	0.23	77.6	22.7
UTS04	a	Black band in silicified siltstone	0.72	10.5	137.4	45	20	101	43.4	122.4	b.d	188	3.9
UTS04	b	Brown siltstone-mudstone-host rock	NA	8.1	27	23	15.3	198.5	28.6	76	0.07	66.3	2.1
UTS05		Silicified siltstone-sandstone-host rock	NA	7.2	86.3	29	38.5	66	41.7	136.7	0.05	120.3	3.6
UTS06	a	Type 1 Vein - stage I band	74	640	53	43.3	19.6	881.7	42	341	0.82	146.3	4.8
UTS06	b	Type 1 Vein - stage II band	18.6	482.5	81.3	23	7.5	388	36	115.4	0.22	156.3	1.2
UTS07	a	Type 1 Vein - stage I band	1078	1673	76	141.2	67.4	739	27.5	4444	8.2	266.3	105.5
UTS07	b	Type 1 Vein - stage II band	77	633	47.7	62.4	4.6	531	32.2	305	0.43	162	8.0
UTS07	c	Type 1 Vein - stage III band	12	102.7	73.2	35.7	4.6	104	29.5	90.6	0.08	133	2.2
UTS08		Silicified rhyolite of silica sinter	NA	31.3	102	33.2	11.5	27	16.2	72.5	b.d	29	5.8
UTS09	a	Silica sinter, layer F (quartz vein)	1.2	1.02	86.4	34	18.3	57	18	305	b.d	60.6	10.4
UTS09	b	Silica sinter, layer E (quartz vein)	0.77	0.56	101.7	30	16.6	25.5	19.5	136.4	b.d	50.3	14.3
UTS09	c	Silica sinter, layers B, C, D	0.61	0.45	76.2	22.4	11.4	13.7	11.5	394	b.d	32.4	7.6
UTS09	d	Silica sinter, layer A	0.63	0.54	90.2	37.3	24.2	145	35	266	b.d	194	10.7
UTS10	a	Type 2 Vein - transparent vein	0.45	2.2	124	22.6	9.3	7.2	25	288	b.d	18.7	23.2

Table 5 (continued)

UTS10	b	Type 2 Vein - wispy brown vein	0.39	0.87	80.7	18.7	10	11.2	27.5	226.2	b.d	29.7	1.8
UTS10	c	Silica sinter - bulk	NA	1.1	96.6	21.2	8.5	21.6	16.6	221.6	b.d	54	1.7
UTS11		Type 2 Vein - bulk	1.2	10.4	132.3	29.5	4.8	155	27.7	45.6	b.d	108	1.6
UTS12		Silica sinter - bulk	0.78	7.7	110	32.7	6.7	26	18.5	166	b.d	64	1.9
UTS13		Type 2 Vein - bulk	0.54	32	82.3	25.1	45.2	114	32	137.3	b.d	96.6	1.6
UTS14		Type 1 Vein - bulk	2.8	124.3	68.5	14.3	6433	150	27	43	0.12	39.7	3.1
UTS15		Kinkomanai lava	NA	0.43	457.2	14.4	90.3	111.4	233	1.3	0.07	615.5	21.4
UTS16		Kinkomanai lava (silicified and vuggy)	NA	0.28	175.5	17.5	60.2	106.2	205.3	1.01	b.d	566	61.7
UTS17		Tuff of Esashi Formation	NA	0.25	219.4	10	64	53.3	871	3.0	0.09	2759	19
UTS18		Argillic clay	NA	0.71	52.4	16.2	19	130.5	85.2	14.3	0.07	546.4	12.2
UTS19		Argillic clay+pyrite	0.91	0.56	846.3	47.4	154	101	37	3.8	0.17	372.1	21.3
HU	a	Silica sinter brown layer	NA	0.35	61.3	23	20.6	40	19.2	228	b.d	77.2	5.3
HU	b	Silica sinter banded white and black layers	0.51	0.51	46	16.2	12.5	64.3	19	304	b.d	88.4	4.6
HU	c	Silica sinter discontinuous banded white and orange-brown layers	NA	0.73	36.3	46	15	146.3	27.4	233.2	b.d	174.5	5.1

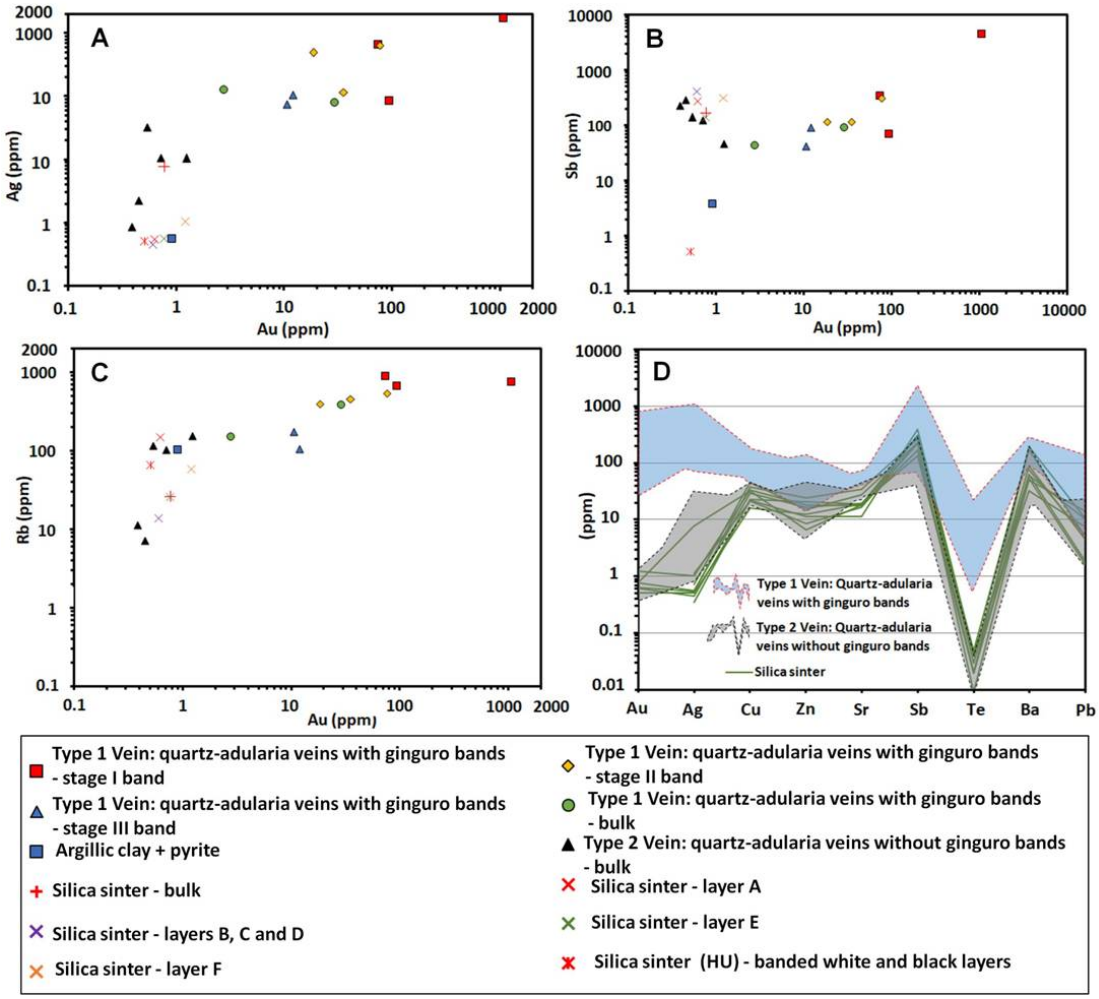

Fig. 17 (A) Log-log plot of Ag and Au contents of the Type 1 and Type 2 Veins, silica sinter, and altered conglomerate and intercalated tuff layer of the Esashi Formation. (B) Log-log plot of Sb and Au contents of the Type 1 and Type 2 Veins, silica sinter, and altered conglomerate and intercalated tuff layer of the Esashi Formation. (C) Log-log plot of Rb and Au contents of the Type 1 and Type 2 Veins, silica sinter, and altered conglomerate and intercalated tuff layer of the Esashi Formation. (D) Multi-elemental plot in log scale for elements Au, Ag, Cu, Zn, Sr, Sb, Te, Ba, and Pb of the Type 1 and the Type 2 Veins and silica sinter.

and the Au, Ag and Sb contents of the silica sinters ranging from less than 1 to 1 ppm and from less than 1 to 8 ppm and from 136 to 394 ppm, respectively. The Ag and Au

(Fig. 17A), Sb and Au (Fig. 17B) and Rb and Au (Fig. 17C) contents of the Type 1 Veins are positively correlated, while those of for the Type 2 Veins, silica sinter and argillic altered samples are scattered. The Au, Ag, Cu, Zn, Sr, Sb, Te, Ba and Pb (in ppm) contents of in the Type 1 Veins (Fig. 17D) are generally higher in contrast with those of the Type 2 Veins and silica sinter.

2.5.4 Chemical composition of electrum

The chemical composition of 10, 20, and 5 electrum grains in the bands I-b and I-d of the Type 1 Vein, and the band II-a of the Type 1 Vein, respectively was determined by SEM-EDS (Appendix 1, KS; Fig. 10, Sorulen *et al*., 2019).

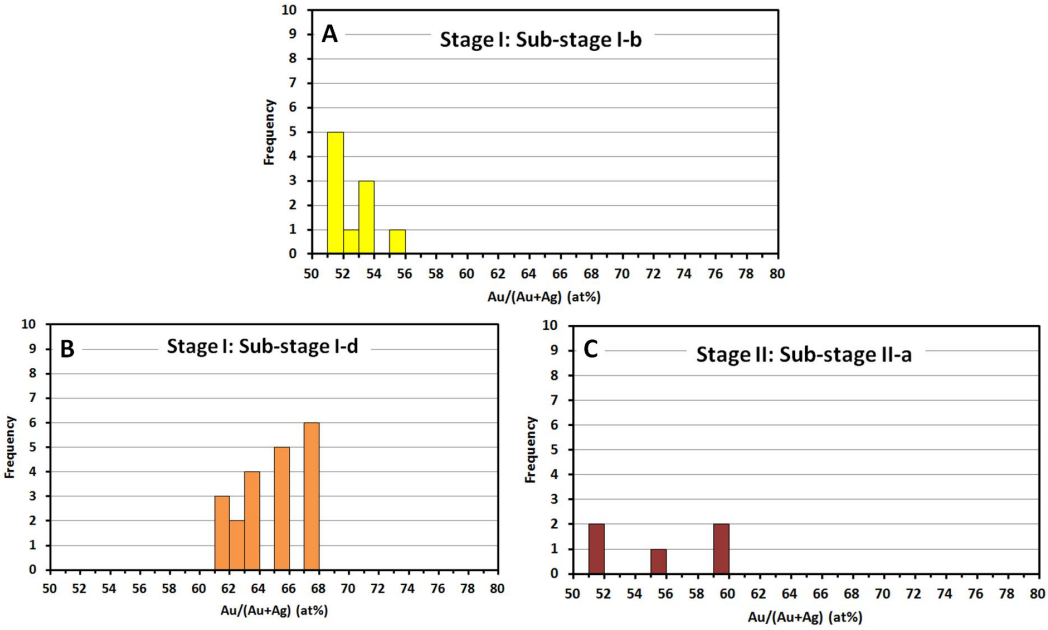

Fig. 18 Electrum composition in band (A) I-b and (B) I-d of stage I and (C) II-a of stage II of the quartz-adularia vein with ginguro (Type 1 Vein).

The Au content of electrum analysis are shown in Figure 18, ranging from 51.0 to 55.3 at% Au (av. 52.5 at% Au), 61.6 to 67.3 at% Au (av. 65.7 at% Au), and

51.2 to 59.8 at% Au (av. 55.5 at% Au) in band I-b of the Type 1 Vein (Fig. 18A), band I-d of the Type 1 Vein (Fig. 18B), and band II-a of the Type 1 Vein (Fig. 18C), respectively.

2.5.5 Trace element chemistry of quartz in the quartz-adularia vein with ginguro band (Type 1 Vein) and silica sinter

The abundance of trace elements of quartz was analyzed on a total of 183 analytical spots across the stages I, II and III bands of the Type 1 Vein (sample UTS07; Figs. 11B-3, 15A), and a total of 50 analytical spots across the layer A (excluding layer A-1) to D of the silica sinter (sample UTS09; Figs. 11B-4; 15C). Profiles with representative photomicrographs of the Type 1 Vein and silica sinter are presented in Figure 19 and Figure 20, respectively. Table 6 shows the number of analysis points, ranges, and averages of the K, Fe, Al, Ti, and Mn concentration in ppm.

Average K and Al concentrations of quartz are high in the bands I-a, I-c, I-e, I-f, I-g of the stage I band of the Type 1 Vein, bands II-c and II-d of the stage II band of the Type 1 Vein, and bands III-a, III-b and III-c of the stage III band of the Type 1 Vein, with the band I-c band of the stage I band, and the band III-c of the stage III band, having a maximum average K and Al concentration of 1619 ppm and 4710 ppm, respectively (Table 6). The Fe concentration of quartz is high in the bands I-a, I-c, I-e and I-g of the stage I band of the Type 1 Vein, and the band III-b of the stage III band of the Type 1 Vein, with a maximum average concentration of 338 ppm in band I-g of the stage I band of the Type 1 Vein. The Ti and Mn contents of quartz are commonly below detection limits, but average Ti concentration of quartz is high in band III-c of the stage III band of the Type 1 Vein.

Table 6 Analytical points, ranges and averages for trace concentration in quartz using EPMA analysis.

Sample type	Stages/layers	Bands/ sub-layers	Number of analysis	K (ppm)	Fe (ppm)	Al (ppm)	Ti (ppm)	Mn (ppm)
Quartz-adularia vein (Type 1 Vein)	I	I-a	13	772-4765 **(1504)**	<31-668 **(103)**	3821-6139 **(4171)**	<37	<39
		I-b	53	<70-1353 (209)	<23-155 (43)	<16-4858 (613)	<37	<37
		I-c	2	1245-1992 **(1619)**	<86-109 **(97)**	<4234-4890 **(4562)**	<23	<20
		I-d	20	<17-897 (174)	<23-70 (20)	<16-3218 (703)	<23	<24
		I-e	9	17-2100 **(799)**	<32-257 **(88)**	<13-5022 **(2767)**	<23-82 (13)	<39
		I-f	4	1162-1287 **(1249)**	<47	3742-3895 **(3840)**	<23	<20
		I-g	2	1619-2092 **(1855)**	31-645 **(338)**	3922-4535 **(4229)**	<23	<24
	II	II-a	29	<232-473 (189)	<47	26-1191 (168)	<30	<20
		II-b	23	<100-4325 (380)	<31	<16-4244 (489)	<23-135 (23)	<39
		II-c	3	921-1129 **(1027)**	<31	3419-5091 **(4493)**	<23	<20
		II-d	2	971-1004 **(988)**	<21	4049-4197 **(4123)**	<23	<20
	III	III-a	1	**1137**	39	**3514**	<23	<20
		III-b	19	714-3321 **(1579)**	<21-326 **(113)**	3159-7420 **(4576)**	<37-45 (20)	<39
		III-c	4	897-1278 **(1085)**	23-78 (39)	4186-5006 **(4710)**	<23-285 **(73)**	<20
Silica sinter	A	0	4	1278-3055 **(2439)**	<21-521 **(257)**	3588-8192 **(5993)**	<23	<24
		2	7	664-2424 **(1531)**	<148-389 **(153)**	2858-6128 **(4268)**	<23	<31
	B	1	9	398-1096 **(844)**	<39-443 **(77)**	2890-4435 **(3672)**	<23-120 (18)	<24
		2	7	149-481 (301)	<54	101-1090 (523)	<23	<20
		3	10	149-714 (424)	<24-62 (30)	175-1498 (564)	<23	<20
	C		10	249-921 **(650)**	<31-78 (42)	603-2196 **(1369)**	<37	<31
	D		4	540-963 **(708)**	<31	826-1826 **(1155)**	<23	<20

Quartz in silica sinter contains high concentrations of K and Al in the layers A-0, and A-2 silica sinter, layer B-1 silica sinter, and in layers C and D silica sinter. Quartz of the layer A-0 of silica sinter contains a maximum average K and Al concentrations of 2439 ppm and 5993 ppm, respectively. The Fe contents of quartz range from <39 to 521 ppm in the layers A-0 and A-2 silica sinter and the layer B-1 silica sinter, with a maximum average Fe concentration of 257 ppm in the layer A-0 silica sinter.

2.5.6 Sulfur isotope compositions of pyrite

Sulfur isotope of pyrite separates (n=2) from the argillic altered inter-beds of conglomerate (sample UTS19) and tuff of the Esashi Formation (sample UTS20) were analyzed (Table 7). The $\delta^{34}S_{CDT}$ values of pyrite of samples UTS19 and UTS20 are -4.3 ‰ and -4.2 ‰, respectively (Figs. 9A; 11H).

Table 7. $\delta^{34}S$ of pyrite (n=2) from argillic altered conglomerate and intercalated tuff layer of the Esashi Formation.

ID	Sample Type	Mineral	$\delta^{34}S$ (‰)
UTS19	Argillic altered conglomerate	Pyrite	-4.3
UTS20	Argillic altered tuff	Pyrite	-4.2

*Argillic altered = proximal to alteration III (Fig. 9A)

2.6. Discussion

2.6.1 Hydrothermal alteration

The central zone of the Utanobori deposit is manifested by silicified rock outcrops and rock floats with quartz veins and silica sinter that characterizes the hydrothermal activity, with an assemblage dominated by quartz and K-feldspar ± chlorite/smectite

mixed layer. The fluids precipitated quartz with K-feldspar-illite-smectite mineral assemblage, indicative of a near neutral pH condition of the hydrothermal fluid, with formation temperature ranging from >90°C to <230°C with depths of <400 m (e.g., Hedenquist *et al.*, 2000).

Quartz + calcite veins were observed to cut the silicified conglomerates at Adit 3 (Fig. 9). Calcite lenses were also reported by MITI (1996) in the Esashi Formation. It is still uncertain how the calcite lenses and veins had formed (e.g., MITI, 1996). MITI (1996) data revealed homogenization temperatures of fluid inclusion in calcite in the calcite lens ranging from 150 to 160°C (n = 20), and reported fluid boiling temperatures ranging from 230 to 240°C (n = 20) from calcite veins. The resultant of such CO_2-rich steam heated water generated argillic alteration characterized by illite, chlorite/smectite mixed layer clays, and kaolinite, indicating a pH of 4-5 (e.g., Hedenquist, 1990; Hedenquist *et al*., 2000). The presence of kaolinite observed in the alteration assemblage is interpreted as a product from steam heated water in the vadose zone, with no observed relationship to the mineralizing event. The fine-grained cubic pyrite in the kaolinite zone may have been deposited by the cooling and interaction of ascending H_2S dominant vapor and available iron in the vadose zone.

The trace amounts of chlorite found in the silica sinter is commonly associated with the late cross-cutting quartz veins and stringers, indicating temperatures >200° in contrast to the silica sinter which initially formed at temperatures <100°C. Microthermometry data of MITI (1996) revealed that homogenization temperature of fluid inclusion in quartz of the silica sinter range from 280 to 310°C (n = 11), which may explain the occurrence of chlorite in silica sinter (and the Type 2 Vein which will be discussed). Trace amount of disseminated adularia in the silica sinter may have

also been introduced by such later overprinting hydrothermal activities at temperatures >100°C.

2.6.2 Mineralization and associated geochemistry

In the quartz-adularia veins (Type 1 Vein and Type 2 Vein) and silica sinter, Au and Ag contents are positively correlated (Fig. 17A), and electrum and naumannite are commonly associated with microcrystalline quartz exhibiting colloform (ghost-sphere) texture in the quartz-adularia veins.

The bulk Rb and Au contents of the stages I, II and III of the Type 1 Vein and those of the Type 2 Veins are positively correlated (Fig. 17C). The precipitation of Au deposited initially with amorphous silica that crystallized to microcrystalline quartz exhibiting colloform (ghost-sphere) texture in the quartz-adularia veins is accompanied with adularia precipitation, implying near neutral pH hydrothermal fluids during mineralization. The bulk Sb and Au contents of the stages I, II and III of the Type 1 Vein and those of the Type 2 Veins are positively correlated (Fig. 17B). The unidentified Fe-Sb oxide and Fe-(Sb)-As oxide commonly occur with electrum and naumannite. Chlorargyrite and bromargyrite [Ag(Cl/Br) - solid solution] were formed after the oxidation of primary silver-bearing minerals.

The Au, Ag, Cu, Zn, Sr, Sb, Te, Ba, and Pb contents of the quartz-adularia veins and silica sinter exhibit similar patterns (Fig. 17D). The mineralized Type 1 Vein contains higher metal values as compared to the silica sinter and the Type 2 Vein. The metal contents of the silica sinter may be explained by the existence of late mineralized cross-cutting Type 2 Vein that extends horizontally as quartz stringers into the silica sinter layers (Figs. 13A, 14D, 17D).

Based on the Ag/Au ratio of native gold and electrum of gold-vein deposits in Japan, Shikazono and Shimizu (1988) suggested that the Ag/Au ratio of native gold and electrum decrease with increasing chloride concentration and temperature. The temperature of deposition of electrum with initial amorphous silica (<200°C) and the Ag content of electrum (avg. 47 at%) at the Utanobori deposit may suggest that Au was transported dominantly by bisulfide complexes (e.g., Shikazono & Shimizu, 1988). Furthermore, the Ag contents of electrum at Utanobori are similar to other epithermal Au-Ag vein-type deposits in Northeast Hokkaido (eg., Sanru and Hokuryu) and in Japan (e.g., Shikazono & Shimizu, 1988). Apart from other physiochemical variables discussed by Shikazono and Shimizu (1988), pH (near neutral, dominated by quartz-adularia mineral assemblage), temperature (<200 °C), activities of selenium (presence of naumannite), hydrogen sulfide (H_2S), and chlorine ion (Cl^-) of hydrothermal fluids may had effectively controlled the chemical composition of electrum in Utanobori.

In the quartz-adularia veins, naumannite (Ag_2Se) was the only observed selenide mineral in this study. Simons *et al*. (1997) suggested that, lower f_{Se} of hydrothermal fluids leads to the deposition of naumannite compared to other selenide minerals, with f_{Se}/f_S lower than unity and fO_2 below or close to the hematite-magnetite buffer. In selenide-bearing epithermal Au-Ag deposits, studies have shown that naumannite may be a likely solubility-controlling phase for silver at lower temperatures (Xiong, 2003), favoring the formation of naumannite at temperatures commonly >100 to <210 °C (Simons *et al*., 1997; Xiong, 2003).

2.6.3 Quartz textures and its relationship to mineralization

In the quartz-adularia veins (Type 1 Veins and Type 2 Veins), quartz stringers and silica sinter, microcrystalline, colloform, comb, zoned, and mosaic, feathery, flamboyant, ghost-sphere and pseudo-acicular quartz textures are described as primary, recrystallization, and replacement textures, respectively (e.g., Adam, 1920; Dong *et al*., 1995). Crustiform to colloform structures were mostly observed in this study, with microcrystalline (colloform) texture as the most common textures observed.

In the Utanobori deposit, three stages with 12 to 14 band were recognized in the quartz-adularia vein with ginguro band (Type 1 Vein); with colloform banding dominant in the main mineralization stage I. Microcrystalline-colloform banded quartz textures associated with ore minerals were formed at temperatures <200^{o}C under high degree of supersaturation (e.g., Henley & Hughes, 2000). The naumannite and electrum dendrites formed especially in the bands I-b and I-d of the stage I of the Type 1 Vein (e.g., Fig. 12A) may imply colloidal transport of ore minerals that eventually precipitated together with amorphous silica in the quartz-adularia veins (e.g., Saunders, 1990, 1996).

Silica sinters formed at the surface were deposited initially as amorphous silica at <100^{o}C from silica super-saturated fluid (Hedenquist & Arribas, 2017). Distinct textural changes of quartz in crystallizing sequence (denoted by "→") from microcrystalline quartz exhibiting colloform-ghost-sphere ± flamboyant → mosaic → comb ± mosaic ± zoned → feathery textures were observed in the bands I-b and II-a and II-c of the stages I and II bands, respectively of the Type 1 Vein (Fig. 15A), bands I-ii, I-iii and I-iv and II-i of the stage I and II bands, respectively of the Type 2 Vein (Fig. 15B), and layers B-1, E and F of the silica sinter that contains horizontal quartz stringers (Fig. 15C).

Ghost-sphere texture is described as a moss texture (e.g., Dong *et al*., 1995), with impurities formed in microcrystalline quartz that recrystallized from initially amorphous silica in the quartz-adularia veins and silica sinter. This texture was observed in microcrystalline quartz, and also faintly in mosaic texture after microcrystalline quartz. Some ghost-sphere texture exhibited radial extinction of flamboyant quartz that crystallized from fibrous chalcedony (e.g., Dong *et al*., 1995; (Fig. 13C). The flamboyant texture was observed as a transitional phase between amorphous silica and microcrystalline quartz (e.g., Camprubi & Albinson, 2007), and not associated with ore minerals.

Mosaic texture formed from the recrystallization of microcrystalline quartz that exhibit colloform (ghost-sphere) texture (e.g., Dong *et al*, 1995). Mosaic texture is found proximal to veins, stringers and vugs that consist of comb ± mosaic ± zoned textures which crystallized from later overprinted hydrothermal activities. The crystallization of mosaic quartz was strongly triggered during later overprinted hydrothermal activities in the quartz-adularia veins (Figs. 12C, B, 13A) and during burial and later overprinted hydrothermal activities in the silica sinter (Fig. 14B, D). The presence of mosaic texture indicates a recrystallization temperature above 180^{o}C (Fournier, 1985).

Comb textures are primary growth textures, where the direction of maximum rate of growth is perpendicular to the growth surface (Dong *et al*., 1995). Comb quartz was observed with colloform-like rhythmic to kinked zoning texture, clearly visible in microscopic observation. Zoning texture requires change of conditions during crystal growth (Fournier, 1985). In the quartz-adularia veins, comb-zoned quartz was observed to enclose early formed ore minerals (Figs. 12C, 13A). Feathery texture formed along the growth tips of comb (zoned) quartz as aggregates of fine-

grained chalcedony (e.g., Dong *et al*., 1995; Fig. 12B). Early comb (zoned) and late feathery quartz are not associated with ore minerals.

Pseudo-acicular texture observed in the late quartz vein (Fig. 13D-2) indicates a replacement texture of early formed minerals by fine-grained quartz. Ore minerals are not associated with this texture.

MITI (1996) documented homogenization temperatures of two-phase liquid-vapor fluid inclusions of the stage I band of the Type 1 Vein, and the stage III band of the Type 1 Vein. In the stage I band, homogenization temperatures of fluid inclusions ranged from 240 to 270°C in euhedral quartz (n = 27). In the stage III band. Homogenization temperatures of fluid inclusions ranged from 220 to 230°C in euhedral quartz (n = 11), and from 170 to 180°C in microcrystalline quartz (n = 28). The homogenization temperatures of fluid inclusions of the stage I band of the Type 1 Vein tend to decrease towards the stage III band of the Type 1 Vein. Homogenization temperatures of calcite vein (230 to 240°C) is intermediate between the homogenization temperatures of fluid inclusions of stage I quartz and stage III quartz of the Type 1 Vein. Such a decreasing trend in homogenization temperatures of fluid inclusions may imply a gradual cooling of the hydrothermal system. The temperatures recorded in the stage I band and stage III band (>200°C) may represent hydrothermal events that occurred after the precipitation of initial amorphous silica that later recrystallized to microcrystalline-colloform banded quartz, resulting in the recrystallization, replacement and primary comb (zoned) quartz textures observed in the stage I band, stage II band and stage III band of the of the Type 1 Vein. Furthermore, the high temperatures recorded for silica sinter (280 to 310°C) does not reflect initial temperatures for its deposition (<100°C), hence implying that later overprinted hydrothermal events had restructured the initial textures and

characteristics of the silica sinter after its formation. Burial and later overprinted hydrothermal activities caused an increase in density and reduction in porosity of the silica sinter. The temperature of formation of silica sinter layers with variable textures can be estimated based on thermophilic microbes that thrive along gradients of pH, geothermal fluid flow rate, fluid composition and temperature (e.g., Hamilton *et al*., 2019). In this study, flattened oval bubble mat-like structures were observed in the darker layers of the silica sinter (e.g., Fig. 11D), suggesting temperature conditions ~45 to 55°C (Hamilton *et al*., 2019). Thin (<2 mm,) and thickly (>1 cm) layered silica sinter (e.g., Fig. 11D) suggest depositional temperatures ~60 to 75°C, and ~25 to ~40°C, respectively with the former situated at proximal slopes adjacent to the vent (Hamilton *et al*., 2019). Palisade texture in the layer C of the silica sinter (Figs. 11B-4, 11C, 14C) suggests temperatures ~30 to 45°C (Hamilton *et al*., 2019). Geyserite indicative of high temperature silica sinter structures (>75°C; Hamilton *et al*., 2019) was not observed in this study.

The occurrence of recrystallization, replacement and primary comb (zoned) textures formed in the quartz-adularia veins and silica sinter are evident that later overprinted hydrothermal activity of temperatures >200°C altered early formed amorphous silica that initially precipitated at temperatures <200°C for the veins, and <100°C for the silica sinter.

Though microcrystalline-colloform banded quartz textures are said to be related with ore mineral precipitation, it should be noted that some sub-stages in the main ore vein (Type 1 Vein) contained trace concentrations of associated ore (e.g., Fig. 15A, bands I-a, I-b, I-c, I-e, I-f, I-g of the stage I band, bands II-b, II-c, II-d of stage II band, and stage III band).

2.6.4 Relationship of trace elements in quartz to mineralization

Cathodoluminescence (CL) has been employed on quartz to observe any defects in crystal lattice and different quartz generations (e.g., Götze., 1996). Several trace elements act as CL activators, including Al, H and Li (Perny *et al*., 1992), Fe (Gorobets *et al*., 1989), Ti (Van den Kerkhof *et al*., 1996), and Ga and Mn (Dudley, 1976). Among them, Al is a common CL activator observed in this study. Charge balance compensators for Al^{3+} can be Na^{+}, K^{+}, H^{+} and Li^{+}, with Ti^{4+} as independent from change compensators (Müller *et al*., 2003).

Trace element spot quantitative analysis on quartz in the quartz-adularia vein with ginguro band (Type 1 Vein) and silica sinter is shown in Figure 19 and Figure 20, respectively. The Al/K ratio and Al content of quartz of the Type 1 Vein and silica sinter are presented in Figure 21.

High Al contents of quartz were observed especially in microcrystalline quartz in the Type 1 Vein and silica sinter, with a maximum of 8129 ppm and 7420 ppm, respectively (Table 6). The Al and K contents of quartz are positively correlated, suggesting that K^{+} acts as a charge compensator for Al^{3+} in quartz of the Type 1 Vein and silica sinter (Figs. 19, 20, 21). Such high Al contents of quartz (>1000 ppm) associated with CL-dark microcrystalline (colloform) quartz with ore in the Type 1 Vein (Figs. 15A; 19), and CL-dark to CL-medium in microcrystalline and mosaic quartz of the silica sinter (Fig. 20) may had been deposited from alkaline low temperature fluids that rapidly precipitated adularia and initial amorphous silica (e.g., Merino *et al*., 1989). This is consistent with the absence of kaolinite in the Type 1 Vein and silica sinter (e.g., Rusk *et al*., 2008; Müller *et al*., 2010).

In the Type 1 Vein, comb ± zoned, feathery and mosaic quartz exhibit CL-dark, CL-intermediate to CL-bright bands, commonly with Al and K contents <150 ppm (Fig. 19). Slightly high Al content of quartz (>150 ppm) is usually observed in

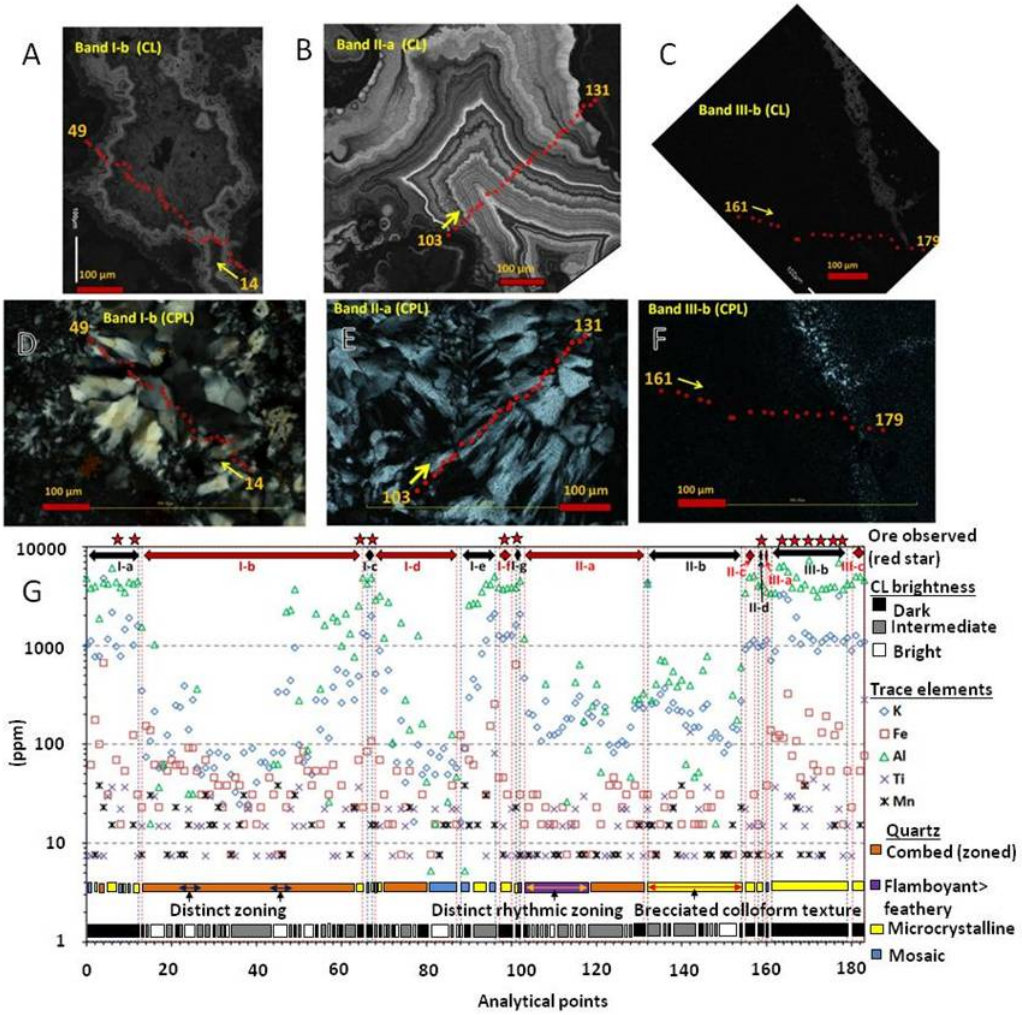

Fig. 19 EPMA spot analysis on quartz of the quartz-adularia vein with ginguro (Type 1 Vein) (sample UTS07). (A) CL image of quartz with band I-b analysis spot from 14 to 49. (B) CL image of quartz with band II-a analysis spot from 103 to 131. (C) CL image of quartz with band III-b analysis spot from 161 to 179. (D) CPL view of photomicrograph A. (E) CPL view of photomicrograph B. (F) CPL view of photomicrograph C. (G) Relationship with CL brightness, K, Fe, Al, Ti and Mn contents and quartz textures of the Type 1 Vein.

the comb ± zoned quartz where CL-intermediate to CL-bright rhythmic and step like zoning are exhibited (Fig. 19A, B, D, E), or near its growth surface proximal to either microcrystalline or mosaic quartz (Fig. 19G, band I-d). The Al content of quartz

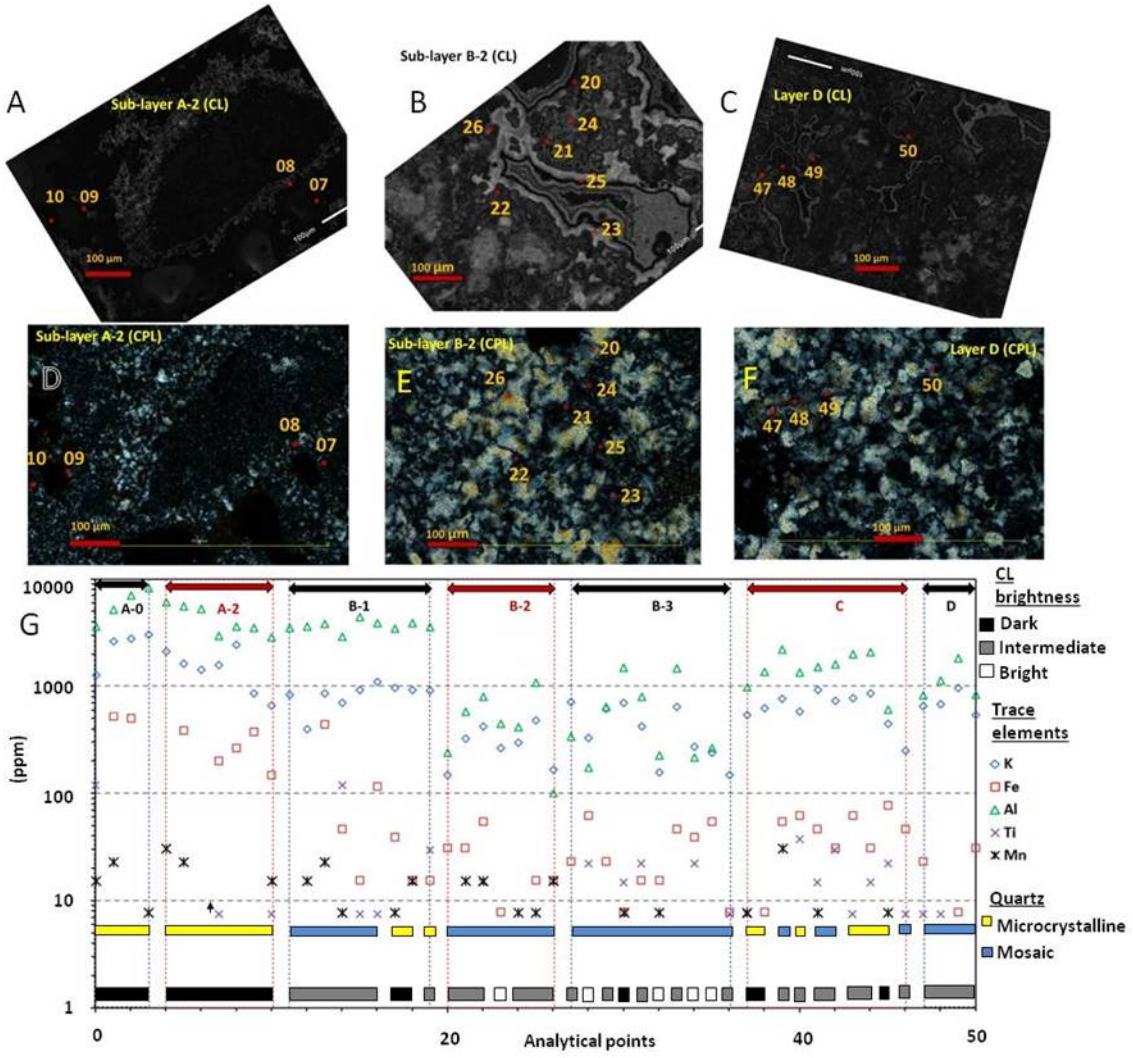

Fig. 20 EPMA spot analysis on quartz of the silica sinter (sample UTS09). (A) CL image of quartz with layer A-2 analysis spot from 07 to 10. (B) CL image of quartz with layer B-2 analysis spot from 22 to 26. (C) CL image of quartz with layer D analysis spot from 47 to 50. (D) CPL view photomicrograph A. (E) CPL view of photomicrograph B. (F) CPL view of photomicrograph C. (G) Relationship with CL brightness, K, Fe, Al, Ti and Mn contents and quartz textures of the silica sinter.

generally decreases towards a quartz crystal that exhibits typical comb texture where Al content of quartz is below the limit of detection. The brecciated microcrystalline-colloform clasts within the matrix of CL-dark microcrystalline quartz commonly

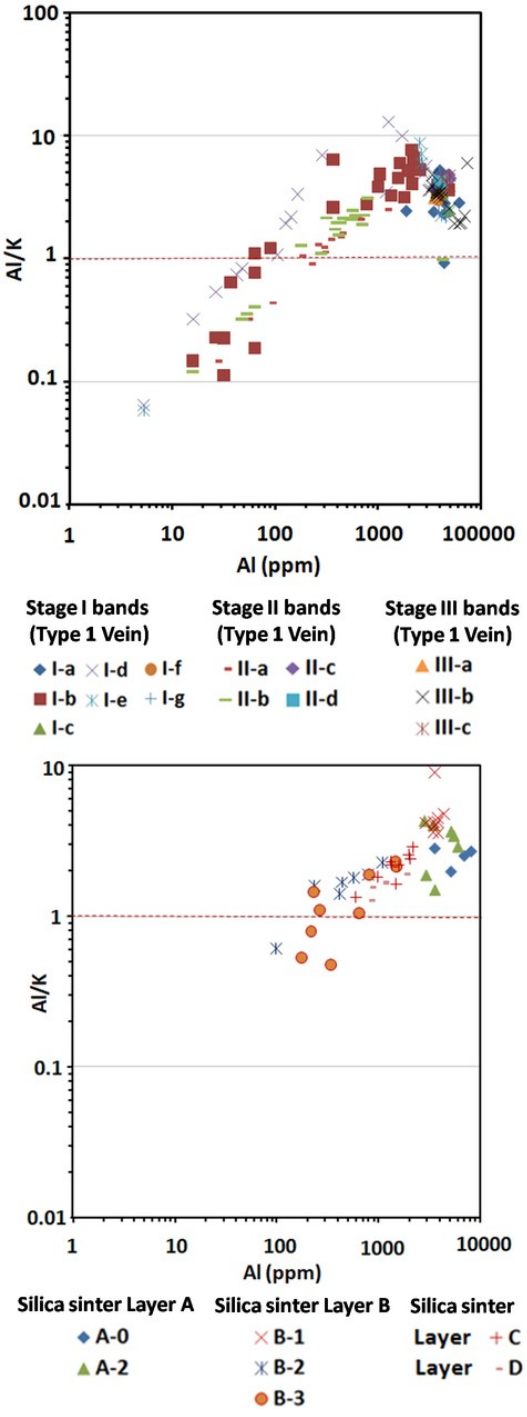

Fig. 21 Diagram showing the Al/K and Al contents of quartz of the (A) quartz-adularia vein with ginguro (Type 1 Vein), and (B) silica sinter.

exhibit CL-intermediate to CL-bright bands with Al and K below 1000 ppm (Fig 19, band II-b). In the Type 1 Vein, Al/K ratios <1 were observed commonly in the comb (zoned), flamboyant and mosaic quartz (Fig. 21A-1). In the layers B-2, B-3 and D of the silica sinter, Al/K ratios are commonly <1 in mosaic quartz, which may be due to the recrystallization of initial amorphous silica and precursor microcrystalline quartz, removing Al and K of quartz (Fig. 21B-1). In the layer C, the Al contents of quartz are commonly greater than 1000 ppm in CL-intermediate to CL-bright microcrystalline quartz. Mosaic quartz in the layer C has similar Al contents (>1000 ppm). This may imply that Al^{3+} was not removed during recrystallization processes (Fig. 20G). Iron is commonly present in CL-dark and CL-intermediate quartz of the Type 1 Vein and silica sinter (Figs. 19, 20). In the Type 1 Vein and silica sinter, average Fe contents of quartz are commonly <60 ppm, which is suggested as a primary feature in quartz of the Type 1 Vein and silica sinter (Table 6; Figs. 19G, 20G). The occurrence of Fe in quartz lattice and its correlated patterns with K in the quartz crystal of Type 1 Vein (Fig. 19G) and silica sinter (Fig. 20G) may suggest the substitution of Fe^{3+} for Si^{4+} atoms in the quartz lattice (apart from Al^{3+}), charge compensated by K^{+} or other charge compensators (e.g., *Müller et al*., 2003). The Ti and Mn are not correlated with CL brightness of quartz in the Type 1 Vein and silica sinter.

2.6.5 Mineralization timing with related igneous activities

Ar-Ar and K-Ar ages of the quartz-adularia vein with ginguro (Type 1 Vein) and silica sinter are shown in Figure 22. Early igneous activity recorded in the vicinity of Utanobori was dated at 16.5 Ma on biotite granite (Maeda *et al*., 1986; Fig. 22). A tuff breccia of the Ofuntanaumanai Formation was dated at 14.3 Ma (Koshimizu & Kim,

1986), and of the Kinkomanai Dacite was dated at 14 Ma (Okamura *et al*., 1995) and 12.1 ± 0.6 Ma (MITI, 1996). Rhyolite of the Esashi Formation dated in this study yielded an age of 14.6 ± 0.4 Ma, in addition to 13.8 ± 0.9 Ma previously obtained on a tuff of the Esashi Formation (Shibata *et al*., 1981). The ages obtained from rhyolite

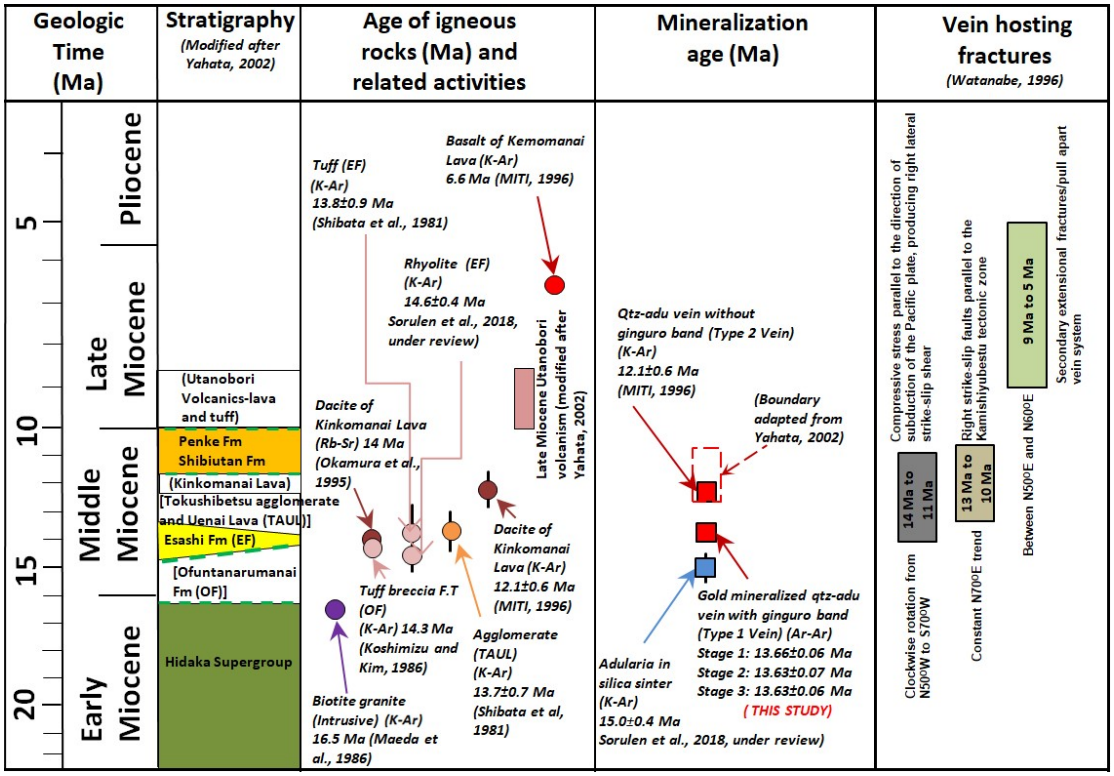

Fig. 22 Summary of the chronology of igneous activities and regional related structures in Utanobori, Northeast Hokkaido (modified after MITI, 1995; Watanabe, 1996; Yahata, 2002). Notes: **Hidaka Supergroup**: Tuff of basaltic rock, pillow lava, slate, sandstone, chert and cordierite biotite hornfels. **Ofutanarumanai Formation (OF)**: Green tuff, tuff breccias, propylitic andesite. **Esashi Formation**: Sandstone, mudstone, conglomerate and tuff. **Tokushibetsu Agglomerate and Uenai Lava (TAUL)**: Opx-cpx andesite pyroclastics rocks. **Kinkomanai lava**: Biotite-hornblende dacite. **Penke Formation**: Sandstone, conglomerate and mudstone. **Shibiutan Formation**: Sandstone, conglomerate and tuffaceous mudstone. **Kemomanai Lava**:

(Fig. 22 continued)

Basaltic andesite and olivine basalt. Green dash line = unconformity, black line = extrapolation from calculated age error in ±.

and dacite samples indicate that rhyolitic subaerial and sub-marine volcanism (e.g., Yahata, 2002) accompanied the deposition of Esashi Formation and the emplacement of the Kinkomanai Dacite during 14.6 Ma to 13.8 Ma. Radiometric dating on adularia in the silica sinter by K-Ar method yielded an age of 15.0 ± 0.4 Ma from this study. From field evidence (Fig. 11B-1, B-2), conglomerate and siltstone were observed peripheral to a silicified rhyolitic tuff, which was buried by the deposition of silica sinter. Such evidence indicates that the silica sinter was formed after rhyolitic volcanism, and volcanic activity may have been responsible for the hydrothermal activity and the deposition of silica sinter. Furthermore, the deposition of rhyolite suggest that an event of rhyolitic volcanism occurred before or during 15 Ma preceding silica sinter deposition (Fig. 11B-1, B-2), further implying that several episodic events of rhyolitic volcanism started prior to silica sinter deposition to 13.8 Ma (Fig. 22). The Rb-Sr and K-Ar ages of the Kinkomanai Dacite at 14 Ma and 12.1 ± 0.6 Ma, respectively may suggest two different events of dacitic volcanism. The first event may had occurred during a break in rhyolitic volcanism around 14 Ma (Fig. 22), and the second related with regional uplifting around 12.1 Ma (e.g., Yahata, 2002).

In Kitami Region of Northeast Hokkaido, the direction of veins was reported by Watanabe (1996) indicating three major trends: (1) a clockwise rotation from N50°W to N70ºE during 14 Ma to 11 Ma, related to the estimated movement direction of the Pacific Plate, (2) a constant N70°E trend from 13 Ma to 11 Ma,

related to the oblique subduction of the Pacific Plate, (3) and a N30°E and N60°E from 9 Ma to 5 Ma, related to secondary pull apart fractures due to the widening of forearc sliver of the Kuril Arc. Faults that host mineralized veins commonly striking ENE to WSW in Utanobori (Appendix 1; MITI, 1996) correspond to the trend of the event (2) (Fig. 22). These faults may have played a major role in the formation of the mineralized veins. Formation age of the mineralized quartz vein is about 13.63 Ma, formed after the first emplacement event of Kinkomanai Dacite (14 Ma), and correlates with the Uenai Lava and Tokushibetsu Agglomerate (Fig. 12, 13.7 ± 0.7 Ma) and rhyolite of the Esashi Formation (13.8 ± 0.9 Ma). The second mineralization event occurred at 12.1 ± 0.6 Ma (MITI, 1996), correlating with regional uplifting and the second emplacement event of the Kinkomanai Dacite (Fig. 22). The second mineralization event may had been associated with the deposition of the quartz-adularia vein without ginguro (Type 2 Vein) cross-cutting the silica sinter, though no cross-cutting relationship were observed between the Type 1 Vein and Type 2 Vein.

The $\delta^{34}S_{CDT}$ values of pyrite (-4.3 and -4.2 ‰, this study; -2.0 and -1.5 ‰, Ishihara *et al*. 2000) and Ag-sulfides in the Type 1 Vein (-0.9 ‰, Ishihara *et al*. 2000) from Utanobori are similar to those in the Kitami district (e.g., Ishihara *et al*. 2000). Negative $\delta^{34}S$ values were possibly due to the interaction fluid derived from magma and ^{34}S depleted sedimentary sulfur of the Hidaka Supergroup basement rocks during hydrothermal fluids migration (Ishihara & Sasaki, 1994).

2.7 Conclusions

Middle Miocene sedimentation occurred with rhyolite volcanism which resulted in the deposition of the Esashi Formation. The deposition of silica sinter began at 15 Ma, followed by subsequent deposition of the Esashi Formation. The gold mineralization

occurred after the deposition of silica sinter around 13.6 Ma, which may had been triggered by rhyolitic volcanism, and again during 12.1 Ma, coinciding with the second emplacement event of the Kinkomanai Dacite (12.1 Ma) and regional uplifting in the region.

Alteration mineralogy indicated that mineralization was associated with near neutral to neutral pH solutions, with kaolinite ± pyrite at places implying an event of steam heated alteration.

Mineralization is commonly hosted in the quartz-adularia vein with ginguro (Type 1 Veins), and was also observed in the quartz-adularia vein without ginguro (Type 2 Veins). Electrum and associated ore minerals are common in the bands I-b and I-d of stage I, and band II-a of stage II of Type 1 Vein. Electrum was also observed in band III–b of stage III of Type 1 Vein. The Type 2 Vein also contains electrum and associated ore, and was observed to cross-cut the silica sinter implying that mineralization occured after the deposition of silica sinter. Ore minerals in both the veins and silica sinter are closely associated with CL-dark microcrystalline (colloform banded) quartz which commonly contain high Al and K contents (>1000 ppm). This implies that early stage generation of initial amorphous silica that eventually recrystallized to microcrystalline quartz was responsible for ore deposition.

The cross-cutting mineralized quartz-adularia veins in the silica sinter suggest that repeated hydrothermal events occurred after silica sinter deposition, subsequently depositing ore minerals in the sinter. In comparison to other low sulfidation epithermal vein-type deposits, this study has shown one of few examples where silica sinter is mineralized by crosscutting ore-bearing veins.

The deposition of the silica sinter around 15 Ma may suggest an earlier mineralizing event associated with quartz-adularia veins not reported at depth.

CHAPTER 3

OCCURRENCE OF THE Fe-Sb OXIDE MINERAL IN THE UTANOBORI GOLD DEPOSIT IN NORTHERN HOKKAIDO, JAPAN

Abstract

The Utanobori gold deposit is a low sulfidation vein-type deposit located in northern Hokkaido Japan. Mineralization at Utanobori is hosted in the Middle to Late Miocene sedimentary and volcanic rocks of the Esashi Formation. Quartz-adularia veins in the Utanobori deposit exhibit three stages of colloform to crustiform banding, with ginguro bands observed in the stage I. In this study, unidentified mineral grains (<5 μm across) and mineral aggregates (>10 to <20 μm across) observed under microscopic observations revealed a chemical composition of Fe-Sb-O phase and a Si-Fe-Sb-Al-K-S-P phase, respectively using scanning electron microscopy with energy dispersive spectroscopy (SEM-EDS). The mineral grains and mineral aggregates are closely associated with electrum, naumannite and secondary goethite, which are all hosted in a matrix dominated by microcrystalline quartz. The identification of the Fe-Sb oxide mineral grain by SEM-EDS and electron probe micro-analyzer (EPMA) spot analyses revealed an Fe:Sb ratio equals 4:1. Such ratio was not reported for antimony oxides and antimonates, suggesting the possibility of a new mineral. Based on chemical calculations obtained from EPMA spot analysis on the Fe-Sb oxide mineral, the chemical formula is proposed to be similar to $Fe_8Sb_2AlSiO_{12}(OH)_{17}$. The crystal structure of the Fe-Sb oxide mineral was not determined due to the minute size of the grains. The aim of this is to reveal the mode of occurrence and chemical composition of the Fe-Sb oxide mineral at the Utanobori deposit.

3.1 Introduction

The Utanobori gold deposit is a low sulfidation vein-type deposit located in northern Hokkaido Japan (Yahata, 2002; Fig. 3). Mineralization is hosted in Middle to Late Miocene Esashi Formation, which consists of conglomerate, sandstone, and tuff. Quartz-adularia veins in the Utanobori deposit exhibits colloform to crustiform banding with silver-rich bands visible in the main ore bearing veins. The deposit was discovered in 1929, and operated until its closure in 1943 [Ministry of International Trade and Industry (MITI), 1996]. Historical production includes crude ore of 19,141 t, with concentrates of 134 kg of gold and 708 kg of silver at average grades of 7g/t and 37g/t, respectively (MITI, 1996). In 2016, Irving Resources Inc. filled 38 prospecting licenses covering 121.55 km^2 of the Utanobori area (Irving Resources Inc., 2019).

Antimony oxides and antimonates which includes apuanite ($Fe^{2+}Fe^{3+}_4Sb^{3+}_4O_{12}S$, Mellini *et al*., 1979), chapmanite [$SbFe_2(SiO_4)_2(OH)$, Walker, 1924], derbylite [$Fe_3Fe_2Ti_2SbO_{13}(OH)$, Hussak & Prior, 1897], hemloite [$(As,Sb)_2(Ti, V, Fe, Al)_{12}O_{23}(OH)$, Harris *et al*., 1989], rinmanite [$(Zn, Mn)_2Sb_2Mg_2Fe_4O_{14}(OH)_2$, Holtstam, *et al*., 2001], schafarzikite ($FeSb_2O_4$, Zemann, 1951), and tripuhyite ($FeSbO_4$, Hussak & Prior, 1897) amongst others include iron, antimony and oxygen in their crystal structure. Schafarzikite and tripuhyite are reported as ultimate sinks for antimony in natural environments (Leverett *et al*., 2012).

This study focuses on the mode of occurrence and mineral composition of an Fe-Sb oxide mineral on the basis of petrography, electron probe micro-analyzer (EPMA) for quantitative chemical composition and mineral mapping of the Fe-Sb oxide mineral, scanning electron microscopy with energy dispersive spectroscopy (SEM-EDS) for semi-quantitative analysis and initial identification of the Fe-Sb oxide

mineral with back scattered electron images (BSE). The aim of this is to reveal the mode of occurrence and chemical composition of the Fe-Sb oxide mineral.

3.2 Geological background

The Utanobori gold deposit is situated at the northwestern end of the Northeast Hokkaido Metallogenic Province, Japan (Fig. 3). Epithermal precious and base metal deposits, volcanic massive base metal sulfides (Kuroko), and subaerial-volcanic exhalative hydrothermal deposits are hosted in the Northeast Hokkaido Metallogenic Province (Yahata, 2002). Mineralization tends to young towards the south, related to Miocene felsic volcanism that shifted southward (Watanabe, 1995, 1996).

The basement rock of the Utanobori deposit consists of mélange complex of Cretaceous to Early Paleogene accretionary complex of the Hidaka Supergroup which consists of slate, sandstone, chert, and limestone (Yamaguchi, 1981). The Hidaka Supergroup is overlain unconformably by the Middle to Late Miocene Esashi Formation which chiefly hosts the mineralized quartz-adularia veins of the Utanobori deposit (Fig. 23; Yamaguchi, 1981; MITI, 1996). The Middle to Late Miocene Kemomanai Lava and Kinkomanai Lava cap the Esashi Formation. The former rock units are then overlain by Late Miocene to Pliocene Penke Formation (Fig. 23; Yamaguchi, 1981). Gold mineralization at Utanobori deposit is reported to be of Middle Miocene age (Yahata, 2002; Sorulen *el at.*, 2019).

The Utanobori deposit sits along a NE-SW trending silicified ridge (Mt. Kanayama) that is manifested by outcrops and floats of silicified rocks, quartz veins and silica sinters (Fig. 23; MITI, 1996). Hydrothermal alteration types consists of (I) quartz + K-feldspar ± chlorite/smectite mixed layer, (II) quartz + K-feldspar + illite ±

smectite, (III) quartz + kaolinite ± illite ± smectite, and quartz + chlorite/smectite mixed layer ± calcite (MITI, 1996; Sorulen *et al*., 2019).

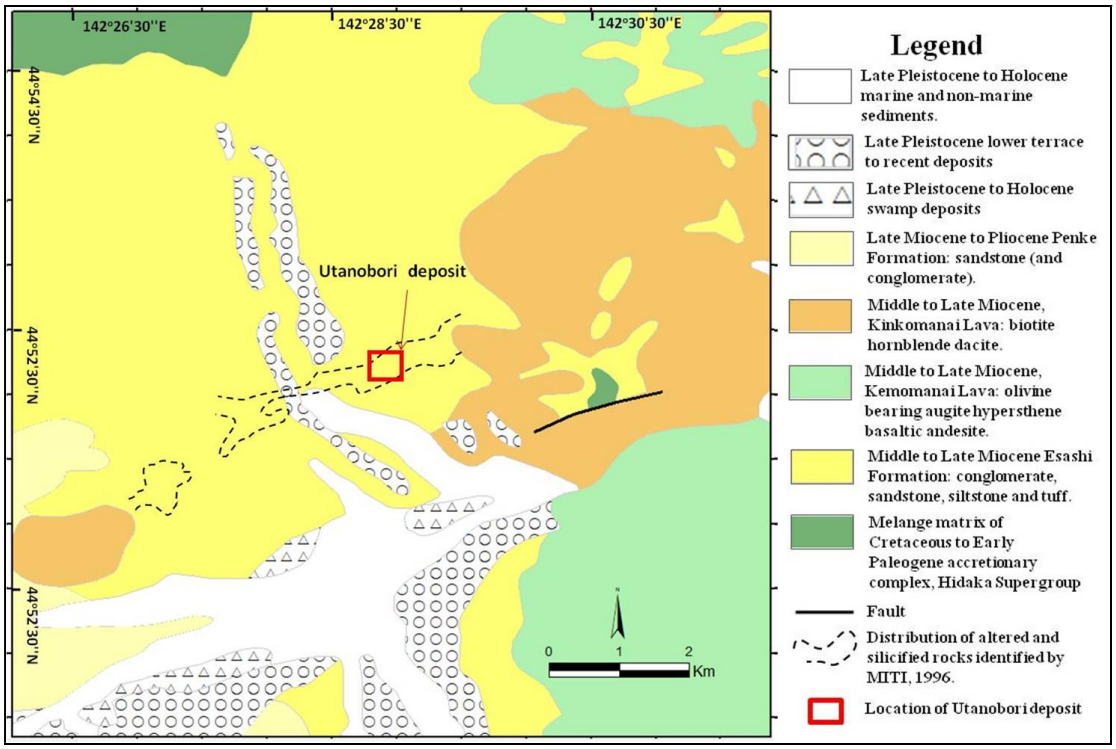

Fig. 23 Geological map of the Utanobori deposit (modified after Yamaguchi, 1981; GSJ, 2009; MITI, 1996; Sorulen *et al*., 2019)

3.3 Materials and Methods

Samples analyzed in this study include three mineralized quartz-adularia veins exhibiting three stages of crustiform-colloform quartz-adularia bandings in hand specimen (Fig. 24). Stage I is characterized by abundant adularia and lesser quartz with two silver-rich bands ("ginguro") <4 mm in thickness. Stage II contains adularia, quartz and discontinuous ginguro band. Stage III is characterized by abundant quartz and lesser adularia. Adularia content decreases from stage I to stage III (Fig. 24).

Thin and polished sections of representative quartz-adularia veins were prepared and petrographic analysis for mineral identification of the Fe-Sb oxide mineral was carried out using a Nikon ECLIPSE LV100N polarizing microscope.

Thin and polished sections were coated with a 20 nm thick carbon film using a JEOL JEC-560 auto carbon coater machine. Semi-quantitative chemical compositions by spot analysis were examined using a JEOL JSM-6610 LV scanning electron microscope (SEM) with an Oxford energy dispersive spectroscope (EDS). Measurement conditions are at 15 kV acceleration voltage, 2.2 nA probe current, high vacuum condition and 10 mm working distance. Low vacuum under 55 Pa conditions were used on non-carbon coated samples to confirm the absence of carbon in the targeted Fe-Sb oxide mineral. SEM-EDS analysis was used for initial identification of mineral phases.

Quantitative chemical composition of the Fe-Sb oxide mineral was determined by a JEOL JXA-8800R Superprobe electron probe micro-analyzer (EPMA) with wavelength dispersion spectroscopy. The calibration was carried out using the following lines, standards, detector crystal and counting time on each peak and same counting times for background: reference standards from the Geological Survey of Japan (GSJ) for Sb ($K\alpha$, Sb, PET, 20 sec), Fe ($K\alpha$, FeS_2, PET, 10 sec), Si ($K\alpha$, Si, TAP, 20 sec), K ($K\alpha$, $KAlSi_3O_8$, PET, 20 sec), Ag ($K\alpha$, Ag, PET, 10 sec), Al ($K\alpha$, Al_2O_3, TAP, 20 sec), P ($K\alpha$, InP, PET, 20 sec), As ($K\alpha$, GaAs, TAP, 20 sec), Al ($K\alpha$, Al_2O_3, TAP, 20 sec), Zn ($K\alpha$, ZnS, LIF, 10 sec), Se ($K\alpha$, SnSe, TAP, 20 sec), Ti ($K\alpha$, TiO_2, PET, 20 sec), S ($K\alpha$, FeS_2, PET, 10 sec), Pb ($K\alpha$, PbS, PET, 20 sec). Measurement conditions were set at 15 kV acceleration voltage, 0.5 nA beam current with a beam diameter of 5μm, working distance of 10 mm, and calculation set for oxides with ZAF correction.

X-ray diffraction by powder analysis and physical properties including cleavage, hardness, streak, density and specific gravity could not be measured due to the fined-grained nature of the Fe-Sb oxide mineral grains (<5 μm) and its close association with secondary goethite.

All analyses were conducted at Akita University in Japan.

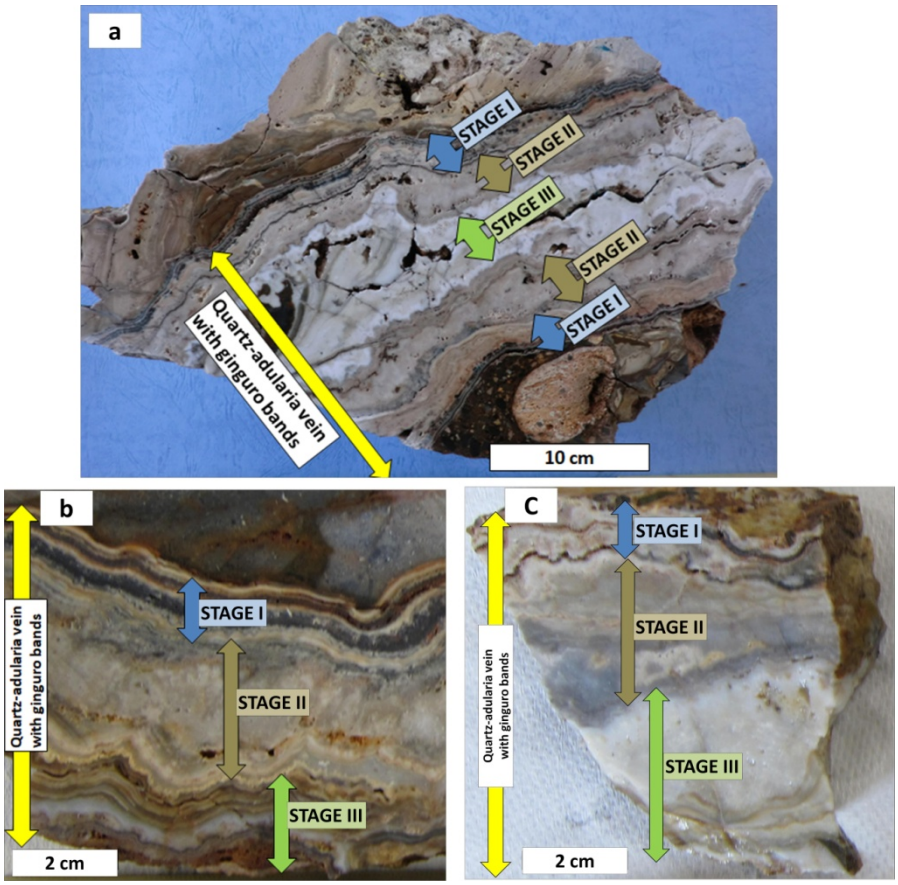

Fig. 24 Main ore-bearing quartz-adularia veins with ginguro bands at the Utanobori deposit used in this study: (a) Float sample KS, a 30 cm symmetrical vein hosted in conglomerate of the Esashi Formation showing three stages of colloform-crustiform quartz-adularia veining with two ginguro bands (<1 mm) in stage I, and milky quartz with vuggy structure in stage III; (b) Outcrop sample UTS-916, quartz-adularia vein hosted in conglomerate and sandstone of the Esashi Formation showing two ginguro bands (<4 mm) in stage I, and stage III exhibiting dominant colloform bandings; (c)

(Fig. 24 continued)

Outcrop sample UTS-915, quartz-adularia vein with two ginguro bands (<1 mm) in stage I, transparent quartz with discontinuous ginguro bands in stage II, and milky quartz and colloform banding in stage III. Analyses were focused on the ginguro bands in stage I of the quartz adularia veins.

3.4. Results

3.4.1 Mode of occurrence of the Fe-Sb oxide mineral

The identification of the Fe-Sb oxide mineral by SEM-EDS spot analysis revealed an Fe:Sb ratio equals 4:1, common in individial grains <40 μm across (Figure 25a, b).

The Fe-Sb oxide mineral occur throughout the stages I, II and III of the quartz-adularia vein, and abundant in the ginguro bands in the stage I. Under refelceted light microscopy, the Fe-Sb oxide mineral exhibits pleochroism from gray to light violet under plane-polarized light (PPL) (Figure 25c, d). Under crossed-polarized light (CPL), the mineral is anisotropic and shows internal reflectance of commonly red. Individual mineral grains are commonly <5 μm across, with very few measureable grains <40 μm across.

SEM-EDS spot analysis on mineral aggregates commonly revealed a Si-Fe-Sb-Al-K-S-P phase (Figure 26a, b).

The mineral aggregates form irregular clusters commonly >10 to >20 μm across, associated with naumannite and electrum. Under reflectedted light microscopy, the mineral aggregates are anisotropic exhibiting gray with bluish tints colors and internal reflectance of commonly orange, dark red to brown (Figure 5c, d).

The aggregates show optical properties similar to goethite, and are in close proximity to the Fe-Sb oxide mineral.

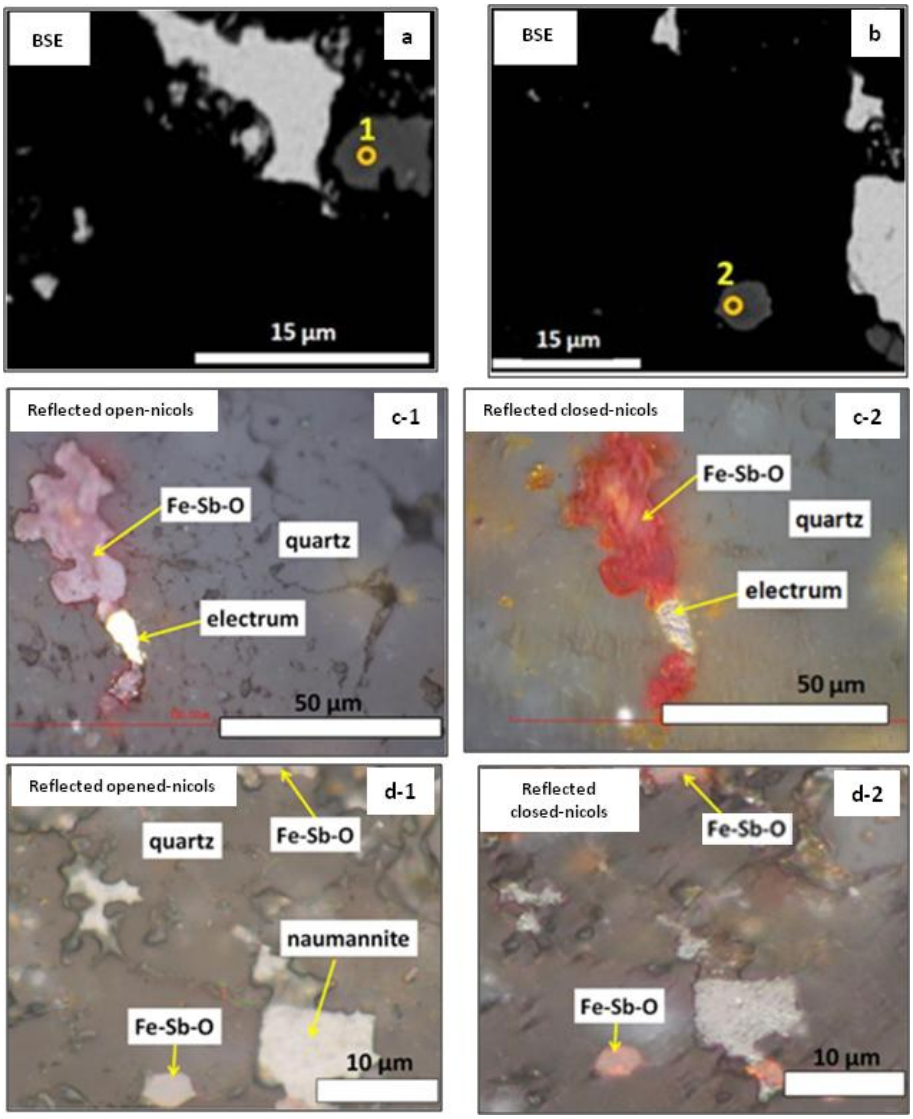

Fig. 25 Photomicrographs of the Fe-Sb oxide mineral: (a, b) BSE images of the Fe-Sb oxide mineral grains observed in the stage I ginguro band in sample KS, with Fe-Sb-Al-As-Si oxide phase determined from spot 1 and 2 with an Fe:Sb ratio equals 4:1 (at. %) from SEM-EDS analysis, with dominant Fe, Sb and O contents (photomicrographs a and b modified from Suzuki, 2015 MS); (c-1) An Fe-Sb oxide mineral grain observed under reflected open-nicols showing colors of gray to light violet; (c-2) Fe-Sb oxide mineral grain in c-1 observed under reflected closed-nicols showing colors of commonly red with minor light violet and orange tint contents; (d-1, 2) Fe-Sb oxide mineral grains observed under reflected (d-1) open nicols and (d-2) closed nicols (photomicrographs c and d modified from Tanaka, 2018 MS).

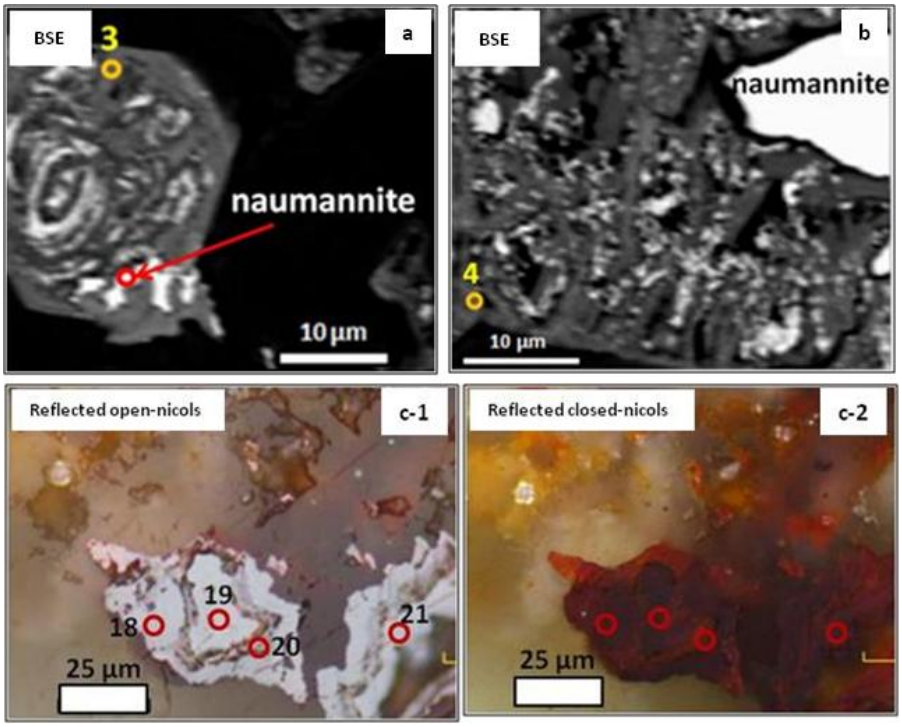

Fig. 26 Photomicrographs of mineral aggregates: (a, b) BSE images of mineral aggregates forming irregular clusters bordered with naumannite containing Si-Fe-Sb-Al-K-S-As-P oxide phase determined from spot 3 and 4 from SEM-EDS analysis; (c-1) Aggregates of the Si-Fe-Sb-Al-K-S-P mineral phase observed under reflected open-nicols showing color gray with slight bluish tint; (c-2) Aggregated mineral grains in c-1 observed under reflected closed-nicols showing colors orange, dark red to brown. EPMA analytical spots are superimposed on photomicrographs in c-1 and c-2.

Dominant gangue minerals are microscrystalline quartz and adularia, the former closely associated with ore minerals. The Fe-Sb oxide mineral appears darker in BSE in contrast to naumannite, electrum and the Si-Fe-Sb-Al-K-S-P mineral aggregate phase which appear brighter (Fig. 26).

3.4.2 Mineral chemistry of the Fe-Sb oxide mineral and mineral aggregates

Concentration of Sb_2O_5, Fe_2O_3, SiO_2, K_2O, Al_2O_3, Ag_2O, P_2O_5, As_2O_5, ZnO, SeO, TiO_2, SO_3, and PbO were analyzed on a total of 21 analytical spots from the Fe-Sb oxide grains and mineral aggregates by EPMA analysis (Table 8). The concentrations of Ag_2O, P_2O_5, ZnO, SeO, TiO_2, SO_3, and PbO are below 1 wt. % in the Fe-Sb oxide mineral grains and mineral aggregates analyzed.

A total of 11 Fe-Sb oxide mineral grains were analyzed. The concentration of Sb_2O_5, Fe_2O_3, SiO_2, K_2O, Al_2O_3, and As_2O_5 of the Fe-Sb oxide mineral range from 19 to 23 wt. % (avg. 23 wt. %), 32 to 48 wt. % (avg. 32 wt. %), 1 to 8 wt. % (avg. 3 wt. %), <1 to 4 wt. % (avg. 1 wt. %), 2 to 7 wt. % (avg. 3 wt. %), and 2 to 4 wt. % (avg. 2 wt. %), respectively (Table 8). Total oxides range from 69 to 81 wt. % (avg. 75 wt. %).

The concentration of Sb_2O_5, Fe_2O_3, SiO_2, K_2O, Al_2O_3, and As_2O_5 of the mineral aggregate range from 10 to 17 wt. % (avg. 14 wt. %), 36 to 62 wt. % (avg. 55 wt. %), <1 to 16 wt. % (avg. 2 wt. %), <1 to 9 wt. % (avg. 1 wt. %), 1 to 12 wt. % (avg. 3 wt. %), and 1 to 3 wt. % (avg. 2 wt. %), respectively (Table 8). Total oxides range from 71 to 86 wt. % (avg. 78 wt. %). A total of 10 analytical spots were analyzed on the mineral aggregates.

EPMA elemental mapping conducted on the Fe-Sb oxide mineral grain in Figure 26c shows correlation between Fe and Sb and traces of Au, Ag, As, Cu and P commonly occurring along the edges of the target mineral (Figure 27). The center of the mineral in Figure 27 shows correlation between S and K with decreasing concentration toward the upper edges of the mineral. Correlation in concentration can also be observed between Ag and Al. The outer margins of the mineral shows an area of high concentration of Si, Al and K which are all correlated, and confirms the occurrence of abundant quartz and adularia associated with the Fe-Sb oxide mineral.

Table 8 Analytical points and concentration of elements presented as oxides (wt. %) in the Fe-Sb oxide mineral grains and mineral aggregates.

Analytical spot	Sample type	Oxides (wt. %)													
		Sb_2O_5	Fe_2O_3	SiO_2	K_2O	Ag_2O	Al_2O_3	P_2O_5	As_2O_5	ZnO	SeO	TiO_2	SO_3	PbO	Total
1	grain	27	40	3.2	0.23	na	3.5	0.53	3.1	na	na	b.d	0.49	na	**78.05**
2	grain	20	43	3.7	0.3	na	3.8	0.27	3.3	na	na	0.02	0.24	na	**74.63**
3	grain	21	45	3.8	0.3	na	3.9	0.36	3.3	na	na	b.d	0.29	na	**77.92**
4	grain	23.59	44.6	1.00	0.23	b.d	2.24	0.59	3.16	b.d	0.05	0.02	b.d	0.12	**75.6**
5	grain	26.53	40.77	1.36	0.39	0.05	2.77	0.48	3.19	0.03	0.07	b.d	0.1	0.09	**75.83**
6	grain	22.7	39.54	0.84	0.25	0.05	3.1	0.64	2.14	b.d	b.d	0.03	0.14	b.d	**69.43**
7	grain	21	43.55	1.55	0.67	b.d	3.52	0.69	2.22	0.08	b.d	b.d	0.09	b.d	**73.36**
8	grain	19.37	42.92	2.67	1.31	b.d	3.45	0.64	2.74	b.d	0.03	b.d	0.13	b.d	**73.25**
9	grain	24.94	47.55	1.69	0.76	0.002	2.58	0.58	2.81	0.09	0.06	b.d	b.d	b.d	**81.06**
10	grain	21.31	32.39	7.6	4.28	0.04	6.87	0.23	2.32	0.16	0.08	0.06	0.11	b.d	**75.44**
11	aggre	10.45	35.78	16.41	8.74	0.3	12.04	0.43	1.19	0.07	0.01	b.d	0.45	b.d	**85.85**
12	aggre	9.81	48.44	3.65	1.79	0.27	4.71	0.66	1.43	0.03	0.01	0.05	0.23	b.d	**71.09**
13	grain	25.21	36.81	0.58	0.17	0.02	2.48	0.55	3.88	0.13	0.07	b.d	0.04	b.d	**69.94**
14	aggre	16.18	56.12	0.49	0.27	0.02	1.2	0.13	3.05	0.2	0.08	b.d	0.17	b.d	**77.91**
15	aggre	14.13	54.66	1.26	0.79	0.36	1.49	0.27	2.99	0.49	0.05	b.d	0.11	b.d	**76.59**
16	aggre	11.44	61.9	0.53	0.02	0.38	1.28	0.35	2.77	0.6	0.08	0.007	0.12	b.d	**79.48**
17	aggre	14.86	60.56	0.49	0.1	0.08	1.09	0.25	2.63	0.4	b.d	0.07	0.3	b.d	**80.85**
18	aggre	17.5	56.8	0.55	0.06	0.006	0.93	0.28	1.57	0.47	0.09	0.03	0.25	b.d	**78.52**
19	aggre	12.43	58.17	0.47	0.03	0.16	1.73	0.41	1.68	0.5	0.09	0.03	b.d	b.d	**75.7**
20	aggre	13.14	55.9	0.51	0.05	0.91	2.17	0.27	2.19	0.42	0.1	b.d	0.11	b.d	**75.77**
21	aggre	16.52	58.54	0.43	b.d	b.d	1.27	0.18	2.45	0.4	0.02	0.001	0.02	b.d	**79.82**

Abbreviations: grain - Fe-sb oxide mineral grain; aggre – mineral aggregate; na – not analyzed; b.d – below detection. Analytical spots 1, 2 and 3 from Tanaka (2018 MS).

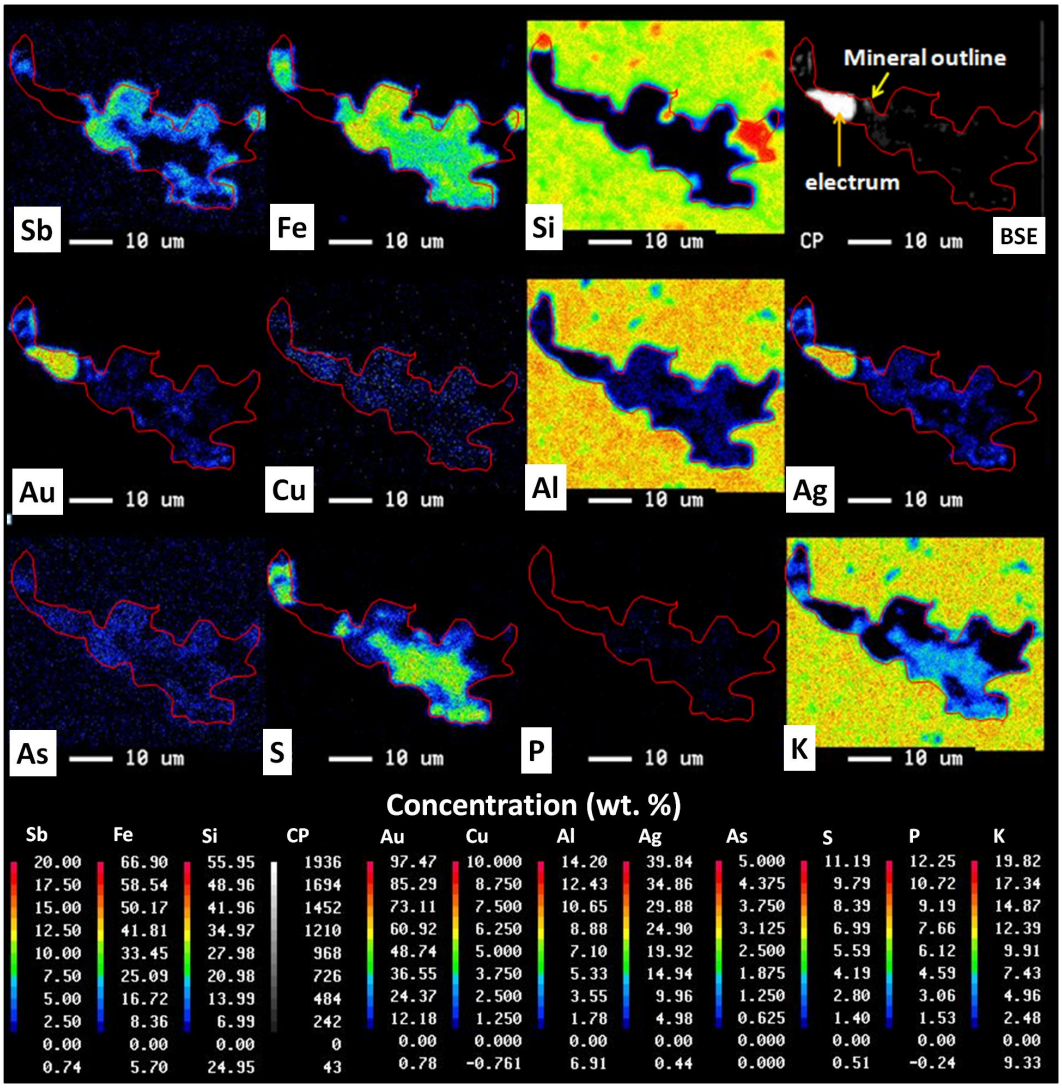

Fig. 27 EPMA elemental mapping showing the concentration (in wt. %) of Sb, Fe, Si, Au, Cu, Al, Ag, As, S, P, and Al of the Fe-Sb oxide mineral in Figure 26c (modified after Tanaka, 2018 MS).

3.5. Discussion

3.5.1 Mineral chemistry

On the basis of EPMA data in Table 8, the average oxides and cation ratio for mineral grains (n = 11) and aggregates (n = 10) were calculated based on the equations shown as below:

Molecular ratio = Weight % (oxide) ÷ Molecular weight (oxide)……....equation 1

Number of cations = Molecular ratio x Number of cations (oxide)…….....equation 2

Charge valence = Number of cation x Cation charge……..equation 3

f(Σ Cation charge) = Σ cation charge ÷ Σ Charge valence……...…equation 4

Cation ration = Charge valence ÷ [f(Σ Cation charge) x Cation charge]….equation 5

Based on equations 1 to 5, the calculated cation ratios are presented in Table 9 for the mineral grains and in Table 10 for the mineral aggregates. The total oxides of the mineral grains and aggregates range from approximately 69 to 81 wt. %, and from 71 to 86 wt. %, respectively, suggesting the presence of water (H_2O) in their crystal structure (Table 8). Based upon this suggestion, hydroxide (OH) was included in the calculation of the cation ratios in Table 9 and in Table 10, with the calculated H_2O values for the mineral grains ranging from approximately 19 to 31 wt. %, and from 14 to 29 wt. % for the mineral aggregates (Table 8). The reasons of such suggested H_2O content of the mineral grains and aggregates remains unclear, but is higher in comparison to minerals such as goethite with 10.14 wt. % H_2O content (Posnjak & Merwin, 1919), chapmanite with 2.07 wt. % H_2O content (Walker, 1924), derbylite with 1.25 wt. % H_2O content (Hussak & Prior, 1897), hemloite with 0.86 wt. % H_2O content (Harris *et al*., 1989) and rinmanite with 2.01 wt. % H_2O content (Hussak & Prior, 1897).

The mineral chemical formula was determined from Table 9 since the mineral aggregates (Table 10) are commonly mixed with electrum, naumannite and secondary goethite (e.g., Fig. 26). Though the crystallography of the Fe-Sb oxide mineral (initially identified using SEM-EDS) was difficult to measure due to its fineness by using X-ray diffraction method, its proposed calculated chemical formula

Table 9 Calculated cation ratio values for the Fe-Sb oxide mineral grains using Table 8 and equations 1 to 5.

Molecules	**Molecular weight**	**Avg. wt. % (n = 11)**	**Molecular ratio**	**Number of cations**	**Charge valence**	**Cation ratio**	**Sb = 1**	**Cations**	**Cation ratio**
Sb_2O_5	323.5	22.97	0.07	0.14	0.71	0.01	1	Sb	1
Fe_2O_3	159.7	41.47	0.26	0.52	1.56	0.05	3.66	Fe	4
Al_2O_3	101.96	3.47	0.03	0.07	0.2	0.01	0.48	Al	0.5
TiO_2	79.88	0.01	0.0002	0.0003	0.0006	0.00002	0.001	Ti	0.001
SiO_2	60.09	2.54	0.04	0.04	0.17	0.004	0.3	Si	0.3
K_2O	94.2	0.81	0.01	0.02	0.02	0.002	0.12	K	0.1
As_2O_5	229.84	2.92	0.01	0.03	0.13	0.002	0.18	As	0.2
P_2O_5	141.94	0.5	0.004	0.01	0.04	0.0007	0.05	P	0.1
Ag_2O	231.74	0.02	0.00007	0.0001	0.0001	0.00001	0.0009	Ag	0.001
ZnO	81.39	0.04	0.0005	0.001	0.002	0.0001	0.01	Zn	0.008
PbO	223.2	0.02	0.00009	0.0002	0.0003	0.00002	0.001	Pb	0.001
SeO	94.96	0.03	0.0003	0.0007	0.001	0.00007	0.005	Se	0.005
SO_3	80.07	0.15	0.002	0.002	0.01	0.0002	0.01	S	0.01
OH	17	26	1.53	1.53	1.53	0.15	10.77	H	11
Total		100.95			4.37				
Σ Cation charge	46			f(Σ Cation charge)	10.53				

Table 10 Calculated cation ratio values for the mineral aggregates using Table 8 and equations 1 to 5.

Molecules	**Molecular weight**	**Avg. wt. % (n = 10)**	**Molecular ratio**	**Number of cations**	**Charge valence**	**Cation ratio**	**Sb = 1**	**Cations**	**Cation ratio**
Sb_2O_5	323.5	13.65	0.04	0.08	0.42	0.01	1	Sb	1
Fe_2O_3	159.7	54.69	0.34	0.68	2.05	0.06	8.12	Fe	8
Al_2O_3	101.96	2.79	0.03	0.05	0.16	0.01	0.65	Al	1
TiO_2	79.88	0.02	0.0002	0.0005	0.001	0.00002	0.003	Ti	0.003
SiO_2	60.09	2.48	0.04	0.04	0.17	0.004	0.49	Si	0.5
K_2O	94.2	1.18	0.01	0.03	0.03	0.002	0.3	K	0.3
As_2O_5	229.84	2.19	0.01	0.02	0.1	0.002	0.23	As	0.2
P_2O_5	141.94	0.32	0.002	0.005	0.02	0.0004	0.05	P	0.05
Ag_2O	231.74	0.25	0.001	0.002	0.002	0.0002	0.03	Ag	0.03
ZnO	81.39	0.36	0.00	0.01	0.02	0.0008	0.1	Zn	0.1
PbO	223.2	0.00	0.0000	0.0000	0.000	0.00	0.00	Pb	0
SeO	94.96	0.05	0.0005	0.001	0.002	0.0001	0.01	Se	0.01
SO_3	80.07	0.18	0.002	0.002	0.01	0.0002	0.03	S	0.03
OH	17	22	1.29	1.29	1.29	0.12	15.34	H	15
Total		100.16			4.28				
Σ cation charge	46			f(Σ cation charge)	10.75				

may be similar to $Fe_8Sb_2AlSiO_{12}(OH)_{17}$ (e.g., Tanaka, 2018 MS).

The Sb, Fe and As contents (in wt. %) of the mineral grains and mineral aggregates were calculated from Table 8 and are shown in Table 11.

Table 11. Concentration of Sb, Fe and As contents (in wt. %) in the Fe-Sb oxide mineral grains and mineral aggregates calculated from Table 8.

Analytical spot	Sample type	Sb wt. %	Fe wt. %	As wt. %
1	grain	10.2	14	1.01
2	grain	7.5	15	1.08
3	grain	7.9	15.7	1.08
4	grain	8.9	15.6	1.03
5	grain	10	14.3	1.04
6	grain	8.5	13.8	0.70
7	grain	7.9	15.2	0.72
8	grain	7.3	15	0.89
9	grain	9.4	16.6	0.91
10	grain	8	11.3	0.76
11	agrre	3.9	12.5	0.39
12	agrre	3.7	16.9	0.47
13	grain	9.5	12.9	1.26
14	aggre	6.1	19.6	1.00
15	aggre	5.3	19.1	0.97
16	aggre	4.3	21.6	0.90
17	aggre	5.6	21.2	0.86
18	aggre	6.6	19.9	0.51
19	aggre	4.7	20.3	0.55
20	aggre	4.9	19.5	0.71
21	aggre	6.2	20.5	0.80

Abbreviation: Aggre – mineral aggregate; grain – Fe-Sb oxide mineral grain

The Fe-As-Sb ternary plot in Figure 28 shows the composition of hydrous ferric oxides (HFO), goethite, tripuhyite, minerals with pyrochlore structure, cervantite ($Sb^{3+}Sb^{5+}O_4$), senamontite (Sb_2O_3) and scorodite ($FeAsO•2H_2O$) from several Sb deposits in Slovakia (Lalinska *et al*., 2012). The Sb, Fe and As contents in

Table 11 were plotted on Figure 28. The plot shows the mineral grains and mineral aggregates correspond to tripuhyite and goethite and HFO field, respectively.

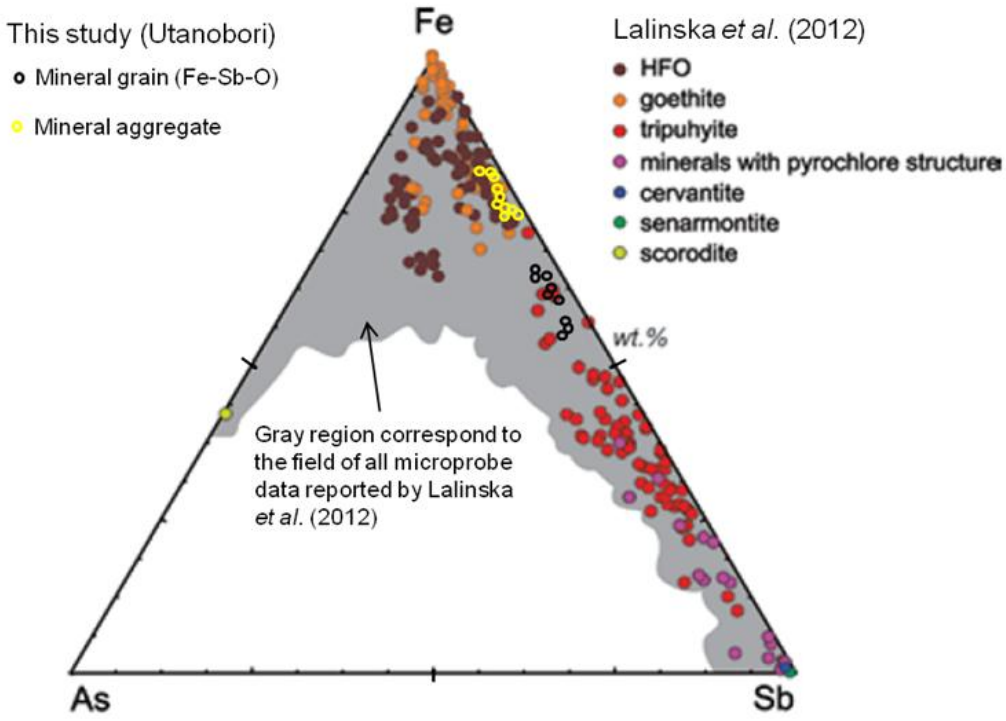

Fig. 28 Fe-As-Sb ternary plot of the mineral grains (Fe-Sb oxides) and mineral aggregates at the Utanobori deposit compared with HFO, goethite, tripuhyite, minerals with pyroclore structure, cervantite, senamontite and scorodite data from Lalinska *et al.* (2012). All data derived from EPMA and presented in wt. %. Ternary plot modified from Lalinska *et al.* (2012).

HFO minerals include ferrihydrite [$(Fe^{3+})_2O_3 \bullet 0.5H_2O$], akaganéite [$(Fe^{3+}, Ni^{2+})_8(OH,O)_{16}Cl_{1.25}$], feroxyhite [$Fe^{3+}O(OH)$], lepidocrocite [FeO(OH)], limonite [$FeO(OH)\cdot nH_2O$] and goethite. The mineral aggregates has an Fe:Sb ratio equals 8:1 (Table 10), which may suggest a chemical composition that may be similar to goethite or other HFO (Fig. 28). Though some studies reported high Sb contents in goethite up

to 19.25 wt. % (e.g., Lalinska *et al*., 2012), it still remains uncertain if the mineral aggregates are actually goethite or other HFO due to the lack of X-ray diffractometry data (Fig. 28). The Al content may be due to minute inclusions of adularia contained in the mineral aggregates (Table 10).

The mineral grains (Fe-Sb oxides) plot in the field of tripuhyite (Fig. 28). The calculated Fe:Sb ratio using EPMA (and SEM-EDS) on the mineral grains equals equals 4:1 (Table 9), an unreported ratio for antimony oxides and antimonates which includes tripuhyite (Fe:Sb ratio equals 1:1, Berlepsch *et al*., 2003). The Fe:Sb ratio of the mineral grains in the Utanobori deposit may suggest the possibility of a new mineral, though no X-ray diffractometry was used to identify its crystallography.

3.5.2 Mineral association and relationship

Minerals associated with the Fe-Sb oxide mineral grains and mineral aggregates observed in this study include microcrystalline quartz, electrum, naumannite, secondary goethite and adularia (Figs. 25, 26, 27). Phases identified using EPMA elemental mapping in Figure 27 associated with the Fe-Sb oxide mineral grain consist of Cu-As-S and Al-K-P. Small inclusions of electrum grains were also observed (Au-Ag, Fig. 27). The Si-Fe-Sb-Al-K-S-P oxide phase identified using SEM-EDS analysis make up the mineral aggregate phase (Fig. 26), though Si appeared to be lower when analyzed using EPMA.

In this study, the Fe-Sb oxide mineral and mineral aggregates observed in Utanobori deposit is proposed to be secondary, though no primary antimony minerals were observed (e.g., Sorulen *et al*., 2019; MITI, 1996). The primary source of Sb (e.g., stibnite) in Utanobori deposit is unknown.

Studies by Leuz *et al.* (2006a) showed that in acidic pH range, the co-oxidation of Sb (III) was similar for Fe (II, III) (Fe:Sb ratio near 1), but in alkaline regions (pH> 7), oxidation was effective in accelerating oxidation kinetics, with Fe:Sb > 3:1. Such mechanism and reaction between the oxidation of Sb (III) in the presence of Fe (II, III) and oxygen may be used to explain the cation ratio of Fe:Sb in the Utanobori deposit, but due to lack of evidence, this suggestions remains unsolved.

3.6 Conclusions

The Utanobori deposit is host to an Fe-Sb oxide mineral that commonly occurs as isolated grains (commonly <5μm across) with a proposed chemical formula similar to $Fe_8Sb_2AlSiO_{12}(OH)_{17}$. On the other hand, mineral aggregates with a chemical phase that consist of Si-Fe-Sb-Al-K-S-P are also hosted in the Utanobori deposit.

The Fe:Sb ratio of the Fe-Sb oxide mineral equals 4:1, a ratio not reported in literatures and suggest the possibility of new mineral.

From EPMA data, it is suggested that the water content of the Fe-Sb oxide mineral grains and mineral aggregates approximately range from 19 to 31 wt. %, and from 14 to 29 wt. %, respectively.

In this study, the Fe-Sb oxide mineral grains and mineral aggregates are associated with microcrystalline quartz, electrum, naumannite, secondary goethite and adularia.

An X-ray diffractometry is recommended for the crystallography and confirmation of the Fe-Sb oxide mineral grains and mineral aggregates to facilitate the geochemical work done in this study.

CHAPTER 4

GEOCHEMICAL CHARACTERISTICS OF THE OMU SILICA SINTER AND OMUI QUARTZ VEINS IN NORTHERN HOKKAIDO, JAPAN

Abstract

The Omui gold deposit is a low sulfidation epithermal vein-type deposit located in the northern part of Hokkaido, Japan. The deposit is composed of the Nanko and Honpi ore bodies which are hosted by Neogene rhyolite lapilli tuff of the Motoineppu Lava. Gold-mineralization in the Honpi and Nanko are characterized by quartz veining exhibiting banded silver-rich and brecciated bands. Three stages were recognized in the Honpi veins, and their Au, Ag and Sb contents were determined using an inductively coupled plasma-mass spectrometry (ICPMS); an early (Au: 82 ppm, Ag: 2315 ppm, Sb: 189 ppm), middle (Au: 16 ppm, Ag: 333 ppm Sb: 125 ppm), and late stage (Au: 2 ppm, Ag: 56 ppm, Sb: 147 ppm). The early and middle stages represent the main stages of ore deposition. The middle stage is characterized by intense hydrothermal brecciation. Ore minerals include electrum, stephanite and argentite, commonly associated with quartz. Chemical composition of electrum determined by scanning electron microscope with energy dispersive spectroscopy ranges from 29.9 to 49.3 at% Au (av. 42.6 at% Au) in the Honpi vein. Hydrothermal alteration determined from X-ray diffractometry in the Neogene volcanic and sedimentary rocks grades outward from (1) silicification → quartz ± K-feldspar ± kaolinite ± illite → (3) quartz ± K-feldspar ± kaolinite ± illite ± calcite → (4) smectite ± quartz ± K-feldspar, implying near-neutral conditions for ore deposition.

Approximately 8 km north of the Omui deposit, silica sinter terraces crop out (Omu sinter) along the eastern banks of the Otoineppu River. The Omu sinter is

massive and brecciated at intervals. The silica sinter is 3.2 m high and dips gently NW. Twenty nine (29) layers were recognized. Structures of the silica sinter observed includes thick (massive) and finely laminated, sinter clast breccia, low-amplitude wavy stromatolite, network and streamer fabrics, geyserite eggs, and plant-rich sinter. The Au content of the sulfide-rich brecciated base of the silica sinter is >1 ppm, and >0.1 ppm in the upper sinter clast breccia layers. The Au and Ag contents of the silica sinter are positively correlated. Base on studies conducted on thermophilic microbes that thrive along gradients of pH, geothermal fluid flow rate, fluid composition and temperature of the silica sinter lithofacies, geyserite eggs suggest temperatures of deposition range from >75ºC, and from ~60 to 75ºC for the thinly laminated, and from ~25 to ~40ºC for the thickly laminated and plant-rich sinter layers. K-Ar dating conducted on hornblende of a Rhyolite Dike reveals an age of 14.3 Ma, suggesting that the Rhyolite Dike pre-dates the Motoineppu Lava that hosted the quartz veins at the Omui deposit. The relationship of the Rhyolite Dike to mineralization is uncertain, but it may had played a role as a heat source for hydrothermal activities. The ore-forming age is not yet reported.

4.1 Introduction

The Omui deposit is an epithermal vein-type gold deposit (Yahata, 2002) located at the northern part of Hokkaido, Japan (Fig. 3). Age of mineralization at the Omui deposit was reported to be of Middle Miocene (Yahata, 2002). Mining activity in Omui commenced in 1925 by Fujita Mining Co. and ceased operations in 1928 [Steffen, Robertson and Kirsten (SRK), 2018]. Reported historical productions include 0.34 t Au and 8.5 t Ag (SRK, 2018). In 2016, Irving Resources Inc. secured a mining license covering 2.98 km^2 of the Omui area, and an additional 50 prospecting

licenses over 152.03 km^2 of the northeast-trending Omu Volcanic Graben (Irving Resources Inc., 2019). The Omu silica sinter was discovered by Irving Resources Inc. in 2016 south of the Otoineppu River. Mineralized veins at the Omui deposit are hosted in rhyolite of the Motoineppu Lava (SRK, 2018).

Regional geology was reported by Suzuki *et al*. (1966). Mineralization was reported by Mining and Materials Processing Institute of Japan (MMIJ) (1990), Sillitoe (1993) and Yahata (2002). Age dating was conducted on the Motoineppu Lava, Inashibetsu Lava, Nakahoronai Lava and Kamiomu Formation by Koshimizu and Kim (1987), Watanabe and Yamaguchi (1991), and Watanabe *et al.* (1995), respectively. The tectonic model of epithermal gold mineralization in Northeast Hokkaido and genesis of fractures that host veins in the Kitami Region of Hokkaido were discussed by Watanabe (1995, 1996). Exploration activities by Irving Resources includes stream sediment and rock chip geochemistry, gravity and magnetic survey covering an area measuring approximately 18 x 18 km^2 which includes the Omui and Omu areas, and high spatial resolution Light Detection and Ranging (LiDAR) topographic models were carried out as part of Irving Resources Inc. exploration effort (SRK, 2018). Drilling at the Omu sinter by Irving Resources Inc. reported high Au and Ag grades from a 0.32 m interval (from 184.93 m to 185.25 m) of hole 190MS-002 (e.g., Chapter 1.2.2; Irving Resources Inc. news release, May 06th 2019). The Au and Ag content are 118.5 g/t and 1410 g/t, respectively of the 0.32 m interval of banded quartz vein displaying ginguro, silver sulfide minerals (Irving Resources Inc. news release, May 06th 2019).

In this study, mineralization stages are identified in the Omui main vein ("Honpi"), and layers of the Omu silica sinter are distinguished. Hand and outcrop sample observations and ICP-MS analysis were carried out on the representative veins

and silica sinter samples in this study. Data sourced from Kuzumaki (2018 MS) and Zeeck (2018 MS) are made mention in this Chapter. K-Ar method on hornblende in a Rhyolite Dike was conducted in this study.

4.2 Geological background

The Omui deposit and Omu silica sinter are located in the northern part of Hokkaido Japan, centered at 44°32'9.60"N and 142°54'26.80"E in the Northern Hokkaido Metallogenic Province, Japan (Figs. 3). Epithermal vein-type precious and base metal deposits, vein and disseminated-type Hg, and volcanic rock-hosted massive sulfide deposits (Kuroko) are hosted in the Northeastern Hokkaido Metallogenic Province (Hasegawa et al., 1983; Yahata, 2002). Formational age of deposits tend to young towards the south following the southward shift of the volcanic front and related volcanism (Watanabe, 1996; Fig. 3).

The Omui and Omu areas sits on a basement consisting of the Mesozoic accretionary complex of the Hidaka Supergroup made up of sandstone and slate (Suzuki *et al*., 1966; Fig. 29). The basement was then overlain by the Miocene Kamiomu Formation consisting of sandstone, shale, breccia and tuff (Suzuki *et al*., 1966; Fig. 29). Age dating conducted on tuff of the Kamiomu Formation revealed an age of 14.3 ± 1.0 MA (Suzuki *et al*., 1966; Fig. 29). The early rocks are covered by the Miocene Nakahoronai Lava (Suzuki *et al*., 1966; Fig. 29). Age dating conducted on andesite by Watanabe *et al*. (1991) revealed an age of 12.9 ± 0.5 Ma. The mineralized veins of the Omui deposit are commonly hosted in the Miocene Motoineppu Lava which consists of rhyolite (Suzuki *et al*., 1966; Fig. 29). Koshimizu and Kim (1987) revealed an age of 12.0 ± 0.9 Ma on rhyolite. The former rocks are then covered by the Miocene Inashibetsu Lava (Suzuki *et al*., 1966; Fig. 29). Age

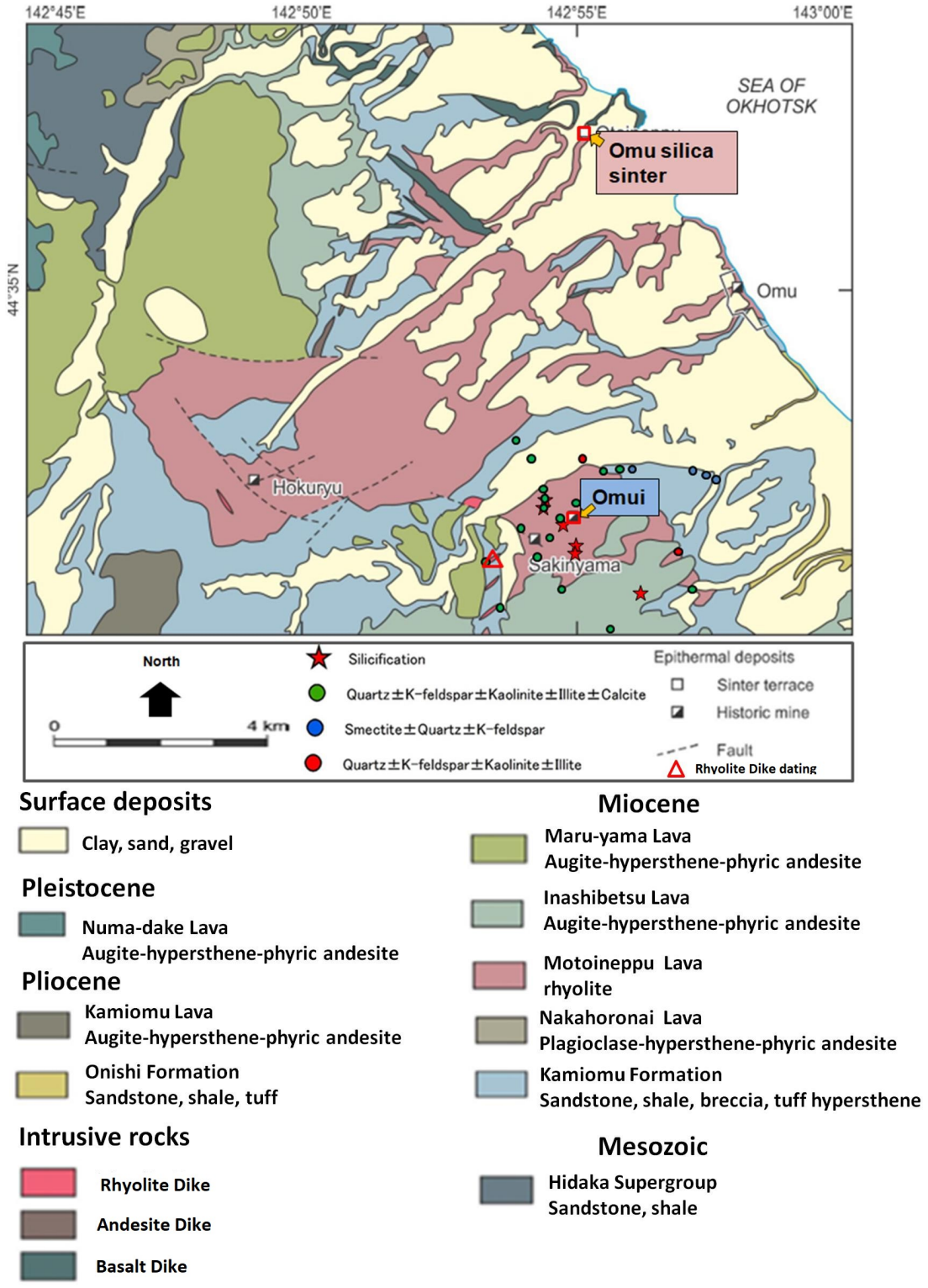

Fig. 29 Geologic and alteration map of the Omui deposit and Omu silica sinter areas (modified from Zeeck, 2018 MS, originally from Suzuki *et al.*, 1966). Alteration assemblages from Kuzumaki (2018 MS).

dating conducted on andesite revealed an age of 9.8 ± 0.5 Ma (Watanabe and Yamaguchi, 1988). Late Miocene Maru-yama Lava covered the early rocks and consists of augite-hypersthene-phyric andesite (Suzuki *et al*., 1966; Fig. 29). The Pliocene rock composes of Onishi Formation which is then covered by the Kamiomu Lava (Suzuki *et al*., 1966; Fig. 29). The Omu silica sinter is bordered by the Motoineppu Lava and the Pleistocene Numa-dake Lava (Suzuki *et al*., 1966; Fig. 29). Intrusive rocks include the Basalt Dike, Andesite Dike and Rhyolite Dike (Fig. 29).

The Omui quartz veins generally trend NNE-WWS to E-W (e.g., Watanabe, 1996). Silicification grades out to quartz ± K-feldspar ± kaolinite ± illite ± calcite, to smectite ± quartz ± K-feldspar, and quartz ± K-feldspar ± kaolinite ± illite (Fig. 29; Kuzumaki, 2018 MS).

4.3 Samples and analytical methods

Alteration mineralogy by XRD analysis was conducted by Kuzumaki (2018 MS) on 30 samples which includes 5 samples of the Inashibetsu Lava, 1 sample of the Rhyolite Dike, 17 samples of the Motoineppu Lava and 2 silica sinter floats hosted in the Motoineppu Lava, and 5 samples of the Kamiomu Formation around and within the vicinity of the Omui deposit (Fig. 29). The Inashibestu Lava is least altered, compact, weakly magnetic and display a gray to greenish gray color (Kuzumaki, 2018 MS). Hand specimen observation of the Moitoineppu Lava (Fig. 30A) show a white appearance and is fine-grained. The rock varies from weak to strongly silicified with clay alteration, quartz veins and stringers. Unaltered rhyolite lapilli tuff with pissolitic textures are observed north of the Otoineppu River (Fig. 31A-1), and silicification tends to increase with vuggy texture of the rock easterly towards the Omu silica sinter (Fig. 29. A-2). Near the base of the Omu silica sinter (Fig. 29), the Numa-dake Lava

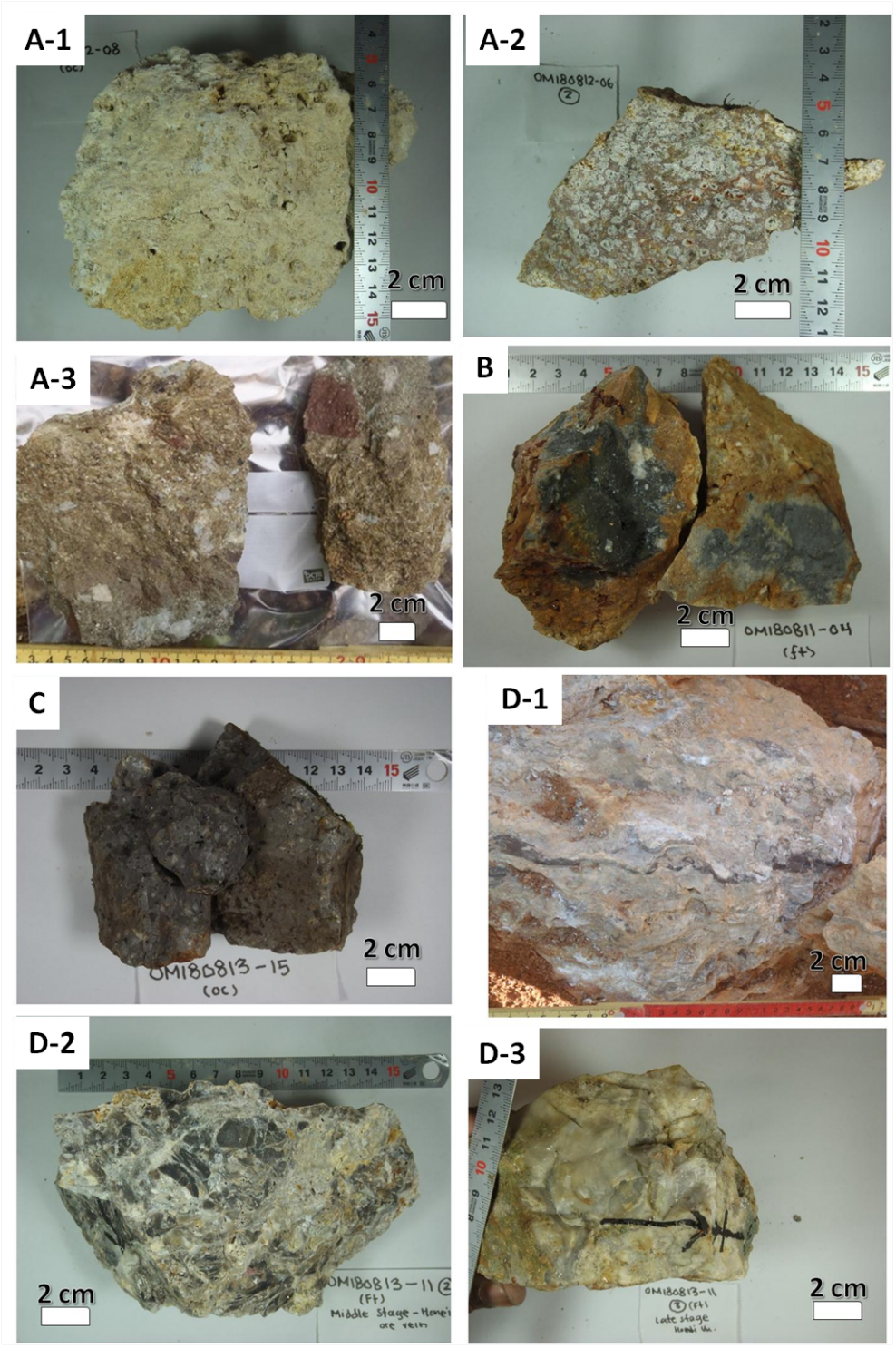

Fig. 30 Representative photos of least and altered host rocks and the Honpi vein. (A-1) Least altered rhyolite lapilli tuff of the Motoineppu Lava with pissolitic texture. (A-2) Silicified rhyolite lapilli tuff with pissolites removed forming vugs. (A-3) Least altered rhyolite lapilli tuff of the Motoineppu Lava (Kuzumaki, 2018 MS). (B) Silicified Numa-Dake andesite. (C) Rhyolite Dike sample obtained from outcrop,

(Fig. 30 continued)

used for K-Ar age dating on hornblende in this study. UTS07). (D-1) Honpi early stage vein. (D-2) Honpi middle stage vein. (D-3) Honpi late stage vein.

is silicified (Fig. 30B), fine-grained and weathered at the edges, and observed as fresh and coarse grained along the coast northeast from the Omu silica sinter (Fig. 29). The Rhyolite Dike near the Omui deposit along the Motoineppu River trends NE-SW, is grey and weakly altered, display chilled margins at contacts, and display visible hornblende crystals of mm sizes (Fig. 30C). The Rhyolite Dike trends NW-SE near the historical Hokuryu mine (Fig. 29). The main Omui vein (Honpi vein) is characterized by three stages, an early (Fig. 30D-1), middle (Fig. 30D-2) and late (Fig. 30D-3). The early and middle stages represent the main mineralization events. Abundant quartz and thin (<1 mm) ginguro bands were formed in the early stage. Mineralization accompanied with brecciation deposited ore during the middle stage, followed by the precipitation of abundant quartz and trace ginguro bands in the late stage. Kaolinite was formed in the early and middle stages, and is lesser in the late stage. Adularia and illite were also formed, but in minor to trace amounts in the veins. Bladed calcite was formed at places in the early and middle stages (Fig. 30D). Colloform-crustiform banding is observed in the early, middle and late stages. Chemical composition of electrum determined by scanning electron probe micro-analyzer (EPMA) ranges from 29.9 to 49.3 at% Au (av. 42.6 at% Au) in the middle stage of the Honpi vein (Kuzumaki, 2018 MS).

Silica sinters were observed a few 100 meters west from the Omui deposit as floats along the tributaries of the main Motoineppu River. The silica sinters are

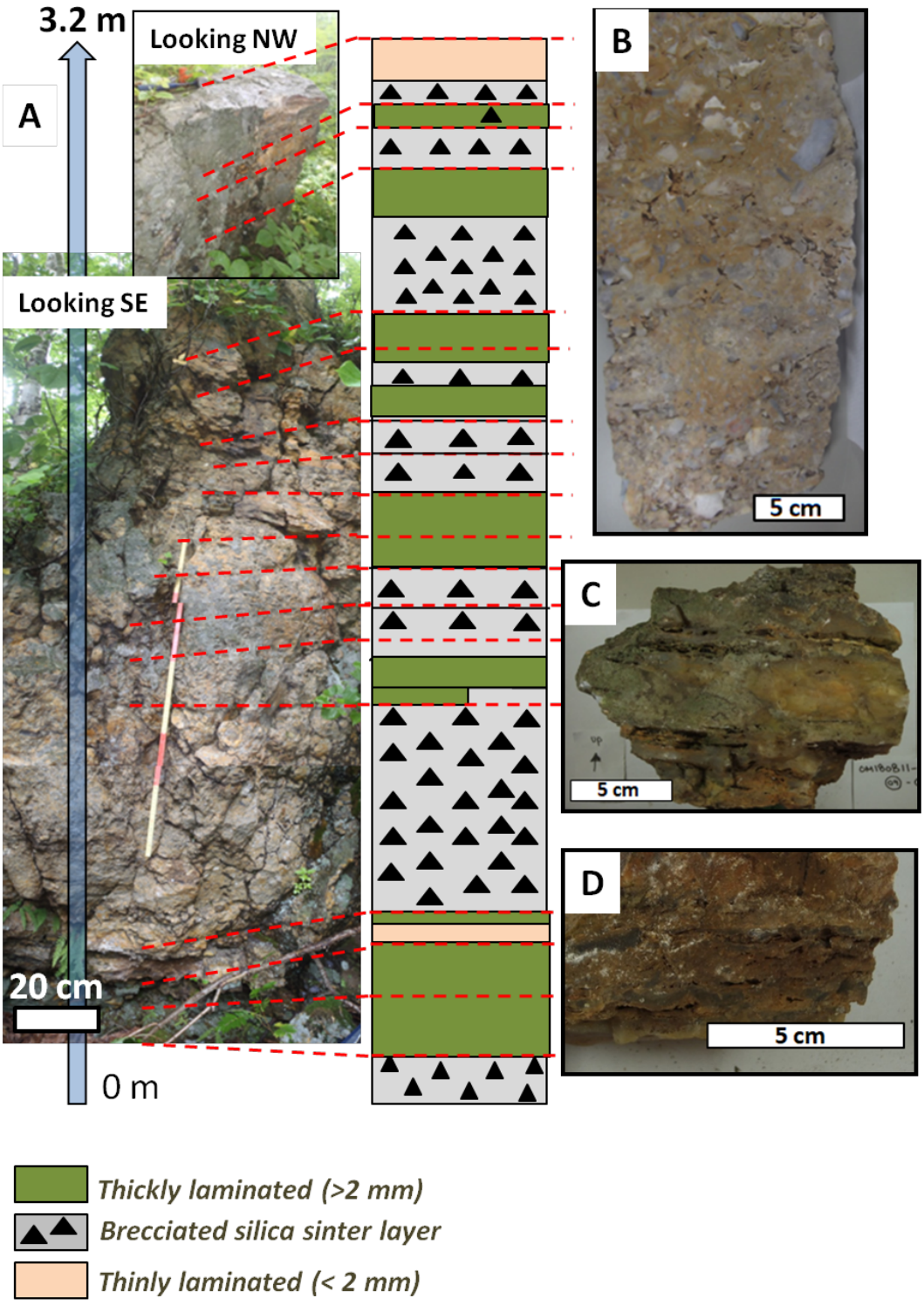

Fig. 31 Outcrop of the Omu silica sinter. (A) Outcrop photo and schematic sketch. (B) Representative photo of a brecciated silica sinter layer. (C) Representative photo of a thickly laminated silica sinter layer. (D) Representative photo of a thinly laminated silica sinter layer.

consecutively laminated with black, brownish red and white layers, compact, and range from 20 to 40 cm in total layer thickness.

Approximately 8 km north of the Omui deposit, outcrops of silica sinter (Omu sinter) forming up to 3.2 m high terraces are observed south of the Otoineppu River (Figs. 29, 31). The Omu silica sinter is massive, and brecciated at intervals. From a 3.2 m high, gently NW dipping silica sinter, each layer is either brecciated, thickly or thinly laminated (Fig. 31). The base of the silica sinter is commonly mineralized (e.g., Irving Resources Inc., 2018), with black and white consecutive layering observed from the base to about 40 cm up.

4.4 Analytical methods

For bulk chemical analyses, twenty-nine representative samples of quartz veins and silica sinters were lightly crushed using an iron motar and pulverized in an agate motar to silt size. Powdered sampled were analyzed using an inductively coupled plasma mass spectrometer (ICP-MS) Agilent 7500 Series Agilent Technology ICP-MS by an acid digestion by HF, $HClO_4$ for Ag, Mn, Cu, Zn, Rb, Sr, Sb, Te, Ba and Pb, and aqua regia for Au. Reference standards from GSJ were used in ICP-MS and AAS analyses. The analysis was conducted at Akita University, Japan.

Age dating was conducted on hornblende fractions obtained from a Rhyolite Dike (Figs. 29, 30C). Mineral separates of hornblende was sent to the Institute of Geological and Nuclear Sciences Limited in New Zealand for K-Ar age determination.

4.5 Results

4.5.1 The Omui (Honpi) vein

Mapping and rock chip sampling was conducted along a trench within the vicinity of the Omui historical mine. The trench was first excavated by the previous property owner in 1995, and was revisited by Irving Resources Inc. in 2016 (SRK, 2018).

The quartz veins observed along the trench are dominantly massive with ginguro bands <1 cm (Fig. 32). The massive crustiform-colloform veins + ginguro bands either strike towards the NW (dip SW) or NE (dip SE), with dip angles greater than 40° inclination (Fig. 32).

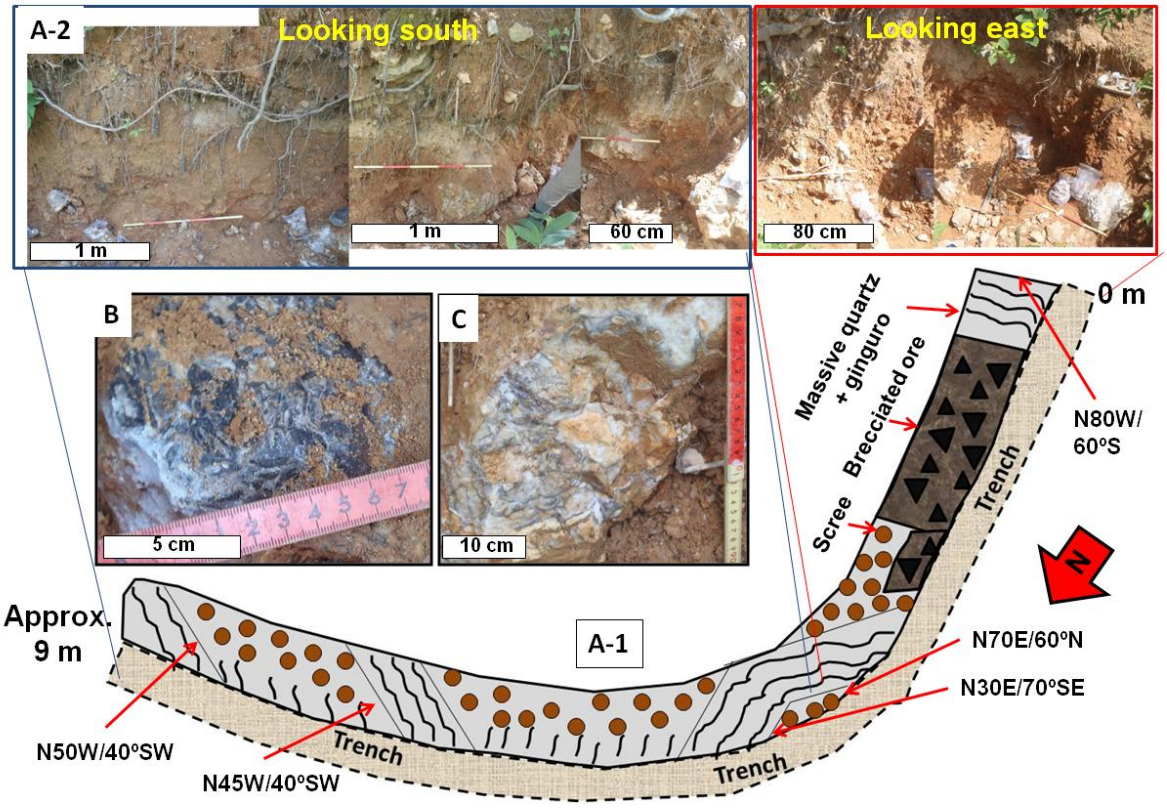

Fig. 32 Omui (Honpi) vein trench mapping. (A-1) Sketch of the trench with details collected during mapping and rock chip sampling. (A-2) Portrait joined images of the trench with line color marking respective of where the photos started and ended. (B) Representative image of the brecciated ore. (C) Representative image of the massive colloform-crustiform quartz vein with ginguro.

The massive crustiform-colloform veins + ginguro bands tightly occur together, and are normally overlain by weathered scree material (Fig. 32). The brecciated ore zone is commonly black and is composed of brecciated angular ore fragments in a matrix that consist of quartz ± kaolinite ± illite ± bladed calcite ± K-feldspar (e.g., Kuzumaki, 2018 MS; Fig. 32). Approximately 10 m towards the SE of the trench, a 3 m boulder of the Honpi vein was observed exhibiting three stages of quartz veining. Samples were obtained from the early stage (e.g., Fig. 30D-1), middle stage (Fig. 30D-2) and late stage (Fig. 30D-3) for bulk geochemical analysis. The veins are hosted in the Motoineppu rhyolite.

Ore mineral identified under microscopic observation in the Honpi vein consists of electrum, argentite and stephanite (Kuzumaki, 2018 MS). These ore minerals are closely associated with microcrystalline quartz that exhibit colloform and microsphere textures, and scarcely associated with mosaic quartz (Zeeck, 2018 MS).

4.5.2 Omu silica sinter

From field observation and hand description, 29 silica sinter layers were identified (Fig. 33). Terminology used in the identification of the silica sinter structures and layers (lithofacies) is adopted from Hamilton *et al*. (2019).

4.5.2.1 Sinter clast breccia

The sinter clast breccia is the dominant lithofacies that make up the Omu silica sinter. The sinter clast breccia is approximately 50 to 60% clast supported and 40 to 50% matrix supported (Figs. 31B, 33).

The clasts are of silica sinter origin, angular, and are commonly < 5 cm across (Fig. 31B, 33). Angular and elongated chalcedonic milky white, grey and dark grey

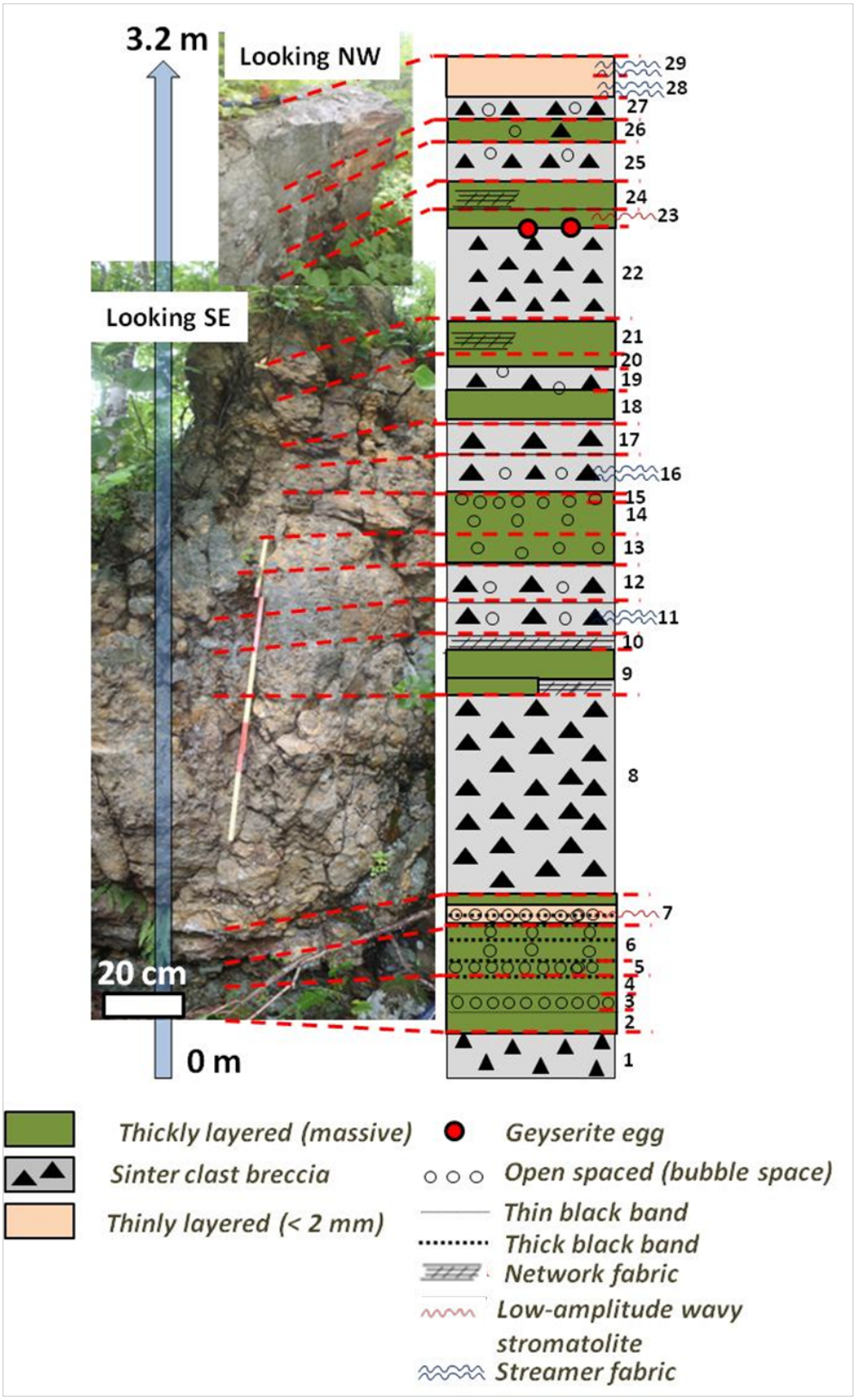

Fig. 33 Structures observed in the Omu silica sinter layers. A total of 29 layers were identified.

clasts are common throughout the sinter clast breccia, with lesser adularia clasts (<1 cm) typically observed in the layer 8 (Fig. 33). The elongated angular clasts exhibit a flow orientation towards the SE to ESE.

The matrix composes dominantly of chalcedony, or microcrystalline quartz that recrystallized from initially amorphous silica (Fig. 31B). Open spaced (bubble space) structure <0.5 cm is commonly observed in the chalcedonic matrix, with open spaced structure >1 cm commonly formed in layers 11, 12, 16, 19, 25 and 27 (Fig. 33).

Hematite alteration is prevalent throughout. Cinnabar was observed in layer 8. At the base of the sinter clast breccia (Fig. 33, layer 1), massive sulfides were reported to be hosted in the sinter clast breccia (SRK, 2018).

Hydrothermal breccia pipes cross-cut the silica sinter clast breccia (layer 8?) few meters SW from the studied silica sinter terrace (Fig. 34).

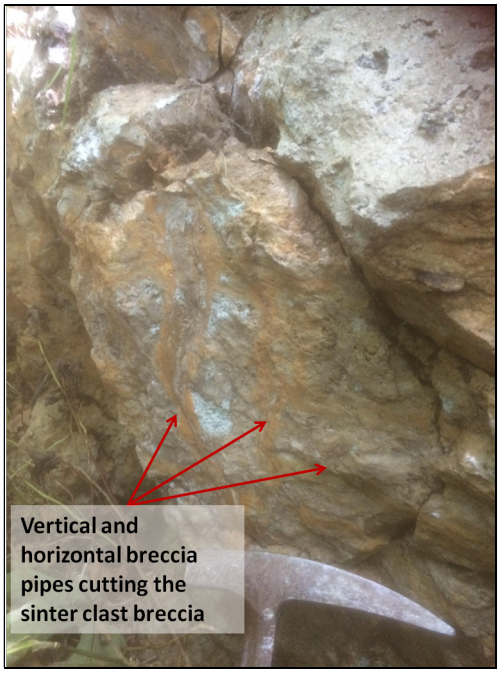

Fig. 34 Hydrothermal breccia pipes hosted in the silica sinter clast layer.

The vertical hydrothermal breccia pipes are approximately 3 cm in width, silicified, and horizontally branch out into the sinter clast breccia (Fig. 34). The hydrothermal breccia pipes are commonly coated with Fe-oxides, and contain angular silica sinter clast in a silicified matrix (Fig. 34).

4.5.2.2 Thickly laminated (layered)

The thickly laminated is the second dominant lithofacies formed (Fig. 33). Thickly laminated consist of chalcedony, and is massive. Layers range from >2 mm to 15 cm in width (Figs. 31C, 35A, C, D). Thickly laminated is typically milky white in color, and commonly exhibit open spaced (bubble space) structure (Fig. 35A, C, D).

Thickly laminated grey to dark grey chalcedony (containing sulfides?) >2 mm is observed in layers 4 and 6 with minor thinly laminated (<2 mm) grey to dark grey chalcedony (containing sulfides?) (Figs. 33, 31D). Thickly laminated was formed in layers 2 to 7, 9, 13 to 15, 18, 20, 21, 23 24 and 26 (Fig. 33).

4.5.2.3 Thinly laminated (layered)

Thinly laminated consist of laminations <2 mm in width (e.g., Hamilton *et al.,* 2019). Thinly laminated consist of fine chalcedony bands that are commonly milky white (Fig. 35A, B-1) and may boarder or occur together with thickly laminated and sinter clast breccia (e.g., Fig. 35A). Thinly laminated may also exhibit grey to dark grey laminations (due to presence of sulfides?) (Fig. 31D). Thinly laminated was commonly formed in the layers 3, 7, 28 and 29 (Fig. 33), and are commonly wavy.

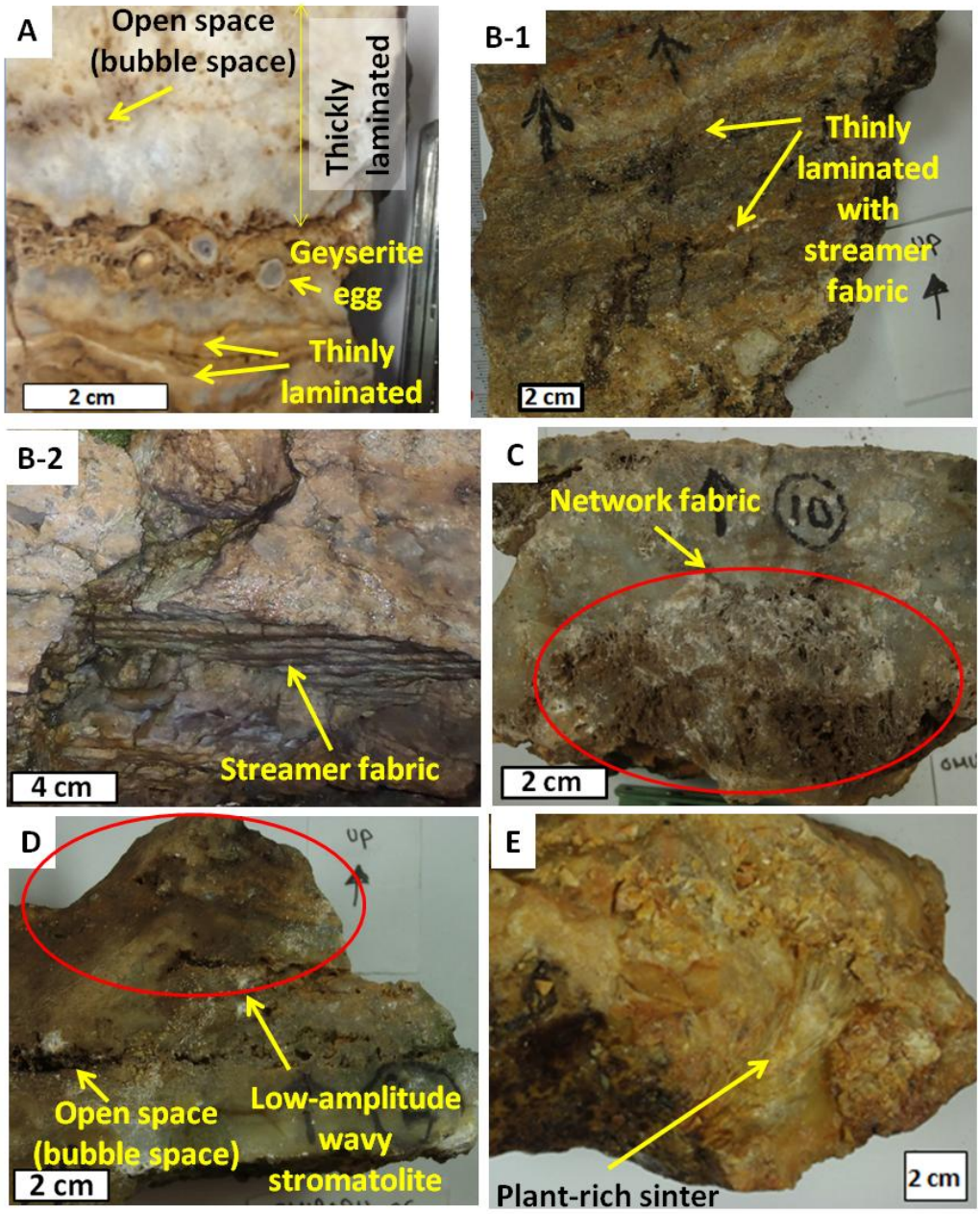

Fig. 35 Type of layers (lithofacies) and structures observed in the Omu silica sinter. (A) Geyserite egg sandwiched between thickly laminated and thinly laminated layers. (B-1) Thinly laminated layers exhibiting streamer fabric (top of silica sinter). (B-2) Example of a streamer fabric (ripple marks) that formed 10 m NE of the studied silica sinter outcrop. (C) Network fabric associated with thickly laminated. (D) Low-amplitude wavy stromatolite associated with open spaced (bubble space) and thickly laminated. (E) Plant-rich sinter (encrustation mimicking a leaf or wood?).

4.5.2.4 Open spaced (bubble space)

Open spaced (or bubble space) are commonly created by microbial organisms as they release gases into their surroundings (e.g., Hamilton *et al.,* 2019; Fig. 35A, D). This structure is observed throughout the silica sinter, and is commonly <5 mm in diameter (Fig. 35A). Areas of intense open spaced structure or of larger diameters (> 5mm to 1 cm) are represented in Figure 33. Due to the lack of microscopic observations to confirm the presence of microbial organisms such as microbial filaments (e.g., Lynne, 2013), it remains uncertain whether the open spaced structure was caused by microbial activities or not. In hand specimen, the open space structure <5 mm display an appearance similar to bubble mat structure (e.g., Hamilton *et al.,* 2019).

4.5.2.5 Network fabric

Network fabric display network-like irregular criss-crossing threads of chalcedony, and may be an analogue to the appearance of bladed calcite (e.g., Hamilton et al., 2019; Figs 33, 35C). Network fabric is commonly associated with thickly laminated, and is observed in the layers 7 and 23 and partially in layer 24 (Fig. 33).

4.5.2.6 Streamer fabric

Aligned and wavy microbial strands that are commonly parallel to each other, and may show flow orientations and may overlap each other (Fig. 33B-1, B-2). Approximate 10 m towards the NE of the silica sinter outcrop (Fig. 32), streamer fabric is observed and was interpreted as ripple marks (Fig. 33B-2; Irving Resources Inc., 2018).

4.5.2.6 Low-amplitude wavy stromatolite

Low-amplitude wavy stromatolite are wavy, with wavelengths >5 cm (e.g., Hamilton *et al*., 2019) and are broadly convex upward (e.g., Hamilton *et al*., 2019). Open spaced (bubble space) are commonly present directly below the convex region, and gradually decrease in size and intensity outwards (Fig. 35D). Low-amplitude stromatolite is commonly associated with the sinter clast breccia and thickly laminated, and is observed in layers 10, 11, 21 and 24 (Fig. 33).

4.5.2.7 Geyserite egg

Geyserite eggs formed at the margin of layer 22 and 23 (Fig. 33), associated with open spaced (bubble space) structure (Fig. 35A). Geyserite egg is concentric, and spherical, and is analogue to an egg (hence the name geyserite "egg"). The geyserite egg is <1 cm, and is milky white in color and exhibit concentric zoning (Fig. 35A).

4.5.2.8 Plant-rich sinter

Plant-rich sinter consists of silicified leaves, twigs and leaves or other biota which are encrusted with chalcedony which precipitated from initially amorphous silica (e.g., Fig. 35E). Figure 35E shows a plant-rich sinter float sample collected approximately 8 km upstream of the Otoineppu River. In the vicinity of Omu town, plant-rich sinters (commonly petrified wood) are a commonly sighted.

4.5.3 Bulk rock geochemistry

The bulk concentration of Au, Ag, Mn, Cu, Zn, Rb, Sr, Sb, Te, Ba, and Pb of the Omu silica sinter and Omui vein are presented in Table 12. The Au, Ag and Sb contents of the Omu silica sinter range from 0.01 to 0.27 ppm and from 5 to 45 ppm and from 50 to 378 ppm, respectively. The Au, Ag and Sb contents of the

Table 12 Whole-rock concentration of selected elements of the Omu silica sinter layers and Omui vein (early, middle and late stages)

Layer/ stage	SAMPLE TYPE	Au ppm	Mn ppm	Cu ppm	Zn ppm	Rb ppm	Sr ppm	Ag ppm	Sb ppm	Te ppm	Ba ppm	Pb ppm
1	Silica sinter (Base)	0.19	55.39	11.39	6.16	7.87	22.98	8.9	99.3	b.d	83.09	2.49
2	Silica sinter	0.02	45.52	9.89	b.d	2.44	2.22	5.37	377.7	b.d	26.85	1.69
3	Silica sinter	0.05	38.62	9.2	b.d	4.4	5.68	13.36	138.5	b.d	26.07	0.88
4	Silica sinter	0.11	56.27	15.03	18.50	6.92	14.1	23.59	167.1	b.d	59.47	1.24
5	Silica sinter	0.27	58.33	19.13	b.d	10.73	17.2	45.16	271.9	b.d	115.9	3.5
6	Silica sinter	0.19	58.69	18.06	1.37	18.19	23.38	23.45	183.1	b.d	180.5	3.08
7	Silica sinter	0.25	60.3	19.06	26.55	18.22	27.84	24.18	147.8	b.d	139.7	2.22
8	Silica sinter	0.28	46.68	13.24	29.72	15.82	25.15	13.24	67.97	b.d	239.1	2.21
9	Silica sinter	0.05	56.24	9.81	9.79	3.07	13.96	12.71	248.4	b.d	167.2	0.44
10	Silica sinter	0.16	56.79	9.37	b.d	10.21	31.55	33.73	138.9	b.d	166.3	2.24
11	Silica sinter	0.19	55.26	10.38	b.d	9.27	29.5	23.26	114.6	b.d	188	1.36
12	Silica sinter	0.17	46.21	9.58	b.d	7.34	20.79	15.77	145.4	0.05	168.1	1.97
13	Silica sinter	0.08	47.99	7.91	b.d	8.89	16.98	14.91	192.2	b.d	92.97	1.63
14	Silica sinter	0.04	42.82	8.79	b.d	4.33	8.2	4.92	304.4	b.d	36.98	0.54
15	Silica sinter	0.01	64.29	9.14	b.d	7.41	14.48	8.25	256.1	b.d	64.81	0.95
16	Silica sinter	0.09	57.88	10.27	b.d	11.88	36.15	21.24	85.51	0.02	109.7	1.84
17	Silica sinter	0.05	47.58	8.4	b.d	9.94	35.56	10.22	69.31	b.d	262.9	1.93
18	Silica sinter	0.01	34.38	6.51	b.d	5.25	11.78	4.8	182.3	b.d	54.3	0.31
19	Silica sinter	0.03	50.96	10.04	b.d	8.25	26.04	6.19	97.68	b.d	186.1	1.44
20	Silica sinter	0.05	58.75	10.71	b.d	9.53	42.9	6.13	117.3	b.d	289.2	1.42
21	Silica sinter	0.06	59.45	11.97	b.d	8.31	25.76	8.11	150.7	b.d	197	1.22
22	Silica sinter	0.2	52.2	12.62	b.d	25.14	31.18	20.75	206.6	b.d	214.9	3.69
23	Silica sinter	0.08	79.17	11.01	b.d	8.32	36.36	4.79	170.6	b.d	394.3	1.12

(Table 12 continued)

24	Silica sinter	0.01	47.95	9.72	b.d	48.57	51.17	10.9	58.98	b.d	442	3.22
25	Silica sinter	0.06	56.51	10.36	b.d	8.52	33.2	4.92	50.19	0.03	236.9	1.23
26	Silica sinter	0.17	57.58	12.39	b.d	6.86	18.16	22.74	156.2	b.d	60.47	2.13
27	Silica sinter	0.07	61.45	11.64	b.d	59.83	34.51	11.97	59.44	b.d	502.6	6.75
28	Silica sinter	0.22	131	17.88	b.d	23.54	46.47	34.47	132.7	b.d	394.6	4.14
29	Silica sinter (Top)	0.15	61.71	12.94	b.d	14.83	56.71	25.63	110.4	b.d	285.4	2.16
Early	Quartz vein	81.53	33.39	12.7	1.87	4.71	14.07	2315	188.6	0.01	15.18	12.09
Middle	Quartz vein	16.38	52.56	12.09	b.d	2.85	5.58	332.8	124.5	b.d	10.24	5.51
Late	Quartz vein	1.84	43.19	10.15	b.d	5.71	7	55.65	146.8	0.03	6.44	2.51

Abbreviations: b.d = below detection; numbers 1 to 29 = silica sinter layers depicted in Figure 33.

Omui quartz vein range from 2 to 86 ppm and from 56 to 2315 ppm and from 125 to 189 ppm, respectively. The Mn, Zn, Rb, Sr and Ba metal contents are slightly elevated in the Omu silica sinter in contrast to the Omui veins (Table 12). The Cu and Pb content in the Omu silica sinter and Omui veins show slight similar values, while Te is commonly below detection limit (Table 12).

4.5.4 K-Ar age dating

K-Ar method age dating on hornblende in the Rhyolite Dike was conducted (Figs. 29, 30C). The K-Ar age data of the Rhyolite Dike yield an age of 14.3 Ma (Table. 13).

Table 13.K-Ar age data of the Rhyolite Dike.

Mineral	K, % ± σ	^{40}Ar rad, (ng/g)	%^{40}Ar air	Age, Ma	Error σ
Hornblende	0.79±0.015	0.786±0.008	39.9	14.3	0.6

4.6 Discussion

4.6.1 Omui (Honpi) vein

Field and hand sample description of the Honpi vein showed dominant colloform-crustiform bands. Colloform banded quartz textures are formed where ascending hydrothermal fluids boil due to sharp depressurization accompanied by rapid cooling, which results in amorphous silica saturation of a colloid that eventually aggregate to form colloform bands (e.g., Hedenquist & Arribas, 2017). This fluid boiling mechanism is thought to be responsible in forming silica sinters at surface as temperatures of the silica supersaturated fluids drop below 100º C.

Studies conducted by Zeeck (2018 MS) on the Honpi vein discussed about the role of fluid flashing in the formation of high-grade, low sulfidation epithermal

deposits. The study showed that the Honpi vein exhibits a wide range of textures that represents primary growth patterns, and in addition, indicative of recrystallization and silica precursor phases of other vein minerals. Episodic mineralization was concluded based on crustiform, brecciated and alternating band structures associated with ore minerals. Densely packed micro-spheres of silica observed suggested that mosaic quartz formed from the recrystallization of non-crystalline silica precursor phase. The study also concluded that the colloform bands with relict microsphere textures were formed through rapid silica and ore mineral deposition within the veins at high temperatures (>200º C), presumably involving flashing of hydrothermal fluids at depths over 400 m below the paleo-surface. The structures and textures of quartz are similar to those observed in the Utanobori deposit (Sorulen *et al*., 2019).

Silicification and quartz ± K-feldspar ± kaolinite ± illite ± calcite in the Honpi vein may suggest that mineralization was associated with near acid to near neutral pH conditions.

Figure 36 show the metal content of the early, middle and late stages of the Honpi vein. Au and Ag mineralization is interpreted to be dominant in the early and middle stages, and scare in the late stage containing small ginguro bands. High concentration of Au and Ag were reported in the Omui vein at 480g/t and 9660g/t respectively in the middle stage of the Honpi vein (Irving Resources Inc., 2018). In the Honpi vein, Au and Ag, Au and Ba and Au and Pb are positively correlated, suggesting that Pb (together with Cu and Zn) may have precipitated with with Au and Ag in various concentrations. The precipitation timing or paragenesis of base metals in relation to precious metals deposition is unknown. Path finder elements such and Ba and Sb show elevated contents >100 ppm for Sb, and <15 ppm for Ba. The Rb and

Sr contents are low (<10 ppm), suggesting trace amounts of adularia present in the Honpi vein which may had incorporated those elements.

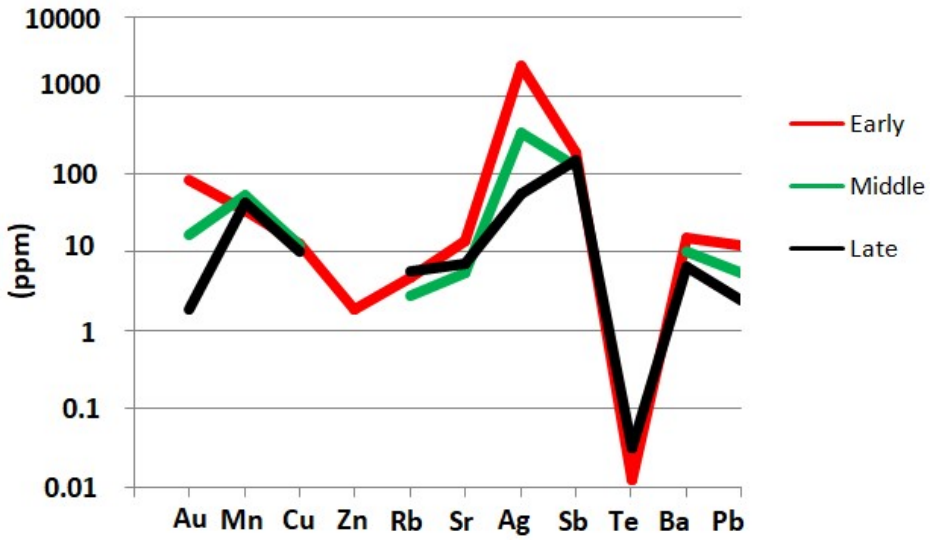

Fig. 36 Multi-elemental plot in log scale for elements Au, Ag, Cu, Zn, Sr, Sb, Te, Ba, and Pb of the Omui veins (early stage in red, middle stage in green, and late stage in black).

4.6.2 Omu silica sinter

Irving Resources Inc. reported 14.6g/t Au, 50.8g/t Ag, 676 ppm As, >100 ppm Hg, 1675 ppm Sb, 93 ppm Se and 180 ppm Tl in the sulfide rich base of the Omu silica sinter (Irving Resources Inc., 2018), suggesting that mineralization is present at depths beneath the sinter though this study found Au <0.1 ppm in the silica sinter layers. In early 2019, Irving resources Inc. conducted a drilling program with two diamond drill holes totaling 786 m at the Omu silica sinter (Irving Resources Inc. news release, April 22nd 2019). Drilling intersected argillic clay + pyrite zones and also intersected quartz veins which confirm the presence of mineralization beneath the Omui silica sinter.

The Zn, Rb, Sr and Ba metal contents of the Omu silica sinter shows slightly elevated concentrations, suggesting that these elements precipitated in the Omu silica sinter during mineralization related to the emplacement of Omu veins, and further imply that the element may prove useful as pathfinder elements in silica sinters in search of mineralized veins at depth in the Omu area. Adularia present in the Omu silica sinter may have incorporated Rb and Sr during its precipitation, causing slight elevated Rb and Sr concentrations in the silica sinter (Tables 12, 13).

In the Omu silica sinter, Au is positively correlated with Cu and Ag, while Cu show positive correlation with Mn. Positive correlations can be observed between Rb, Sr, Ba and Pb. Such correlations suggest that hydrothermal fluids responsible for Au and Ag mineralization also favored the transportation of these elements, suggesting that mineralization had continued after the deposition of the silica sinter hence depositing metals.

Table 14 Correlation matrix of the Omu silica sinter (calculated using ioGAS™ software version 7.0)

Correlation	Au_ppm	Cu_ppm	Zn_ppm	Ag_ppm	Rb_ppm	Sr_ppm	Sb_ppm	Ba_ppm	Pb_ppm
Au_ppm	1	0.73	0.52	0.72	0.063	0.15	-0.1	0.028	0.39
Cu_ppm	0.73	1	0.19	0.67	0.21	0.18	0.029	0.15	0.46
Zn_ppm	0.52	0.19	1	0.14	0.29	0.31	-0.46	0.26	-0.14
Ag_ppm	0.72	0.67	0.14	1	0.11	0.19	0.029	-0.0043	0.41
Rb_ppm	0.063	0.21	0.29	0.11	1	0.53	-0.42	0.74	0.84
Sr_ppm	0.15	0.18	0.31	0.19	0.53	1	-0.66	0.8	0.42
Sb_ppm	-0.1	0.029	-0.46	0.029	-0.42	-0.66	1	-0.55	-0.28
Ba_ppm	0.028	0.15	0.26	-0.0043	0.74	0.8	-0.55	1	0.6
Pb_ppm	0.39	0.46	-0.14	0.41	0.84	0.42	-0.28	0.6	1

Base on studies conducted on thermophilic microbes that thrive along gradients of pH, geothermal fluid flow rate, fluid composition and temperature of the silica sinter lithofacies (Hamilton *et al*., 2019), geyserite eggs suggest a depositional

temperature >75ºC, and from ~60 to 75ºC for the thinly laminated, and from ~25 to ~40ºC for the thickly laminated and plant-rich sinter layers in the Omu silica sinter.

Figure 37 summarizes the silica sinter layers (lithofacies), structures and their implication to depositional temperatures of the Omu silica sinter. A comparison of

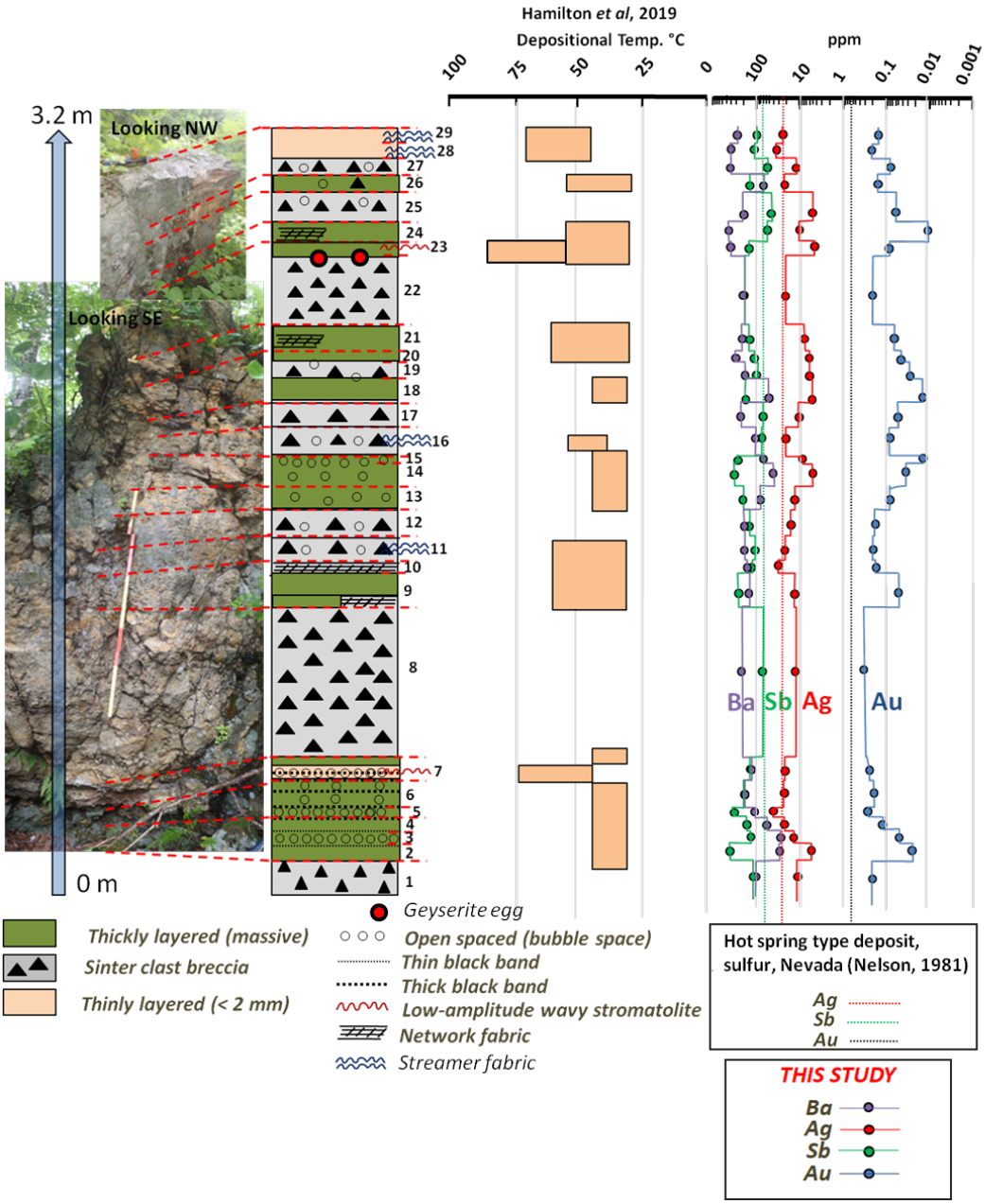

Fig. 37 Summary the silica sinter layers (lithofacies), structures and their implication to depositional temperatures of the Omu silica sinter.

metal content is given for the sulfur deposit in Navada (Nelson, 1988). In Figure 37, Au and Ag is commonly elevated in the sinter clast breccia, and partly in the thickly laminated and thinly laminated layers containing grey to dark grey thick and thin laminations.

The sinter clast breccia in the Omu silica sinter (Fig. 37) may had been formed anywhere between the proximal slope/channels to distal slope apron with respect to its vent (e.g., Hamilton *et al.,* 2019). Such is said due to its close association with thickly laminated and thinly laminated layers that form at distal slope apron and proximal slope/channels, respectively. Brecciation of initial sinter layers may have occurred due to waning spring fluid emissions, seasonal changes and/or shifts in discharge flow channels (e.g., Hamilton *et al.,* 2019). Fluid volume during flow may have been intermittent, transporting broken clast over a short distance before depositing them as evident from the angular clast present.

The hydrothermal silicified breccia pipes (Fig. 34) that cross cut the silica sinter imply that hydrothermal brecciation occurred after the deposition of the sinter clast breccia. The hydrothermal breccia pipes formed at surface may be related to hydrothermal brecciation at depth that brecciated the Omu mineralized veins (e.g., Irving Resources Inc. news release, May 22nd 2019).

The thickly laminated may had formed at distal slope apron with respect to its vent, with a formational temperature that range from ~25 to ~40ºC (e.g., Hamilton *et al.,* 2019; Fig. 37).

Thinly laminated formed in the Omu silica sinter may had been deposited from fast flowing geothermal fluids that emerge from the vent at proximal slope areas, indicating formation temperatures that range from ~60 to ~70ºC (e.g., Hamilton *et al.,* 2019; Fig. 37).

Geyserite eggs that formed in the Omu silica sinter are indicative of formational temperatures >75 ºC (e.g., Hamilton *et al.,* 2019), and may had formed in conditions that involve splashing of effusive geysers and fountains that often disturb surging vent fluids (e.g., Hamilton *et al.,* 2019). The geyserite eggs were than cemented (Figs. 35A, 37).

Low-amplitude wavy stromatolites in the Omu silica sinter (Fig. 37) may had formed where high volumes of thermal fluids where discharged, creating pools where the stromatolite grew perpendicular to the water level, with a domed feature terminating at the air-water interface (e.g., Hamilton *et al.,* 2019). Formational temperatures range from ~45 to ~60ºC, typical of mid-apron areas with respect to its vent (Hamilton *et al.,* 2019).

In the Omu silica sinter, network fabric is present (Fig. 37). The network fabric may had formed during wet and dry conditions around mid-apron pools with respect to its vent (e.g., Hamilton *et al.,* 2019). Network fabric indicates a formational temperature of ~45 to ~60ºC (Hamilton *et al.,* 2019).

The streamer fabric in the Omu sinter (Fig. 37) may have formed from fast flowing, shallow to moderately deep channels in middle apron areas (e.g., Hamilton *et al.,* 2019). Formational temperatures are similar to the network fabric.

4.6.3 Relationship between the Omu silica sinter and Omu vein

In early 2019, Irving resources Inc. conducted a drilling program with two diamond drill holes totaling 786 m at the Omu sinter (Irving Resources Inc. news release, April 22nd 2019; Chapter 1.2.2).

The first hole 19OMS-001 tested the full width of the targeted N-S trending magnetic low at Omu sinter, and was oriented northwest with an inclination of -45

degrees and reached a depth of 515 meters (Irving Resources Inc. news release, April 22nd 2019; Chapter 1.2.2).

The second hole 19OMS-002 was designated to test deeper areas under the zone of intense silicification and clay alteration encountered in hole 19OMS-001. Hole 19OMS-002 was collared 210 m northwest of hole 19OMS-001 and oriented southwest with an inclination of -60 degrees and a depth of approximately 271 m and progressing (Irving Resources Inc. news release, April 22nd 2019; Chapter 1.2.2).

The additional hole 190MS-003 was drilled in a south-southeasterly direction at an inclination of -55 degrees and was designed to test the extension of mineralization encountered in hole 190MS-002 (Irving Resources Inc. news release, May 22nd 2019). Silicification and vein breccias sulfide mineralization were encountered at depths beginning around 350 m and ended at the intersection of an east west structures at 426 m (e.g., Fig. 6; Irving Resources Inc. news release, May 22nd 2019).

190MS-004, had been collared approximately 140 m south-southeast of hole 190MS-003, with an east-southeasterly orientation and an inclination of -60 degrees (Irving Resources Inc. news release, May 22nd 2019).

Table 15 shows the drill core results from hole 190MS-002 (Irving Resources Inc. news release, May 06th 2019). The elements analyzed are Au, Ag, As, Sb, Hg and Se (Table 15). At a depth of 184.93 m, a 0.32 m interval of banded quartz vein with ginguro bands and sulfides (Fig, 38) was intersected grading 118.5 g/t Au, 1410 g/t Ag, 425 ppm As, 511 ppm Sb and 297 ppm Se (Irving Resources Inc. news release, May 06th 2019; Table 15).

The Au-Ag, Au-Sb and Ag-Sb ratios of the Omu silica sinter and Omu vein with associated argillic clay + sulfides are positively correlated, and the contents

Table 15 Fire assay results from drill hole 190MS-002 (modified after Irving Resources Inc. news release, May 06th 2019).

From (m)	To (m)	Length (m)	Au (gpt)	Ag (gpt)	As (ppm)	Sb (ppm)	Hg (ppm)	Se (ppm)
182	182.35	0.35	<0.05	0.79	121	32	1	1
182.35	182.93	0.58	0.26	7.27	207	72	1	4
182.93	183.75	0.82	0.57	11.05	285	58	2	8
183.75	184.39	0.64	0.95	16.2	358	97	6	15
184.39	184.93	0.54	1.7	31.2	214	140	9	16
184.93	**185.25**	**0.32**	**118.5**	**1410**	**425**	**511**	**26**	**297**
185.25	185.72	0.47	1.61	629	161	273	27	93
185.72	186.5	0.78	0.24	5.48	132	47	3	3
186.5	186.96	0.46	0.48	8.41	134	30	4	4
186.96	187.08	0.12	0.59	35.5	110	63	3	8
187.08	187.69	0.61	0.31	4.82	120	48	3	3
187.69	187.84	0.15	0.57	16.1	197	59	4	12
187.84	188.15	0.31	0.81	20	362	79	8	8
188.15	188.25	0.1	1.75	33.9	249	113	6	11
188.25	188.82	0.57	0.61	17.95	208	92	4	6
188.82	189.5	0.68	0.88	16.95	166	74	7	6

Note: In bold, 0.32 m interval of banded quartz vein with ginguro bands and sulfides. Grams per ton (gpt).

of Au, Ag and Sb in the Omui silica sinter and Omu veins generally show similar metal contents (Fig. 38), and imply that Au, Ag, Sb and Ba (and possibly Hg and Se) are significant pathfinder elements when prospecting for mineralized veins beneath silica sinters (e.g., Nelson, 1988). Furthermore, the similarities in metal contents between the the Omu silica sinter and Omu vein and associated argillic clay + sulfides imply that the silica sinter may had been deposited first, followed by mineralization (formation of the Omu vein) which had precipitated metals in the silica sinter. High contents of Au, Ag, As, Hg, Sb, Se and Tl in the sulfide rich base of the Omu silica sinter (Irving Resources Inc., 2018) further imply the close association of the mineralized Omu silica sinter and the Omu veins intersected by Irving Resources

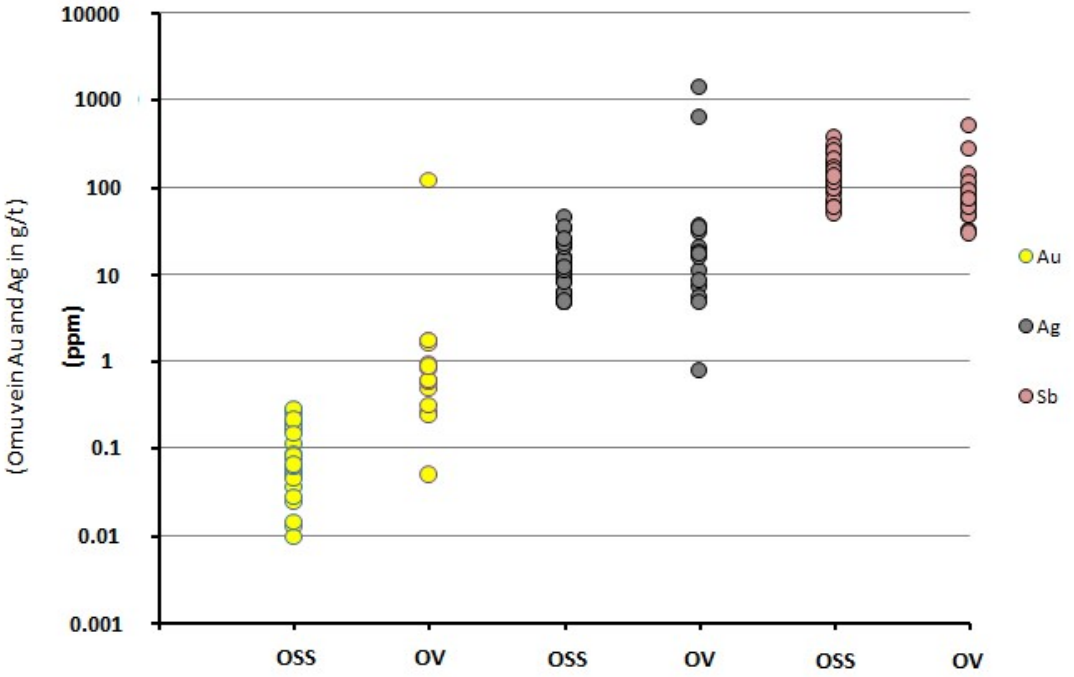

Fig. 38 The Au, Ag and Sb contents in the Omu silica sinter and Omu vein and associated argillic clay + sulfides. The Au, Ag and Sb content of the Omu veins and associated argiilic clay + sulfides were sourced from Irving resources Inc. (Irving Resources Inc. news release, May 06th 2019; Table 15). Abbreviations: OSS – Omu silica sinter; OV – Omu vein and associated argillic clay + sulfides.

Inc. at depth. Though microscopic observations were not carried on the Omu silica sinter, it is assumed that the Omu silica sinter may host stringers of mineralized veins similar to the Utanobori silica sinter (e.g., Sorulen *et al*., 2019).

4.6.4 Relationship of the Rhyolite Dike to mineralization

The Rhyolite Dike is of 14.3 Ma determined from K-Ar age dating method. Age dating conducted on the Nakahoronai andesite by Watanabe *et al*. (1991) revealed an age of 12.9 ± 0.5 Ma (Fig. 28). Koshimizu and Kim (1987) revealed an age of 12.0 ± 0.9 Ma on the Motoineppu rhyolite which is host to the mineralized quartz veins. The

former rocks are then covered by the Miocene Lava (Suzuki *et al*., 1966; Fig. 28). Age dating conducted on Inashibetsu andesite revealed an age of 9.8 ± 0.5 Ma (Watanabe and Yamaguchi, 1988). The oldest rock within the vicinity of Omui is the Kamiomu Formation (14.3 ± 1.0 Ma, Watanabe, 1995). The Rhyolite Dike post dates the Kamiomu Formation as evident from the cross cutting relationship observed in Figure 29, and pre-dates the Nakahoronai Lava, Motoineppu Lava, Inashibetsu Lava and the Maru-yama Lava. In Figure 29, the the Rhyolite dike strikes NW-SE direction near Horkuyu mine, and intrudes the Motoineppu Lava. Proximal to the Omui deposit, the Rhyolite Dike strikes NE-SW, and is dated at 14.3 Ma.

Diamond drilling by Irving Resources Inc. confirmed an E-W structure that terminated alteration and associated mineralization in hole 190MS-003 (Irving Resources Inc. news release, May 22nd 2019), suggesting that the E-W to NW-SE faults (Fig. 6) may had formed late and displaced or terminated alteration and mineralization associated with the graben structure (e.g., Irving Resources Inc. news release, May 06th 2019; Fig. 6).

In this study, it is suggested that mineralization at Omui and Omu may had initiated during the formation of the NE-SW striking graben structure. The development of the graben may had been accompanied by the emplacement of the NE-SW striking Rhyolite Dike at 14. 3 Ma, which may had acted as a heat source for hydrothermal activity in the area. It is suggested that the early stages of mineralization and silica sinter formation in the Omu and Omui were associated with this event. The early stages of vein mineralization in the Omu and Omui area consist of dominant colloform veins with ginguro bands (Figs. 30D-1, Fig. 39A).

The development of late NW-SE striking faults may had been accompanied with the second emplacement of the NW-SE striking Rhyolite Dike which may had

initiated brecciation after initial vein formation in the Omu and Omui deposit Figs. 30D-2, 39B). Such brecciation was also manifested as hydrothermal breccia pipes in the silica sinter (Fig. 34).

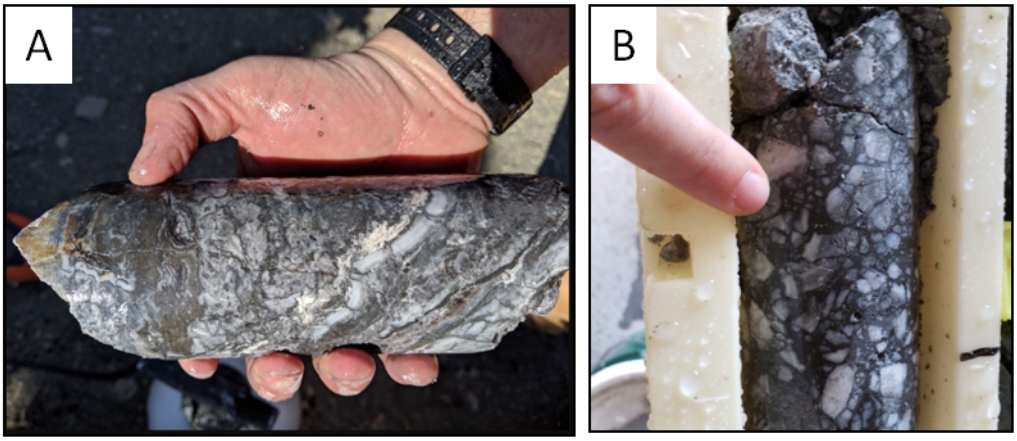

Fig. 39 Omu vein. (A) Colloform vein with ginguro bands and associated sulfide mineralization. (B) Vein breccia with associated sulfide mineralization. Photos are from Irving Resources Inc. (Irving Resources Inc. news release, April 22nd, May 06th 2019)

The relationship of the Rhyolite Dike to mineralization is uncertain, but it may had played a role as a heat source for hydrothermal activities in the vicinity of the Omu and Omui areas. The ore-forming age is not reported yet.

4.7 Conclusions

The Omui quartz vein composes of three stages, an early, middle, and a late stage. Mineralization is commonly hosted in the early and middle stages.

A total of 29 layers were identified in the Omu silica sinter. The layers commonly include sinter clast breccia, thickly laminated, and thinly laminated, geyserite eggs, low-amplitude wavy stromatolite, network fabric and streamer fabric.

Three stages were identified in the Omui vein which includes an early, middle and late stage. Mineralization is prevalent in the early and middle stages.

The Au, Ag and Sb content of the Omu vein and Omu silica sinter show similarities, implying that the silica sinter was mineralized by the Omu veins identified by Irving Resources Inc. Furthermore, the Au, Ag, Sb, Ba (and possibly Hg and Se) are significant as pathfinder elements in prospecting for mineralized epithermal veins

The Omui veins were reported to had formed at temperatures >200 ºC, which may involve hydrothermal flashing. In the Omu silica sinter, formational temperature ranges from ~25 ºC to >75 ºC (and <100 ºC).

CHAPTER 5

CONCLUSIONS

The deposition of silica sinters and hydrothermal mineralization in the Utanobori and Omui epithermal gold deposits were closely related to rhyolite volcanism in each area. Quartz textures and structures were observed in mineralized veins of the Utanobori and Omui gold deposits suggest that gold was precipitated with initially amorphous silica that crystallized to microcrystalline and mosaic quartz. Silica sinters in both deposits were mineralized, suggesting that repeated hydrothermal events occurred after silica sinters were deposited. In comparison to other low sulfidation epithermal vein-type deposits, this study has shown two of few examples where silica sinter is mineralized by cross-cutting ore-bearing vein.

REFERENCES

Adams, S. F. (1920) A microscopic study of vein quartz. Econ. Geol., 15, 623-664.

Arribas, A. and Mizuta, T. (2017) Potential for porphyry copper deposits in northern Tohoku (or the exploration potential for base metal and precious metal deposits in Japan 2010). Resourc. Geol., 68, 144-163)

Berlepsch, P, Armbruster, T, Brugger, T, Criddle, J. and Graeser, S. (2003) Tripuhyite, $FeSbO_4$, revisited. Mineralogical magazine, 67,31-46.

Buchanan, L. J. (1981) Precious metal deposits associated with volcanic environments in the southwest. Arizona Geol. Soc. Digest, 14, 237-262.

Camprubi, A. and Albinson, T. (2007) Epithermal deposits in Mexico-Update of current knowledge, and an empirical reclassification. Special Paper in Geol. Soc. Amer., 422, 377-415.

Corbett. G. and Leach. T. (1997) Southwest Pacific Rim Gold Copper Systems, Alteration and Mineralization, Short Course Manual, 318 p.

Crooke, W. (1896) The true cathode rays: electricity in high vacuum. The New York Times, Feb 23, 1896. (https://timesmachine.nytimes.com/timesmachine/1896/02/23/105742938.pdf)

Dong, G., Morrison, G. and Jaireth, S. (1995) Quartz textures in epithermal veins, Queensland-classification, origin, and implication. Econ. Geol., 90, 1841-1856.

Dudley, R. J. (1976) The use of cathodoluminscence in the identification of soil materials. Jour. Soil Sci., 27: 487-491.

Fournier, R. O. (1985) The behavior of silica in hydrothermal solutions. Geology and

Geochemistry of Epithermal Systems. Rev. Econ. Geol., 2, 45-61.

Geological Survey of Japan (1967) Metallic and non-metallic mineral deposits of Hokkaido, Japan., 574 p. (in Japanese)

Geological Survey of Japan (2009) Seamless GIS Japan: Digital Geological Data for ARCGIS, "Utanobori".

Goldstein, E. (1907) Über das Auftreten roten Phosphoreszenzlichtes an Geissler'schen Röhren: Bericht der Dutschen Physikalischen Gesellschaft, 598-605.

Gorobets, B. S. Gaft, M. L. and Podolshyi, A. M. (1989) Luminescence of Minerals and Ore (in Russia). Ministry of Geol., Moscow, 53 p.

Götze, J. (1996) Cathodoluminescence of quartz-Principle and application in geosciences (in German). Aufschluss, 47, 215-223.

Götze, J. and Plötze, M. (1997) Investigation of trace element distribution in detrital quartz by electron paramagnetic resonance (EPR). Eur. J. Mineral., 9, 529-537.

Hamilton, A. R., Campbell, K. A. and Guido, D. M. (2019) Atlas of siliceous hot spring deposits (sinter) and other silicified surface manifestations in epithermal environments. Lower Hutt (NZ): GNS Science (GNS science report; 2019/06), doi: 10.21420/BQDR-XQ16, 56 p.

Harris, D. C., Hoskins, B. F., Grey, I. E., Criddle, A. J. and Stanley, C.J. (1989) Hemloite, (As,Sb)2(Ti,V,Fe,Al)12O23OH: a new mineral from the Hemlo gold deposit, Hemlo, Ontario, and its crystal structure. Canadian Mineralogist 27, 427-440.

Hasegawa, K., Nagao, S., Fuzie, T. and Takahashi, T. (1962) Explanatory Text of the

Geological Map of “Otoineppu”. Scale, 1:50,000, 53p, Geol. Surv. Hokkaido (in Japanese with English abstract).

Hasegawa, K., Terashima, K. and Kurosawa, K. (1983) Metallic Mineral Resources of Hokkaido. Geology and Mineral Resources of Hokkaido, 3, 62p. Geol. Surv. Hokkaido. (in Japanese with English abstract).

Hedenquist, J. W. (1990) The thermal and geochemical structure of the broadlands Ohaaki geothermal systems. Geothermics, 19, 151-185.

Hedenquist, J. W. and Arribas, A. R. (2017) Epithermal ore deposits: First-order features relevant to exploration and assessment. Paper presented at the 14th Society of Geology Applied to Mineral Deposits (SGA) Biennial Meeting 2017, Quebec City, 1, 47-50.

Hedenquist, J. W., Arribas, A. R. and Gonzalez-Urein, E. (2000) Exploration for epithermal gold deposits. Rev. Econ. Geol., 13, 245-278.

Henley, R. W. and Hughes, G. O. (2000) Underground fumeroles: Excess heat effect in vein formation. Econ. Geol., 95, 453-466.

Holtstam, D., Gatedal, K., Söderberg, K. and Norrestam, R. (2001) Rinmanite, $Zn_2Sb_2Mg_2Fe_4O_{14}(OH)_2$, a new mineral species with a nolanite-type structure from the Garpenberg Norra mine, Dalarna, Sweden. Canadian Mineralogist, 39, 1675-1685.

Hussak, E. and Prior, G. T. (1897) Tripuhyite, a new antimonate of iron from Tripuhy, Brazil. Min. Magazine, 11, 302-303.

Irving Resources Inc. News release dated May 22nd 2019: Irving Resources updates drilling at Omu sinter.

Irving Resources Inc. News release dated May 06th 2019: Irving Resources encounters high-

grade gold and silver in drilling at Omu sinter.

Irving Resources Inc. News release dated April 22nd 2019: Irving Resources provides update on drilling at its Omu gold project in Hokkaido, Japan.

Irving Resources Inc. formal website: https://www.irvresources.com/projects/japan (Accessed 22nd of August 2018 and 10th of January 2019).

Irving Resources Inc. News release dated October 30th 2018: Irving Resources receives mining permit at its Omu gold-silver project, Hokkaido, Japan.

Irving Resource Inc., (2018) Society of Resour. Geol. Annual Conference, Tokyo, ppt handout, 10 p.

Ishihara, S. and Sasaki, A. (1994) Sulfur isotopic characteristics of late Cenozoic ore deposits at the arc junction of Hokkaido, Japan. Island Arc, 3, 122-130.

Ishihara, S., Yahata, M., Urashima, Y. and Watanabe, Y. (2000) Late Cenozoic ore deposits and their sulfur isotope ratios of the northeastern Hokkaido, Japan. Bull. Geol. Surv. Japan, 51, 17-28.

JDS Energy & Mining Inc. (2019) Feasibility study technical report on the Cerro Blanco project in Guatamala. A report prepared for Bluestone Resources Inc., 399p.

Komura, K., Bamba, T. and Ando, K. (1962) The research report of Au-Ag-Cu-Hg-Cr deposit around Mt. Poronupuri (northwestern part). Survey data of sub-surface resources in Hokkaido. 70, 1-21. (in Japanese).

Koshimizu, T. and Kim, C. W. (1986b) Fission-track dating of the Cenozoic formation in central-eastern Hokkaido, Japan (part 2)-“Green tuff” in Western-Central zone. Jour. Geol. Soc. Japan, 92, 559-568 (in Japanese with English abstract).

Koshimizu, S., and Kim, C.W., 1987, Fission-track dating of the Cenozoic formations in central-eastern Hokkaido, Japan (part IV) – Terrestrial pyroclastics: Jour. Geol. Soc. Japan, 93, 217–227.

Kuzumaki, K. (2018) Characteristics ofgold mineralization and ore-forming conditions at the Oumui deposit, northern Hokkaido, Japan. Bachelor 4th year thesis submitted to Akita University in Japan, 104 p.

Lalinska, V. B., Majzlan, J., Klimko, T., Chovan, M., Kucerova, G., Michnova, J., Hovoric, R., Gottlicher., J. and Steininger, R. (2012) Mineralogy of weathering products of Fe-As-Sb mine wastes and soil at several Sb deposits in Slovakia. Canadian Mineralogist, 50,1207-1226.

Large, R.R., Gemmell, J.B., Paulick, H. and Huston, D.L. (2001) The alteration box plot: A simple approach to understanding the relationship between alteration mineralogy and lithogeochemistry associated with volcanic-hosted massive sulphide desposits. Econ. Geol., 96, 957-971.

Leuz, A. K., Hug, S. J., Wehrli, B., and Johnson, C. A. (2006a). Iron–mediated oxidation of antimony (III) by oxygen and hydrogen peroxide compared to arsenic (III) oxidation. Environmental Science & Technology, 40, 2565–71.

Leverett, P., Reynolds, J. K., Roper, A. J. and Williams, P. A. (2012) Tripuyite and schafarzikite: two of the ultimate sinks for antimony in the natural environment. Min. Magazine., 76, 891-902.

Lindgren, W. (1922) A suggestion for the terminology of certain mineral deposits, Econ. Geol., 17, 292-294.

Lindgren, W. (1933). Mineral deposits: New York, McGraw-Hill, 930.

Ludwig, K. R. (2012) User's manual for Isoplot 3.75: a geochronological toolkit for Microsoft Excel, Vol. 5, Berkeley Geochronology Center Special Publication, 1-75.

Lynne, Y. B. (2013) Siliceous sinter: An early exploration tool and direct link to a geothermal reservoir. Thirty-Eight Workshop on Geothermal Reservoir Engineering, Stanford University, Stanford, California Proceedings, 1-7.

Marshall, D. J. (1988) Cathodoluminescence of geological materials. Allen and Unwin Inc., Winchester/Mass., 146.

Maeda, J., Suetake, S., Ikeda, Y., Tomura, S., Motoyoshi, Y. and Okamoto, Y. (1986) Tertiary plutonic rocks in the axial zone of Hokkaido: Distribution, age, major element chemistry, and tectonics, Monograph, Assoc. for the Geol. Coll. Japan, 31, 223-246. (in Japanese).

Mason, B. and Vitaliano, C. J. (1952) The mineralogy of the antimony oxides and antimonates. Indiana Univ. Bloomington, Indiana, U.S.A., 100-112.

Merino, E., Harvey, C. and Murray, H. M. (1989) Aqueou-chemical control of the tetrahedral-aluminum content of quartz, halloysite and other low-temperature silicates. Clays and Clay Minerals, 37, 135-142.

Mellini, M., Merlino, S. and Orlandi, P. (1979) Versiliaite and apuanite, two new minerals from the Apuan Alps, Italy. Amer. Mineralogist, 64, 1230-1234.

Ministry of International trade and Industry (MITI) (1996) Report on the Occurrence State of Trace Metal Mineral Resources. Northern Hidaka Region, the Heisei 7th (1995) fiscal year, 107 p. (in Japanese).

MITI (1994) Report of Regional Geological Survey; Northern Hokkaido B area, the Heisei 5th

(1993) fiscal year, 442 p. (in Japanese).

Mining and Materials Processing Institute of Japan (MMIJ). (1990) Japanese Gold Mines Vol. 2 Hokkaido. (in Japanese)

Morrison, G. W., Dong, G. and Jaireth, S. (1990) Textural zoning in epithermal quartz veins, Townsville, James Cook Univ. north Queensland, AMIRA project P247, 25.

Müller, A. (2000) Cathodoluminescence and characterisation of defect structures in quartz with applications to the study of granitic rocks. Ph.D. Thesis, University Göttingen, Germany.

Müller, A. R., Herrington, R., Armstrong. R., Seltmann, D., Kirwin, D. J., Stenina, Nina. G. S. and Kronz. A. (2010) Trace elements and cathodoluminescence of quartz in stockwork veins of Mongolia porphryry-style deposits. Min. Deposita, 45, 707-727.

Müller, A., René, M., Behr, H. J. and Kronz, A. (2003) Trace elements in quartz - a combined electron microprobe, secondary ion mass spectrometry, laser-ablation ICP-MS, and cathodoluminescence study. Min. Petrol., 79, 167-191.

Mullis, J. and Ramseyer, K. (1999) Growth related Al-uptake in fissure quartz, Central Alps, Switzerland, Terra Nostra, 99/6, 209.

Nelson, C.E. (1988) Gold deposits in the hot spring environment: in Schafer, R.W., Cooper, J.J. and Vikre, P.G., cds., Bulk mineable precious metal deposits of the Western United States - Symposium Proceedings. Geol. Soc. Nevada, 417-432.

Nuclear Waste Management Organization of Japan (NUMO). (2004) Evaluating Site Suitability for a HLW Repository, 83 p.

Okamura, S., Sugawara, M. and Kagami, H. (1995) Origin and spatial variation of Miocene

volcanic rocks from north Hokkaido, Japan. Mem. Geol. Soc. Japan, 44, 165-180. (in Japanese with English abstract)

Osanai, H., Mitani, K., Ishiyama, S. and Mtasushita, K. (1963) Explanatory Text of the Geological Map of "Nakatonbetsu". Scale 1:50,000, 64 p, Geol. Sur. Hokkaido (in Japanese with English abstract).

Osanai., H. Mitani, K. and Oota, M. (1962) Explanatory Text of the Geological Map of "Esashi". Scale 1:50,000,. 37p, Geol. Surv. Hokkaido (in Japanese with English abstract).

Pagel, M., Barbin, V., Blanc, P. and Ohnenstetter, D. (2000) Cathodoluminescence in Geosciences. Springer, Berlin, Heidelberg, New York, 514.

Perny, B., Eberhardt, P., Ramseyer, K., Mullis, J. and Pankrath, R. (1992) Microdistribution of Al, Li, and Na in α-quartz: Possible causes and correlation with short-lived cathodoluminescence. Amer. Min., 77, 534-544.

Pfenninger, H. (1961) Diffusion von Kationen und Abscheidung von Metallen in Quarz unter elektrischer Feldeinwirkung. Thesis, Universität Zürich, Switzerland.

Posnjak, E. and Merwin, H. E. (1919) The hydrated ferric oxides. Amer. Jour. Science, 47, 311 p.

Ramseyer, K. and Mullis, J. (1990) Factors influencing short-lived blue cathodoluminescence of a-quartz. Amer. Miner., 75, 791-800.

Rusk, B. G., Lowers, H. A. and Reed, M. A. (2008) Trace elements in hydrothermal quartz: relationship to cathodoluminescence textures and insights into vein formation. Geology, 36, 547-550.

Saunders, J. A. (1990) Colloidal transport of gold and silica in epithermal precious metal

systems: Evidence from the Sleeper deposit, Humboldt Country, Nevada. Geology, 18, 757-760.

Saunders, J. A., Schoenly, P. A. and Cook, R. B. (1996) Electrum disequilibrium crystallization textures in volcanic-hosted bonanza epithermal gold deposits, in Coyer, A. R. and Fahey, P. L. (eds.), Geology and Ore Deposits of American Cordillera. Geol. Soc. Nevada Symposium Proceedings, 173-179.

Sherlock, R., Tosdal, R., Lehrman, N. J., Graney, J. R., Losh, S., Jowett, E. C. and Kesler, S. E. (1995) Origin of the McLaughlin mine sheeted vein complex; metal zoning, fluid inclusion, and isotope evidence, Econ. Geol., 90, 2156-2181.

Shibata, K., Yamaguchi, S., Ishida, M. and Nemoto, T. (1981) Geochronology of the Desmostylus-bearing formation from the Utanobori, Kokkaido. Bull. Geol. Surv. Japan, 32, 545-549. (in Japanese with English abstract).

Shikazono, N. and Shimizu, M. (1988) Electrum: chemical composition, mode of occurrence, and depositional environment. Bull. Univ. Tokyo, 32, 1-81.

Shunso Ishihara (1998): Mineralization ages of the Kitami metallogenic province, northeastern Hokkaido, Japan. Bull. Geol. Surv. Japan, 49, 469-476.

Shuto, K. 1999. Omui gold property in Kitami region, Hokkaido, Japan. Jipangu Inc., 10.

Sillitoe, R. H. (1993). Appraisal of epithermal gold prospects and exploration approach in northern Hokkaido B area, Japan. In: MITI. Report on a regional survey of geological structure on the Northern Hokkaido B Area during the fiscal year Heisei 4, 307-336.

Sillitoe, R.H., and Hedenquist, J.W. (2003) Linkages between volcanotectonic settings, ore-fluid compositions, and epithermal precious metal deposits: Econ. Geol. Special Publication 10, 315-343.

Simmons, S.F., White, N.C. and John, D.A. (2005). Geological characteristics of epithermal precious and base metal deposits: Econ. Geol. 100th Anniv. Vol., 485-522.

Simon, G., Kesler, S. E. and Essene, E. J. (1997) Phase relations among selenides, sulfides, tellurides, and oxides: II. Applications to selenide-bearing ore deposits. Econ. Geol., 92, 468-484.

SRK. (2018) Independent technical report on the Omu property, Hokkaido, Japan. Report prepared for Irving Resources Inc., 74 p.

Sorulen, T. T., Takahashi, R., Tanaka, S., Suzuki, K., Imai, A., Watanabe, Y. and Kikuchi, S. (2019) Mineralogical and geochemical characteristics of the Utanobori gold deposit in northern Hokkaido Japan, Resour. Geol. (accepted)

Suzuki, K. (2015) Hydrothermal alteration, mineralogical description and ore-forming conditions of the Utanobori gold deposit in northern Hokkaido, Japan. Bachelor 4th year thesis submitted to Akita University in Japan, 85 p.

Suzuki, M. Konoya, M. and Fujiwara, T. (1966) Geological map of Omu, Japan with explanatory text. 1:50,000. Geological Survey of Hokkaido. 25 p.

Takahashi, R., Müller, A., Matsueda, H., Okrugin, V.M., Ono, S., van den Kerkhof, A., Kronz, A. and Andreeva, E.D. (2008) Cathodoluminescence and trace elements in quartz: Clues to metal precipitation mechanisms at the Asachinskoe gold deposit in Kamchatka [ext.

abs.]: International Symposium on The Origin and Evolution of Natural Diversity, Sapporo, Japan, 2007, Proceedings, 175–184.

Tanaka, S. (2018) Studies on the mineralogical characteristics and ore-forming processes of the Utanobori epithermal gold deposit, Northern Hokkaido, Japan. Bachelor 4th year thesis submitted to Akita University in Japan, 159.

Van den Kerkhof, A. M., Scherer, T. and Riganti, A. (1996) Cathodoluminescence and EPR analysis of the Archean quartzites from the Nondweni Green stone Belt, South Africa. Abstracts SLMS International Conference on Cathodoluminescence, Nancy, Sept. 1996, 75.

Walker, T.L. (1924) Chapmanite, a new hydrous ferrous silica-antimonate from South Lorrain, Ontario. Contributions to Canadian Mineralogy, Univ. Toronto, Geol. Series, 17, 5-8.

Watanabe, Y., Uchiumi, S. and Uto, K. (1991) K-Ar ages of Neogene basalts in Kitami Green Tuff region, northeast Hokkaido: Journal of the Geol. Soc. Japan, 97, 61–64.

Watanabe, Y. and Yamaguchi, S. (1988) K-Ar ages of Miocene volcanic rocks and the tectonics in the Nayoro-Asahikawa region, northern Hokkaido: Earth Science (Chikyu Kagaku), 42, 91–99.

Watanabe, Y. (1995) A tectonic model for epithermal Au mineralization in NE Hokkaido, Japan. Resour. Geol., Spec. Issue, 18, 257-269.

Watanabe, Y. (1996) Genesis of vein-hosting fractures in the Kitami Region, Hokkaido, Japan. Resour. Geol., 46, 151-166.

Watt G.R., Wright P., Galloway S., McLean C. (1997) Cathodoluminescence and trace element zoning in quartz phenocrysts and xenocrysts. Geochim Cosmochim Acta, 61: 4337-4348.

Wei, D. and Seno, T. (1998) Determination of the Amurian Plate Motion, Mantle Dynamics and Plate Interactions in East Asia, Geodynam., 27, 337-346.

Xiong, Y. (2003) Predicted equilibrium constants for solid and aqueous selenium species to 300 °C: application to selenium-rich mineral deposits. Ore Geol. Rev., 23, 259-276.

Yahata, M. (2002) Evolution in space and time of Late Cenozoic hydrothermal activity and ore Mineralization in Hokkaido, Japan. Report Geol. Surv. Hokkaido, 73, 151-194 (in Japanese with English abstract).

Yamaguchi, S. (1981) Geological Map of "Esashi". Scale 1:200,000. Geol. Surv. Japan (in Japanese and English).

Zeeck, L. (2018) The role of flashing in the formation of high-grade, low-sulfidation epithermal deposits: A case study from the Omu camp in Kokkaido, Japan. Master thesis submitted to the Colorado School of Mines, 55 p.

Appendix

Appendix I Information summary of samples collected in this study.

Figure ID	Original sample ID	Location ID	Outcrop/sample measurement(s)	Sample Description/Structures	Host rock
KS	KS150708-01	Unknown	Approx. 30 cm vein	Crustiform-colloform Type 1 Vein, with distint ginguro band and three stages of vein formation.	Silicified conglomerate of EF
UTS 01	UTS17080909	E-W striking mine adit, south-east extension of No. 2 Kousaku Vein (Adit 1)	6-10 cm wide vein. Main adit vein striking N66°-68° E/55°-70° NW dipping	Crustiform-colloform milky Type 1 Vein (OC)	Silicified conglomerate with dominant sandstone-siltstone matrix of EF
UTS 02	UTS17080910-C	Ditto to UTS01	5-10 cm wide vein	Crustiform-colloform Type 1 Vein (with distinct adularia bands) (OC)	Ditto to UTS01
UTS 03	UTS17080911	Ditto to UTS01	10-15 cm wide vein	Ditto to above (OC)	Ditto to UTS01
UTS 04	UTS17080913	Ditto to UTS01, 1 m south of Adit 1 entrance.	5-8 cm wide vein striking E-W/65° N dipping	Type 2 Vein with discontinuous black bands exhibiting wispy structure (OC)	Silicified conglomerate with dominant siltstone matrix of EF
UTS 05	UTS17080914	Ditto to UTS04	5-8 cm wide vein striking N15°W/65° NE dipping	Ditto to UTS04 (OC)	Ditto to UTS04
UTS 06	UTS17080915-2	NE-SW striking mine adit, east extension of No. 2 Kousaku Vein (Adit 2)	7-10 cm wide vein striking N60°-80° E/70° NW to steeply dipping	Crustiform-colloform milky Type 1 Vein with observed ginguro bands of 1-2 mm thickness (OC)	Silicified conglomerate of EF
UTS 07	UTS17080916	Ditto to UTS06, quartz vein continue up to overlying silica sinter	4-5 cm wide vein striking N75° E/80° NW to steeply dipping	Crustiform-colloform Type 1 Vein with distinct 2-5 mm thick ginguro bands (OC)	Silicified tuff, conglomerate sandstone-siltstone of EF
UTS 08	UTS17080917-A	Ditto to UTS06	50 cm thick silica sinter outcrop striking E-W/02° N.	White to red-brown-orange consecutive layers (OC)	Silicified tuff of EF
UTS 09	UTS17080918-1	Ditto to UTS06	30 cm thick silica sinter outcrop	Ditto to above (OC)	Silicified siltstone of EF
UTS 10	UTS17081005	Approximately 50 m south-east of No. 8 Vein	11-12 cm wide silicified sample	Crustiform-colloform Type 2 Vein cutting silica sinter layers (F)	Silicified conglomerate of EF

Appendix

Appendix 1 (Continued)

UTS 11	UTS17081008	NEN-WSW striking mine adit, Kousaku Vein (Adit 3),	3-5 cm wide silicified sample	Crustiform-colloform Type 2 Vein cutting silica sinter layers (F)	Ditto to UTS10
UTS 12	UTS17081010	NEN-WSW striking mine adit, Kousaku Vein, 20 m east	6 cm wide silica sinter sample	White to red-brown-orange consecutive layers (OC)	Silicified conglomerate, sandstone-siltstone of EF
UTS 13	UTS17081204-2	ENE-WSW striking mine adit, E-W extension of No. 6 Vein (Adit 4)	1 cm wide vein striking N10° E/steeply dipping. Vein striking N50°-55° E/80° NW to steeply dipping.	Crustiform-colloform milky Type 2 Vein (OC)	Silicified conglomerate of EF
UTS 14	UTS17081205	East extension of No. 6 Vein (Adit 5)	2-3 cm wide vein	Crustiform-colloform milky Type 1 Vein with observed dark bands (F)	Not identified
UTS 15	UTS17081207	South cliff face exposure of Kinkomanai lava, north of main highway, approximately 5 km ESE of UM	Approximately 20 m height x 20 wide Kinkomanai Lava	Grey dacite lava, with orange to brown color due to weathering (OC)	
UTS 16	UTS17081208	South cliff face exposure of Kinkomanai lava, north of main highway, approximately 3 km ESE of UM	Approximately 15 m height x 15 m wide Kinkomanai Lava	Grey-purplish grey dacite lava with vugs less than 1-4 cm in size, at areas vugs are in filled by transparent quartz (OC)	
UTS 17	UTS17081211	Southern slope of a SE trending ridge, north of excess road, approximately 1.5 km east of UM	Approximately 12 m height x 15 m wide tuff of the Esashi Formation. Tuff beds striking N50° E/30° NW dipping	Altered yellow-brown plagioclase phenocrysts set in white weathered crystalline matrix (OC)	
UTS 18	UTS17081303	Proximal to a silicified zone, north of excess road, approximately 2.5 km southwest of UM	Approximately 5 m height x 15 m wide altered conglomerate clasts of the Esashi Formation	Less than 1 cm to 5 cm sub-rounded to rounded conglomerate clasts with strong clay alteration (OC)	

Appendix

Appendix 1 (Continued)

UTS 19	UTS17081307-2	Western slope of a E-W striking ridge, east of excess road, approximately 1.5 km NW of UM	Approximately 10 m height x 15 m clay alteration in sedimentary beds of the Esashi Formation. Beds striking N10° W/35° SE dipping	Strong white clay±pyrite alteration hosted in silt-sand-size puggy-friable rock (OC)	Argillic alteration hosted in Inter-bed of siltstone, sandstone, conglomerate and tuff of the EF
UTS 20	UTS17081307-3	Ditto to above.	Ditto to above	Ditto to UTS19. Composes also of conglomerate inter-beds (OC)	Ditto to UTS19

Abbreviations: UM=Utanobori mine, OC=outcrop, F=float, EF = Esashi Formation